Ultrafast coherent electron dynamics in solids

Michael Sejer Wismer

München 2018

Ultrafast coherent electron dynamics in solids

Michael Sejer Wismer

Dissertation
an der Fakultät für Physik
der Ludwig–Maximilians–Universität
München

vorgelegt von
Michael Sejer Wismer
aus Kopenhagen

München, den 01.08.2018

Erstgutachter: Prof. Dr. Ferenc Krausz
Zweitgutachter: Prof. Dr. Armin Scrinzi
Tag der mündlichen Prüfung: 18.09.2018

Contents

List of Figures

Zusammenfassung

Es wurde die Dynamik von Elektronen in Festkörpern, die durch intensive, Subzykluslaserpulse erregt werden numerisch untersucht. Die Berechnungen wurden auf der quantenmechanischen Ebene und in verschiedenen, unabhängigen elektromagnetischen Eichungen ausgeführt. Zuerst wurde die Dynamik der Elektronen in eindimensionalen periodischen Potentialen berechnet um die Gültigket von neuen numerischen Verfahren zu bestätigen. Eines dieser Verfahren ermöglicht Simulationen von räumlich periodischen, gemischten Quantensystemen mit Hamilton-Operatoren mit gebrochener Translationssymmetrie.
Durch Anwendung der Dichtefunktionaltheorie wurden Wellenfunktionen für Halbleiter und Insulatoren hergeleitet. Danach konnt der zeitliche Verlauf des optisch induzierten Strom nach ersten Prinzipien bestimmt werden. Die Bedeutung von intraband Bewegungen für Elektronen im halbleitenden Material GaAs wurde ebenfalls untersucht. Bei Erregung mit resonanten Pulsen konnte ein stufenförmiger Anregungsmechanismus beobachtet werden.
Ähnliche Methoden wurden verwendet, um die Größe des optischen Faraday-Effektes in einem Insulator mit einer Bandlücke, grösser der Fotonenergie beider Pulse, zu bestimmen. Diese Berechnungen deuten darauf hin, dass ultraschnelle Kontrolle der optisch induzierten Chiralität möglich ist.

Thesis overview

Due to recent developments in high-field laser systems, intense sub-cycle pulses can be generated on a routine basis in laser laboratories around the world. The electric fields originating from such few-femtosecond laser pulses can be on the same order of magnitude as the internal electric fields in bulk, crystalline solids. Due to the short duration of the pulses the laser fluence can remain below the damage threshold of the material. This paves the way for exploring strong-field effects in solids in a non-destructive regime experimentally, and hence motivates theoretical investigations in this field.

This thesis is about numerical studies of strong-field effects in insulators and semiconductors. In particular, calculations are performed at a quantum mechanical level in order to examine the importance of quantum coherence in light-matter interactions in the strong-field regime.

The dynamics of electrons in one-dimensional spatially periodic potentials excited by laser pulses was simulated. Upon introducing phenomenological decoherence into the dynamical equations, it was found that the optical responses calculated from geometric phases of mixed quantum system were in excellent agreement with conventional approaches for evaluating the optically induced current and polarization response. The excellent agreement even extended to highly non-linear, strong-field regimes, and motivated the development of a numerical method to simulate open quantum mechanical systems governed by spatially periodic Hamiltonians subject to perturbations with broken translation symmetry.

Density functional theory was also employed to obtain wave functions from first principles for a number of materials, for which time-resolved optical responses were calculated. Field-induced intraband motion was found to modify the interband transitions significantly at high field strengths for transitions that would otherwise be resonant at low field strengths. For semiconducting materials like GaAs, where the transition elements are strongly peaked at the centre of the Brillouin zone, a step-like excitation mechanism was revealed at field strengths on the order of 0.5 V/Å. Similar *ab initio* methods were used to model the optical Faraday effect in the insulating, wide band gap material Al_2O_3 for few-cycle pulses. The magnitude of the effect was predicted using non-perturbative methods. Time-dependent calculations confirmed that a near-instantaneous response is to be expected.

Chapter 1 introduces the basic concepts for describing solid media at a quantum mechanical level, and describes the approaches for obtaining field-free ground states. Chapter 2 presents the equations used to model the time-resolved electron dynamics, and emphasizes the aspects of gauge invariance of electromagnetic fields in periodic systems and in open systems. The latest numerical implementation is presented in Chapter 3, where numerical approximations related to the electromagnetic gauges are considered. Numerical simulations for strong-field resonant excitations in bulk GaAs are given in Chapter 4, and simulations of the optical Faraday effect in Al_2O_3 are given in Chapter 5.

List of Publications

Peer-reviewed publications

1. Michael S. Wismer, Stanislav Yu. Kruchinin, Marcelo Ciappina, Mark I. Stockman, and Vladislav S. Yakovlev. Strong-field resonant dynamics in semiconductors. *Phys. Rev. Lett.*, 116:197401, May 2016

2. Vladislav S. Yakovlev and Michael S. Wismer. Adiabatic corrections for velocity-gauge simulations of electron dynamics in periodic potentials. *Computer Physics Communications*, 217:82–88, Aug 2017

3. Michael S. Wismer, Mark I. Stockman, and Vladislav S. Yakovlev. Ultrafast optical faraday effect in transparent solids. *Phys. Rev. B*, 96:224301, Dec 2017

4. Michael S. Wismer and Vladislav S Yakovlev. Gauge-independent decoherence models for solids in external fields. *Physical Review B*, 97(14):144302, 2018

5. Muhammad Qasim, Michael S Wismer, Manoram Agarwal, and Vladislav S Yakovlev. Ensemble properties of charge carriers injected by an ultrashort laser pulse. *Physical Review B*, 98(21):214304, 2018

6. Shawn Sederberg, Dmitry Zimin, Sabine Keiber, Florian Siegrist, Michael S. Wismer, Vladislav S. Yakovlev, Isabella Floss, Christoph Lemell, Joachim Burgdorfer, Martin Schultze, Ferenc Krausz, and Nicholas Karpowicz. Attosecond metrology in solids. *submitted*

7. Michael S. Wismer and et al. Detection of berry curvature in two-dimensional solid media. *In preparation*

Conference contributions

1. Michael S. Wismer, Stanislav Yu. Kruchinin, Marcelo Ciappina, Mark I. Stockman, Ferenc Krausz, and Vladislav S. Yakovlev. Ultrafast coherent control of charge carriers in semiconductors. *CLEO/Europe-EQEC 2015*, Jun 2015

2. Michael S. Wismer, Stanislav Yu. Kruchinin, Marcelo F. Ciappina, Mark I. Stockman, and Vladislav S. Yakovlev. Strong-field resonant light-induced currents in semiconductors. *8th EPS-QEOD Europhoton Conference*, Aug 2016

3. Michael S. Wismer, Mark I. Stockman, and Vladislav S. Yakovlev. Ultrafast optical faraday effect in crystalline al2o3. *6th International Conference on Attosecond Physics*, Jul 2017

Chapter 1

Fundamentals of solid media

Solid media are comprised of atoms bound together to form a regular lattice. The strength at which they are bond is characterized by the cohesive energy, which quantifies the strength of the atomic bonds. The valence electrons of the atoms hybridize to form bands with a continuum of allowed energy levels. This is in contrast to the original discrete levels of the atomic orbitals. Periodic crystalline media can be characterized as either metals, semi-metals, semiconductors, and insulators depending on the electronic configuration of the valence bands. If any of the bands are partially filled, the medium is a metal, whereas the medium is a semiconductor or an insulator if every bands is either fully occupied or empty. Metals can therefore absorb any infinitesimally small quantum of energy. Semi-metals are a borderline case, where an infinitesimally small perturbation leads to partially occupied bands, as the separation energy between the filled and empty bands is zero. Semiconductors and insulators are robust to small perturbations, as the energy gap, referred to as the *band gap*, between the occupied and empty states is finite. Semiconductors and insulators have the same mathematical properties, but are traditionally distinguished as semiconductors with a small band gaps are used for markedly different technological applications than insulators with large band gaps.

Light-matter interactions provide a way to modify the states of the light and the medium. Interaction with optical fields leads to a deposition of energy in the medium, and the amount of energy depends strongly on the frequency of the light. While fields with photon energies of 0.1–10 meV can excite nuclear motion, fields with photon energies of 100 meV – 10 eV typically leads to optical excitations of electrons from valence bands to conduction bands. Extreme ultraviolet light may even excite electrons from a core valence state to one of the conduction bands. Properties such as the cohesion energy, and energy differences of allowed transitions are important for a materials ability to withstand high field strengths. For sufficiently high field strengths, the crystal lattices can get distorted and the atomic bonds may break. Just below the damage threshold, large non-linear responses are expected to occur, and such non-linear responses are a central part of this thesis. A proper description of ablation processes requires modeling the transfer of energy from electrons to the nuclei, and the motion of the nuclei, and will thus not be treated here.

This chapter first covers how equations of motion in the independent particle approximation can be determined starting from a many-body system. Afterwards, properties of quantum states in periodic potentials are considered. Periodic potentials represent the microscopic, crystalline structure of solid media. Later on, computational aspects of density functional theory are considered. After the properties of electrons in solid media are considered, the next step towards obtaining the real-time response is to consider the equation of motions of the electrons in the presence of an electromagnetic field. Lastly, descriptions of a number of physical phenomena for electrons in an electric field are given.

1.1 Independent particle approximation

A prerequisite for calculating the response to an external electric field of a medium in equilibrium is to first calculate the ground state. The many-body wave function is assumed to reside in the ground state prior to all light-matter interactions. A system consisting of N electrons and M identical nuclei can in general be written as a many-body wave function:

$$\Phi(\mathbf{r}_1, \ldots, \mathbf{r}_N, \mathbf{R}_1 ..., \mathbf{R}_M) = \Psi(\mathbf{r}_1, ..., \mathbf{r}_N; \mathbf{R}_1 ..., \mathbf{R}_M)\chi(\mathbf{R}_1, ..., \mathbf{R}_M), \tag{1.1}$$

where the spin quantum number has been suppressed. Ψ is the wave function of the electrons with coordinates $\mathbf{r}_i$ and χ is the wave function of the atomic nuclei with coordinates $\mathbf{R}_j$. The dynamics is governed by the Schrödinger equation for both electrons and nuclei. The ground state, being the eigenstate with the lowest eigenvalue, fulfills the stationary Schrödinger equation

$$\hat{H}_0\Phi = E_0\Phi. \tag{1.2}$$

where H_0 is the stationary Hamiltonian, and E_0 is the energy of the ground state. Solving the Schrödinger equation for the full many-body wave function directly is unfeasible, and approximations are necessary when solving a system consisting of more than a few particles. The energy levels of the electrons and the nuclei are in general sufficiently large that the Born-Oppenheimer approximation may be applied to factor out the motion of the nuclei. Both electrons and nuclei contribute to the total optical response, but in the following chapters the dynamics of the nuclei will be neglected. After fixing the position of all nuclei, it is only necessary to consider the electronic part of the many-body wave function. The position of the nuclei determines the potential experienced by the electrons.

For crystalline, periodic solids, the nuclear potential is thus periodic in space, and a set of lattice vectors $\{\mathbf{a}_n\}$ and reciprocal lattice vectors $\{\mathbf{b}_n\}$ can be defined. Consequently, the density of electrons has the same periodicity as the potential. The electronic Hamiltonian contains a kinetic energy term, and potential energy terms which describe interactions with other particles such as nuclei, other electrons and particles arising from external fields, e.g. photons from an oscillating electromagnetic field:

$$\hat{H} = \frac{\hat{\mathbf{p}}^2}{2m_e} + \hat{V}_{\text{e-nuc}} + \hat{V}_{\text{e-e}} + \hat{V}_{\text{ext}}. \tag{1.3}$$

The electrons interact with the nuclei and one another via the Coulomb potential, and electrons also interact via exchange-correlation interactions which are a consequence of Pauli's principle that prohibits electrons from occupying the same quantum state.

For systems containing only a single electron, it is straightforward to calculate the allowed energy levels. If the system contain multiple electrons, it is convenient to express the many-body wave function as a Slater determinant of single-particle wave functions:

$$\Psi(\mathbf{r}_1, ..., \mathbf{r}_N) = \begin{vmatrix} \psi_1((\mathbf{r}_1) & \ddots & \psi_1((\mathbf{r}_N) \\ \vdots & \ddots & \vdots \\ \psi_N(\mathbf{r}_1) & \dots & \psi_N(\mathbf{r}_N) \end{vmatrix}. \tag{1.4}$$

Calculating the wave functions self-consistently, however, scales exponentially with the number of electrons, which makes it an unfeasible approach to calculate the ground state. Instead, a modern approach is to resort to conventional density functional theory, which is based on the Hohenberg-Kohn theorem [52]. The theorem establishes a one-to-one mapping between the many-body wave functions and the electron density and thereby greatly reduces the number of variables involved. A consequence of the Hohenberg-Kohn theorem is that all observables can be determined from the density alone. The theorem states that a universal functional $F[n(\mathbf{r})]$ exists such that

$$E = \langle \Psi | \hat{H} | \Psi \rangle = \int v(\mathbf{r}) n(\mathbf{r}) \, d\mathbf{r} + F[n(\mathbf{r})], \tag{1.5}$$

where $n(\mathbf{r}_1) = \int d\mathbf{r}_2 ... \mathbf{r}_N \Psi^*(\mathbf{r}_1, ..., \mathbf{r}_N) \Psi(\mathbf{r}_1, ..., \mathbf{r}_N)$ is the single-particle density. This ensures that the ground state density is uniquely defined for a pre-described potential $v(\mathbf{r})$. A common approach to determine the ground state density is to express the many-body wave function by a Slater determinant of mutually orthogonal Kohn-Sham orbitals for non-interacting electrons [63]. Orthogonality ensures that the density can be calculated as

$$n(\mathbf{r}) = \sum_i |\phi_i^{\mathrm{KS}}(\mathbf{r})|^2, \tag{1.6}$$

where the orbitals $\phi_i^{\mathrm{KS}}(\mathbf{r})$ have to be determined self-consistently. Solving the Schrödinger equation for the Kohn-Sham orbitals yields the Kohn-Sham energies E_i^{KS}:

$$\left(\hat{T}_S + \hat{v}_{\mathrm{KS}}(\mathbf{r}) \right) \phi_i^{\mathrm{KS}} = E_i^{\mathrm{KS}} \phi_i^{\mathrm{KS}}. \tag{1.7}$$

After the ground state has been obtained, the real-time response to an time-dependent external field, can be determined by solving the time-dependent Schrödinger equation for the wave functions:

$$i\hbar \frac{d}{dt} \phi_i^{\mathrm{KS}}(\mathbf{r}) = \left(\hat{H}_0[n] + \hat{H}_{\mathrm{int}}(t)[n] \right) \phi_i^{\mathrm{KS}}(\mathbf{r}). \tag{1.8}$$

The validity of the generalization to time-dependent density functional theory (TDDFT) rests on the Runge-Gross theorem [100]. According to the Runge-Gross theorem, the time-evolution due to time-dependent potentials can be determined by mapping the time-dependent potential to the time-dependent density. This approach leads to a complex, time-dependent functional A_{xc}.

The approach followed in this thesis is to consider the case where the time-dependent Kohn-Sham equations can be approximated with a Hamiltonian that only depends on the initial state and the external time-dependent potential:

$$i\hbar\frac{d}{dt}\phi_i^{\mathrm{KS}}(\mathbf{r}) = \left(\hat{H}_0[n] + \hat{H}_{\mathrm{int}}(t)\right)\phi_i^{\mathrm{KS}}(\mathbf{r}) \approx \left(\hat{H}_0[n_0] + \hat{H}_{\mathrm{int}}(t)\right)\phi_i^{\mathrm{KS}}(\mathbf{r}). \tag{1.9}$$

Further details regarding TDDFT are considered in Section 1.2 The evolution of wave functions can be interpreted as a fraction of the electrons being excited to one of the unoccupied conduction band states. A set of unoccupied Kohn–Sham orbitals can be obtained once the ground state is known. The Kohn–Sham orbitals for the unoccupied states are often interpreted as orbitals of the excited states. While the valence states are exact up the validity of the chosen exchange-correlation potential, the excited states are in general not exact. The energy difference between a valence band state and a conduction band state will thus not correspond to the actual transition energy [46].

The work presented in this thesis is based on approximating the time-dependent exchange-correlation potential by the ground-state exchange-correlation potential. It serves as an alternative to TDDFT. While the equations presented up until now are valid for all sorts of atomic, molecular and condensed matter systems, the following sections are dedicated to periodic potentials which represent crystalline materials.

1.1.1 Electrons in periodic potentials

To describe an infinite periodic system, it is beneficial to decompose the electronic part of the non-interacting wave function in such a way that the solutions to the stationary Hamiltonian can be enumerated according to a set of quantum numbers [16]. If the Hamiltonian $\hat{H}$ is spatially periodic with the periodicity given by a set of linearly independent lattice vectors $\{\mathbf{R}_m\}$, the Hamiltonian necessarily commutes with the translation operators $\hat{T}_{\mathbf{R}_m}$, $[\hat{H}, \hat{T}_{\mathbf{R}_m}] = 0$. Consequently, simultaneous eigenstates of the Hamiltonian and the translation operators can be found. The eigenvalues of the translation operators are phase factors as the translation operators are unitary. The wave function for an electron with quantum numbers n and $\mathbf{k}$ is thus decomposed as

$$\psi_{n\mathbf{k}}(\mathbf{r}) = e^{i\mathbf{k}\cdot\mathbf{r}}u_{n\mathbf{k}}(\mathbf{r}), \tag{1.10}$$

where $u_{n\mathbf{k}}(\mathbf{r})$ is a spatially periodic function that satisfies $u_{n\mathbf{k}}(\mathbf{r}+\mathbf{R}_m) = u_{n\mathbf{k}}(\mathbf{r})$ for any lattice vector $\mathbf{R}_m$. The parameter $\hbar\mathbf{k}$ is referred to as the crystal momentum in the literature, and determines the phase shift upon translation. I.e.

$$\hat{T}_{\mathbf{R}_m}\psi_{n\mathbf{k}}(\mathbf{r}) = \psi_{n\mathbf{k}}(\mathbf{r}+\mathbf{R}_m) = e^{i\mathbf{k}\cdot\mathbf{R}_m}\psi_{n\mathbf{k}}(\mathbf{r}). \tag{1.11}$$

Values of $\mathbf{k}$ for which $|\mathbf{k}\cdot\mathbf{R}_n| \leq \pi$ for all possible lattice vectors $\mathbf{R}_n$ are said to belong to the first Brillouin zone. Although the crystal momentum $\mathbf{k}$ is unbounded, it is sufficient to consider the crystal momenta within the first Brillouin zone. In addition to being periodic in real space, the functions $u_{n\mathbf{k}}(\mathbf{r})$ can be chosen such that they are also periodic in reciprocal space $u_{n\mathbf{k}+\mathbf{b}}(\mathbf{r}) = u_{n\mathbf{k}}(\mathbf{r})$ [92].

By introducing the parameter $\mathbf{k}$, the Schrödinger equation can be written as an eigenvalue equation for the periodic function with a Hamiltonian that depends on $\mathbf{k}$:

$$\hat{H}\psi_{n\mathbf{k}}(\mathbf{r}) = E_{n\mathbf{k}}\psi_{n\mathbf{k}}(\mathbf{r}) \implies \tag{1.12}$$

$$\hat{H}_{\mathbf{k}}u_{n\mathbf{k}}(\mathbf{r}) = E_{n\mathbf{k}}u_{n\mathbf{k}}(\mathbf{r}), \tag{1.13}$$

where

$$\hat{H}_{\mathbf{k}} = e^{-i\mathbf{k}\cdot\hat{\mathbf{r}}}\hat{H}e^{i\mathbf{k}\cdot\hat{\mathbf{r}}}. \tag{1.14}$$

The quantum numbers n and $\mathbf{k}$ uniquely define the energy of the eigenstate. The crystal momentum is a continuous variable, but it becomes discrete when invoking Born-von Karman boundary conditions on the periodic potential. I.e. N uniformly distributed values of the crystal momentum corresponds to the solutions of a periodic supercell with N unit cells.

Expanding the wave function requires a sufficiently large basis set. In order to determine the wave function, the cell-periodic function has to be determined as a stationary solution to the $\mathbf{k}$-dependent Hamiltonian:

$$\hat{H}_{\mathbf{k}}|u_{\mathbf{k}s}(\mathbf{r},t)\rangle = \left(\frac{(\hat{\mathbf{p}}+\hbar\mathbf{k})^2}{2m} + V(\hat{\mathbf{r}})\right)|u_{\mathbf{k}s}(\mathbf{r},t)\rangle = E_{\mathbf{k}s}|u_{\mathbf{k}s}(\mathbf{r},t)\rangle \tag{1.15}$$

Once the periodic part of the wave function is found, operators can be evaluated in the basis of stationary states. These states constitute a convenient basis for calculating electron dynamics caused by light-matter interactions. Momentum matrix elements are important for determining optical transitions and for constructing electronic band structures using $\mathbf{k}\cdot\mathbf{p}$ theory:

$$\mathbf{p}_{nm}(\mathbf{k},\mathbf{k}') = \langle\psi_{n\mathbf{k}}|\hat{\mathbf{p}}|\psi_{m\mathbf{k}'}\rangle \tag{1.16}$$

$$= \mathrm{i}\delta(\mathbf{k}-\mathbf{k}')\int_{V_{\text{cell}}} \mathrm{d}^3\mathbf{r}\; u_n^*(\mathbf{k},\mathbf{r})\nabla_{\mathbf{r}}u_m(\mathbf{k}',\mathbf{r}). \tag{1.17}$$

The momentum operator is also important for evaluating induced currents, verifying convergence through sum rules, and for calculating the Berry curvature of bands. Likewise, the matrix element of the coordinate operator, which appears in the dipole operator $\hat{\mathbf{d}} = q\hat{\mathbf{r}}$ for a particle with charge q can in principle be determined as:

$$\mathbf{r}_{nm}(\mathbf{k},\mathbf{k}') = \langle\psi_{n\mathbf{k}}|\hat{\mathbf{r}}|\psi_{m\mathbf{k}'}\rangle = \mathrm{i}\delta(\mathbf{k}-\mathbf{k}')\int_{V_{\text{cell}}} \mathrm{d}^3\mathbf{r}\; u_n^*(\mathbf{k},\mathbf{r})\nabla_{\mathbf{k}}u_m(\mathbf{k}',\mathbf{r}). \tag{1.18}$$

Although calculating the position operator in a closed form is a non-trivial task, various approaches exist to calculate expectation values of operators containing the position operator. These difficulties arise from the fact that the position operator does not possess the translation symmetry of the potential. Another useful quantity is the overlap between wave functions at neighboring $\mathbf{k}$ points:

$$S_{nm,\mathbf{k},\mathbf{k}+\Delta\mathbf{k}} = \langle \psi_{n\mathbf{k}} | e^{-i\Delta\mathbf{k}\cdot\mathbf{r}} | \psi_{m\mathbf{k}+\Delta\mathbf{k}} \rangle \tag{1.19}$$

This quantity is important for the construction of Wannier functions [80], and for calculating the geometric phase. The Wannier functions are a set of orthogonal, localized wave functions, which are not eigenstates of the Hamiltonian. A well-known example of such states are the Maximally Localized Wannier Functions (MLWF) [80].

Upon parameterization of the Hamiltonian by the crystal momentum, a non-vanishing Berry connection may arise. The overlap matrices are also useful for evaluating the coordinate operator using an alternative approach that relies on the geometric phase of the wave functions. The geometric phase, also known as the Pancharaknam or Berry phase, is for a single $\mathbf{k}$-dependent wave function given as:

$$\gamma = \oint d\mathbf{k} \;\; \langle u_{n\mathbf{k}} | i\nabla_{\mathbf{k}} | u_{n\mathbf{k}} \rangle \tag{1.20}$$

For time-dependent systems, the geometric phase is related to the macroscopic polarization response according to the modern theory of polarization [62]. The geometric phase can also be used to calculate properties such as piezoelectricity and pyroelectricity. It requires, however, that the ground state of the system is insulating.

It is important to note that neither the wave functions nor most of the operator matrix elements are uniquely defined. The wave functions are only defined up to an arbitrary phase factors. This has consequences for calculating derivatives with respect to the crystal momentum, as the derivative cannot be calculated as a finite difference when the wave functions at the neighboring $\mathbf{k}$-points are expressed in different gauges. I.e.

$$\lim_{|\Delta\mathbf{k}|\to 0+} \langle u_{n\mathbf{k}} | u_{n\mathbf{k}+\Delta\mathbf{k}} \rangle \neq 1 \tag{1.21}$$

However, $|\langle u_{n\mathbf{k}} | u_{n\mathbf{k}+\Delta\mathbf{k}} \rangle|$ will tend to unity in the absence of degeneracies. In special cases, such as systems with one spatial dimension, it is possible to adjust the gauge of the wave functions in a rigorous manner to construct wave functions that are differentiable with respect to $\mathbf{k}$. For three dimensional *ab initio* data, numerical procedures can be used to minimize the phase difference. For two-dimensional and three-dimensional potentials, a necessary and sufficient condition for the periodic part of the wave functions to be analytic functions of $\mathbf{k}$ is that the Chern number vanishes [92].

The Berry connection $\mathcal{A}_{n\mathbf{k}} = \langle u_{n\mathbf{k}} | \nabla_{\mathbf{k}} u_{n\mathbf{k}} \rangle$ is a vector field and arises in periodic systems. While the Berry connection depends on the choice of gauge for the functions $|u_{n\mathbf{k}}\rangle$, one

can derive the gauge-independent Berry curvature $\Omega_{n\mathbf{k}} = \nabla_{\mathbf{k}} \times \mathcal{A}_{n\mathbf{k}}$. The Berry curvature gives rise to the anomalous velocity and can be calculated using the Kubo formula:

$$\Omega_{n,\alpha\beta}(\mathbf{k}) = -2\mathrm{Im} \sum_{l \neq n} \frac{v_{nl\mathbf{k},\alpha} v_{ln\mathbf{k},\beta}}{\omega_{nl\mathbf{k}}^2}, \tag{1.22}$$

where $\omega_{nl\mathbf{k}} = E_{l\mathbf{k}} - E_{n\mathbf{k}}$ is the energy difference between the bands with indices l and n, and $\mathbf{v}_{nl\mathbf{k}}$ is the matrix element of the velocity operator. In contrast to the momentum matrix elements, the Berry curvature is gauge-independent.
As the energy difference appears in the denominator, closely lying bands can have a high Berry curvature. The spin-orbit coupling lifts the degeneracy among certain states and can lead to small band gaps with a correspondingly high Berry curvature. Symmetries lead to restrictions on the Berry curvature. If time-reversal symmetry is conserved $\Omega(-\mathbf{k}) = -\Omega(\mathbf{k})$ while spatial symmetry of the potential demands that $\Omega(-\mathbf{k}) = \Omega(\mathbf{k})$. if the system has a center of inversion. It therefore requires a medium with broken time-symmetry or broken inversion symmetry to observe Berry curvature and the anomalous velocity.

1.1.2 Sum rules

Sum rules indicate self-consistency relations among the properties of the states. They are a useful tool for predicting the completeness of a truncated basis, which in turn is useful for predicting the magnitude of numerical artifacts introduced in a calculation. The fulfillment of the sum rules can therefore be a measure of convergence with respect to the number of bands for calculations involving excited states. The sum rules can e.g. be used to determine the number of bands required for high-order $\mathbf{k} \cdot \mathbf{p}$ calculations to converge, and for verifying gauge invariance of a solution obtained from a numerical simulation.

The Lagrangian $L(\mathbf{r}, \dot{\mathbf{r}})$ for a classical particle is formulated in a set of generalized coordinates $\mathbf{r}$ and their first derivatives $\dot{\mathbf{r}} = \partial \mathbf{r}/\partial t$. The Hamiltonian is then determined via a Legendre transformation:

$$H = \mathbf{p} \cdot \dot{\mathbf{r}} - L(\mathbf{r}, \dot{\mathbf{r}}) \tag{1.23}$$

where the canonical momentum is defined as $\mathbf{p}_i = \partial L/\partial \dot{\mathbf{r}}_i$.
The self-consistency condition of the basic operators arise naturally in quantum mechanics, where the canonically conjugated variables $\hat{\mathbf{r}}$ and $\hat{\mathbf{p}}$ satisfy the canonical commutation relation upon quantization of the Hamiltonian:

$$[\hat{r}_i, \hat{p}_j] = i\hbar\delta_{ij}. \tag{1.24}$$

The velocity operator is related to the coordinate operator via the Heisenberg equation of motion:

$$\hat{\mathbf{v}} = \frac{d}{dt}\hat{\mathbf{r}} = \frac{1}{i\hbar}[\hat{H}, \hat{\mathbf{r}}]. \tag{1.25}$$

For local potentials the momentum and the velocity are related via $\hat{\mathbf{p}} = m\hat{\mathbf{v}}$ in the absence of electromagnetic fields. It is thus straightforward to derive a self-consistency condition for the Hamiltonian and the coordinate matrix elements:

$$[\hat{x}_i, [\hat{H}, \hat{x}_j]] = \hbar^2 \delta_{ij}. \tag{1.26}$$

The above relation is very general, and the corresponding sum rule for eigenstates of periodic potentials is known as the Thomas-Reiche-Kuhn sum rule [77]. For a non-degenerate band n, the sum rule reads

$$\frac{2}{m} \sum_{l \neq n}^{\infty} \frac{p_{\alpha,n} p^*_{\beta,l}}{E_l - E_n} = \delta_{\alpha\beta} - m \frac{\partial^2 \epsilon_n}{\partial k_\alpha \partial k_\beta}. \tag{1.27}$$

where $\left(\frac{\partial^2 E_n}{\partial k_\alpha^2} \right)^{-1} = m^*_\alpha$ is the effective mass along the direction α for the band n, and $\delta_{\alpha\beta}$ is the Kronecker delta. In general it possible to construct an arbitrary number of sum rules involving operators to higher orders [134].

Two other relations that rely on the self-consistency of the fundamental operators are

$$e^{-i\mathbf{a}\cdot\hat{\mathbf{p}}} \hat{H}(\hat{\mathbf{r}}, \hat{\mathbf{p}}) e^{i\mathbf{a}\cdot\hat{\mathbf{p}}} = \hat{H}(\hat{\mathbf{r}} - \mathbf{a}, \hat{\mathbf{p}}), \tag{1.28}$$

$$e^{-i\mathbf{b}\cdot\hat{\mathbf{r}}} \hat{H}(\hat{\mathbf{r}}, \hat{\mathbf{p}}) e^{i\mathbf{b}\cdot\hat{\mathbf{r}}} = \hat{H}(\hat{\mathbf{r}}, \hat{\mathbf{p}} + \mathbf{b}) = \hat{H}(\hat{\mathbf{r}}, \hat{\mathbf{p}}) + \frac{1}{2m}\mathbf{b}^2 + \frac{1}{m}\mathbf{b}\cdot\hat{\mathbf{p}}. \tag{1.29}$$

The first relation utilizes the momentum operator to translate the Hamiltonian by a displacement vector $\mathbf{a}$, while the latter expression is useful for expanding the Hamiltonian with respect to changes in the momentum. These two relations are particularly useful regarding particles in a periodic potential, as $H(\hat{\mathbf{r}} - \mathbf{a}, \hat{\mathbf{p}}) = H(\hat{\mathbf{r}}, \hat{\mathbf{p}})$ if $\mathbf{a}$ is linear combination of an integer number the lattice vectors. The second relation is important once the crystal momentum has been introduced to the Hamiltonian $\hat{H}_\mathbf{k}$, as the relation can be used to relate $\mathbf{k}$-dependent Hamiltonians at different points in reciprocal space. The relation between $\mathbf{k}$-dependent Hamiltonians is particularly simple for local potentials:

$$\hat{H}_\mathbf{k}(\hat{\mathbf{r}}, \hat{\mathbf{p}} + \hbar\Delta\mathbf{k}) = \hat{H}_\mathbf{k}(\hat{\mathbf{r}}, \hat{\mathbf{p}}) + \frac{\hbar^2}{2m}\Delta\mathbf{k}^2 + \frac{\hbar}{m}\Delta\mathbf{k}\cdot\hat{\mathbf{p}}. \tag{1.30}$$

Knowing the Hamiltonian and momentum matrix elements at a particular point in reciprocal space makes it is possible to calculate energies and matrix elements at neighboring bands using. This has been demonstrated for *ab initio* data [95, 11]. Likewise, it is possible to construct the Berry curvature without resorting to Wannier interpolation [135].

1.2 Density functional theory

Density functional theory (DFT) relies on the Hohenberg-Kohn theorem and amounts to determining the ground state density, which minimizes the total energy of interacting electrons [52]. DFT allows for predicting material properties *ab initio*, as no external parameters are needed to solve the Schrödinger equation. The Schrödinger equation for the electronic wave functions $\Psi_{\mathbf{k}}$ is solved self-consistently with the Poisson equation for the internal electronic potential $\phi_{\text{int}}(\mathbf{r})$,

$$\nabla^2 \phi_{\text{int}}(\mathbf{r}) = -\frac{en(\mathbf{r})}{\epsilon}. \tag{1.31}$$

where $n = \sum_{\mathbf{k}} |\Psi_{\mathbf{k}}|^2$ is the electron density and ϵ is the permittivity. A successful approach has been to introduce a fictitious set of non-interacting Kohn-Sham orbitals, which are eigenfunctions to the Kohn-Sham potential [63]. This yields a set of equations that can be solved self-consistently. The ground state orbitals are determined by minimizing the functional

$$F[n] = \langle T \rangle + \langle V_{\text{ext}} \rangle + \langle V_{\text{Coulomb}} \rangle + \langle V_{\text{xc}} \rangle, \tag{1.32}$$

where the operators only depend on the orbitals via the electron density. A crucial part of DFT is to determine a suitable approximation for V_{xc}. A widely used approach is to first separate out single-particle kinetic energies and Coloumbic repulsion, leaving only the exchange-correlation potential undetermined:

$$F[n] = \langle T_S \rangle + E_{\text{ext}} + E_{\text{Hartree}} + E_{\text{xc}} \tag{1.33}$$

$$= \sum_n T_n + \int d\mathbf{r} n(\mathbf{r}) v_{\text{ext}}(\mathbf{r}) + \frac{1}{2} \sum_s \int d\mathbf{r} d\mathbf{r}' \frac{n(\mathbf{r}) n(\mathbf{r}')}{|\mathbf{r} - \mathbf{r}'|} + E_{\text{xc}}[n]. \tag{1.34}$$

The corresponding Kohn–Sham Hamiltonian is:

$$\left(\frac{\hat{\mathbf{p}}^2}{2m} + \hat{v}_{\text{ext}}(\mathbf{r}) + \hat{v}_{\text{Hartree}}(\mathbf{r}) + \hat{v}_{\text{xc}} \right) \phi^{\text{KS}}_{n\mathbf{k}} = E_{n\mathbf{k}} \phi^{\text{KS}}_{n\mathbf{k}}. \tag{1.35}$$

The task is thus reduced to finding an approximation for the exchange-correlation potential. A simple, and practical approach is to approximate it by the exchange-correlation potential that can be derived for a homogeneous electron gas. This is known as the Local Density Approximation (LDA). While LDA yields reasonable results for many systems, it is known to underestimate the band gap in solids. Other types of exchange-correlation potentials are Generalized Gradient Approximation (GGA) methods, such as the Perdew-Burke-Ernzerhof (PBE), which contains gradients, and meta-GGA where the potentials depend on the momentum operator as well [33].

One of the approaches to improve calculations of the band gap is to relax the requirement of the exchange-correlation energy to be derivable from a potential.
While DFT by definition is only valid for determining ground states, it has successfully

been applied in the past to determine material properties of excited states of large classes of materials. As the band gap is an important parameter for photon absorption, it is important to reproduce the band gap when numerical results are compared to experimental observations. For molecules, a common approach is to calculate hybrid functionals, while calculation of screened potentials are commonly employed in calculations of solids.

Another highly successful approach is to apply many-body perturbation theory with the use of Green's functions G and screened potentials W [50]. Due to the large computational requirements of well-converged GW calculations, the approach employed here is to solely use conventional DFT. The ground state density is calculated self-consistently within the Local Density Approximation, and the wave function eigenstates are caluculated for the Trans-Blaha modified Becke–Johnson potential (TB–mBJ). During an LDA calculation the force exerted on the nuclei can be calculated and used to determine their equilibrium positions. In a following step, the equilibrium positions can be taken for granted while the electronic wave functions are determined with a correction to the exchange-correlation potential. Calculating the wave functions for the TB-mBJ potential is computationally inexpensive compared to the procedures based on hybrid functionals or the GW approximation.
The modified Becke–Johnson potential is known to provide band gaps that are in good agreement with experimentally observed values [124, 112]. The TB–mBJ potential is designed to correct the distribution of electrons by optimizing the effective potential and, which consequently leads to band gap that are in better agreement with the experimentally observed ones. The band width are however known to be smaller [30], but for the materials considered here, the reduction in band width was not observed to be significant. Linear susceptibilities can be calculated from the equilibrium data obtained from DFT. High-order susceptibilities can also be constructed, but tend to be in worse agreement with experimental data. This is partially because those susceptibilities are more sensitive to the input data, and because non-linear interactions are neglected during the evaluation of the first-order susceptibilities.

Pseudopotentials and all-electron potential

DFT codes can be divided into two groups, namely all-electron codes that calculate the wave function of all electrons in the unit cell, and codes that replace electrons in the core-regions by pseudo-potentials. The core-electrons are much more localized than the valence electrons, and require that the wave functions for the lowest orbitals are calculated on a much smaller spatial scale than that of the typical inter-atomic distance. To overcome this difficulty, various approaches have been developed. Common DFT codes generally make use of either pseudopotentials, augmented plane-wave (APW) method, or the projector augmented wave (PAW) method [17] to efficiently handle the problem of rapidly varying wave functions near the atomic nuclei. The core states are then treated separately while orbitals than span a significant fraction of the unit cell volume can be expanded in a basis of e.g. plane waves. Linearized Augmented Plane Waves (LAPW) and Augmented Plane

Waves (APW) with local orbitals (lo) are currently considered most accurate schemes [71] [13].

Time-dependent density functional theory

Several works have dealt with explicit time-dependent density functional theory [76] [102] [115]. Several works have also suggested that the change in density, and thus the change in the Kohn-Sham potential has a minor effect on high harmonics [121] [49]. Such results indicate that using of a time-independent energy functional is sufficient when solving the time-dependent Schrödinger equation. The approach employed here is thus expected to reproduce similar results to that of calculations based on TDDFT. It should, however, be kept in mind that approaches based on TDDFT are incapable of describing e.g. optically induced transversal currents. This stems from the fact that the Runge-Gross theorem relies on equation of continuity to relate the change in electron density to the current:

$$\partial_t \rho + \nabla \cdot \mathbf{j} = 0. \tag{1.36}$$

To capture the transversal part response, i.e. currents for which $\nabla \cdot \mathbf{j}_{\text{trans}} = 0$, it is necessary to apply the time-dependent current density functional theory (TDCDFT). In addition, most applications of TDDFT in the strong-field regime use the Adiabatic Local Density Approximation (ALDA) for the time-dependent exchange-correlation [130, 131]. More elaborate time-dependent exchange-correlations are known to exist, but their application has been limited [99].

1.3 Single-particle electrodynamics

After having the described the equilibrium properties of solids, interactions between electrons and electromagnetic fields are considered. In order to study the response of few-cycle pulse with a duration of a few femtoseconds, it is preferable to consider the real-time response. This is done by solving the equations of motion for the wave functions, and propagate them in time. The natural starting point for a non-relativistic, quantum mechanical description of the response of a single electron to a classical electromagnetic field is the time-dependent Schrödinger equation:

$$i\hbar\partial_t|\psi_s(\mathbf{r},t)\rangle = \left(\frac{(\hat{\mathbf{p}} - q\mathbf{A}(\mathrm{r},t))^2}{2m} + \hat{V}_{\mathrm{lattice}}(\hat{\mathbf{r}}) + q\phi(\mathrm{r},t)\right)|\psi_s(\mathbf{r},t)\rangle \tag{1.37}$$

The spin-index will for the most part be omitted. Both the vector potential $\mathbf{A}(\mathbf{r},t)$ and the scalar potential $\phi(\mathbf{r},t)$ are gauge-dependent quantities. Different approaches to solve the dynamical equation numerically in various gauges are considered in detail in Chapter 2. As the dipole approximation is used throughout the thesis, it suffices to impose the Coulomb gauge $\nabla \cdot \mathbf{A} = 0$ as the gauge fixing condition.

In the dipole approximation, the vector potential is independent of position, and the scalar potential depends only on the coordinate operator to first order. Consequently, the presence of a vector potential does not break the translational symmetry of the potential experienced by the electrons, and the Bloch functions remain eigenstates to the total Hamiltonian. A non-vanishing scalar potential, however, breaks the translational symmetry. If a charged particle in periodic potential is exposed to a homogeneous electric field $\mathbf{F}_0$, translating the particle by a lattice vector $\mathbf{R}_i$ changes the energy by an amount $\Delta\phi_i = q\mathbf{F}_0 \cdot \mathbf{R}_i$ This complicates the procedure of determining the ground state when the energy is not bounded from below. Approaches to solve this problem are described in Chapter 3.

The Schrödinger equation cannot describe an open system, where the wave functions interact with an external environment. In contrast to a closed system, the quantum decoherence may decay over time in an open system. One way of describing an open quantum system is to express the ensemble of wave functions with a density matrix:

$$\hat{\rho} = \sum_n p_n|\psi_n\rangle\langle\psi_n|. \tag{1.38}$$

with real, positive weights p_n. Determining the dynamics for an open system requires solving the master equation. The Lindblad formalism is used when including decoherence operators, in order to ensure that the semi-definite positiveness of the density matrix and the particle number are conserved:

$$i\hbar\frac{\partial}{\partial t}\rho = [\hat{H}(t),\rho] + \sum_n \gamma_n[[\hat{L}_n^\dagger,\hat{\rho}],\hat{L}_n]. \tag{1.39}$$

This equation will also be considered further in the Chapter 3.

1.4 Examples of nonlinear optical phenomena in solids

The aim is to describe the light-matter interactions of a short, intense laser pulse interacting with electrons in a crystal as the pulse propagates through the crystal. To this end, it is sufficient to describe the dynamics in a non-relativistic, semi-classical regime. I.e. the electrons are described quantum mechanically, whereas the applied electric field of the laser pulse is sufficiently strong that it does not have to be quantized.
The purpose of a medium is two-fold. It can act as a mediator for interactions between the photons, which leads to classical nonlinear effects such as four-wave mixing. This leads to generation of light at new frequencies via difference frequency generation, sum frequency generation and third harmonic generation.
On the other hand, a laser field also modifies the properties of the medium. For semiconductor and insulators, this typically involves optical excitation of electrons to unoccupied orbitals. Nonlinear interactions modifies the state of the medium, and can lead to e.g. optically induced electric currents, or optically induced spin currents. As the medium eventually relaxes back to its ground state, it may be possible to observe florescence signals. Such relaxation mechanisms typically occur on time scales of picoseconds to nanoseconds, and are thus neglected in this work as they are much slower than excitation dynamics. The optically induced currents are important for evaluating the optical response of the medium. The effect of strong electric fields on crystalline solids was long considered important and introduced by Zener [151] and developed by e.g. Keldysh [59].

Bloch oscillations

If one considers a single electron in a certain band, and applies a constant field that is sufficient small that the electron undergoes adiabatic motion, and also neglect interactions with the environment, the electron accelerates according the Bloch's acceleration theorem. The change in crystal momentum is proportional to the instantaneous electric field:

$$\hbar\dot{\mathbf{k}}(t) = e\mathbf{F}_0(t). \tag{1.40}$$

Such transitions are *intraband transitions*. If a constant field F_0 is applied, the crystal momentum increases monotonously at a constant rate. The phase velocity $\mathbf{v}_{n\mathbf{k}} = \nabla_{\mathbf{k}} E_n(\mathbf{k})$ of the electron, however, oscillates due to the periodicity of the dispersion relation, and the electron remains localized over times scales on the order of $T = 1/(eaF_0)$, where a is the lattice spacing. This effect is known as Wannier-Stark localization. These effects can also be detected in e.g. optical lattices or superlattices where the lattice spacing is orders of magnitudes larger [48].

Multi-photon absorption

If a harmonic electric field oscillating with an angular frequency ω_{L} is applied the excitation rate can be obtained in two-well known limits. These limits are the tunneling regime where $\omega_{\mathrm{L}} \to 0$, and the multi-photon regime where the frequency is a fraction of the band gap

$\omega_{\mathrm{L}} \approx E_g/N$. The tunneling regime applies to fields that are constant in time and hence the limit of infinitesimally small frequencies need to be taken. For short time-scales it is possible to define a tunneling rate w [60]:

$$w_{\mathrm{tunneling}} = \frac{2}{9\pi^2}\frac{E_g}{\hbar}\left(\frac{mE_g}{\hbar^2}\right)^{3/2}\left(\frac{e\hbar F}{m^{1/2}E_g^{3/2}}\right)^{5/2}\exp\left(-\frac{\pi}{2}\frac{m^{1/2}E_g^{3/2}}{e\hbar F}\left(1-\frac{1}{8}\frac{m\omega_{\mathrm{L}}^2 E_g}{e^2F^2}\right)\right), \tag{1.41}$$

where the electric field F appears in the exponential pre–factor and in the denominator in the exponent. In the multi-photon regime, electron needs to absorb several photons simultaneously in order to overcome the band gap. The excitation rate will then be proportional to $w_{\mathrm{multi-photon}} \propto |E|^{2N+1}$.
If short pulses width a large bandwidth are considered instead of harmonic fields, the large bandwidth of the field may allow for multi-photon absorption of different orders. The interference arising from the various excitation pathways thus complicates the dynamics.

High harmonic generation

Numerous attempts have been made to calculate the perturbative second and third harmonics for semiconductors, and the first few harmonics have been studied in great detail [8, 6]. Recently it has been shown that plateau-like behavior can be observed for harmonics spanning tens of orders [40]. While the generation of high harmonics is a generic feature of harmonically driven, nonlinear equations of motion [9], the observed plateaus bear a resemblance to that of the high harmonics observed in gases. For gases of atoms and molecules, the cut–off energy of the high harmonic spectrum can be determined from a classical description of the electron motion. The cut-off has been determined to be $E_{\mathrm{cut}} = I_p + 3.17U_P$, where I_p is the ionization potential of the atom or molecule, and the U_P is the ponderomotive energy induced by the laser field [23].

In solids, conduction band electrons driven by an electric field may generate harmonics due to the intraband motion. Intraband harmonics are generated as the group velocity of the wave packet evolves [42]:

$$v_g = \frac{eE_0}{m_0^*}\sum_{s=1}^{\infty}\frac{1}{2s-1}\left[J_{2s-2}\left(\frac{\omega_B}{\omega}\right) + J_{2s}\left(\frac{\omega_B}{\omega}\right)\sin[(2s-1)(kz-\omega t)]\right]. \tag{1.42}$$

Harmonics can also be generated by the anomalous velocity induced by the Berry curvature, and is manifest themselves in systems that lack either time-reversal symmetry of inversion symmetry [75].
In contrast to spherically symmetric nuclear potentials experienced by electrons in atomic vapours, the crystal structure of solids can have a profound impact on the harmonics that can be generated. The conventional unit cell for diamond is shown in Figure 1.4 (a), which contains 8 carbon atoms. Diamond is an example of a cubic material with isotropic first order-responses. Figure 1.4 (b) and (c) show the projection of the unit cell for the crystal directions [111] and [100], which are clearly seen to have different

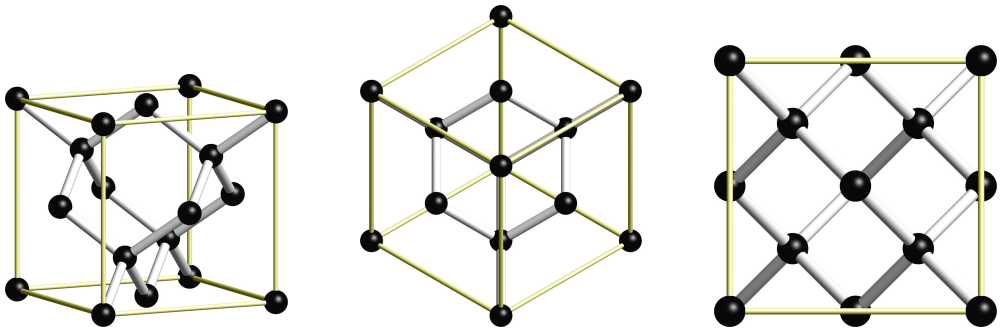

Figure 1.1: (a) Conventional unit cell for diamond. (b) Six-fold rotation symmetry upon propagation along [1,1,1] axis, and (c) four-fold rotation symmetry for propagation along [1,0,0] axis.

rotational symmetries. For these orientations, the unit cell has three-fold and four-fold symmetries, respectively. Linearly polarized high harmonics for monochromatic light can be generated for any orientation. For circularly polarized light the dynamical symmetry $\left(\varphi \to \varphi + \frac{2\pi}{N}, t \to \frac{2\pi}{N\omega}\right)$ for a system with N–fold symmetry, however, ensures that only harmonics of order $nN \pm 1$ are generated [1], where n is a positive integer.

Rabi oscillations

Rabi oscillations occur when a resonant or near-resonant oscillating field interacts with a system with quantized energy levels. The dynamics depend on the frequency of the field ω_{L}, the transition frequency of the system $E_{\mathrm{g}}/\hbar$, and the field strength $\Omega_0 = F_0 d/\hbar$. d is the projection of the dipole moment between the two energy levels on the direction of the field, and F is the magnitude of the field. For the near-resonant transitions, the detuning $\Delta = \omega_{\mathrm{L}} - E_{\mathrm{g}}/\hbar$ has to be considered as well, as it affects the Rabi frequency at which population is transferred, and limits the maximal fraction of population that can be transferred. A non-vanishing detuning modifies the frequency at which the population transfer occurs: $\Omega_R = \sqrt{\Omega_0^2 + \Delta^2}$.

Rabi oscillations are particularly important for two-level systems, where it is possible to reversibly transfer the whole population from one state to the other using monochromatic light with resonant and weak fields, $\hbar\omega_L = E_g \gg \mathbf{F} \cdot \mathbf{d}$. For light propagating in a medium of two-level systems it is also possible to observe self-induced transparency, where electrons are perfectly excited and de-excited by a pulse which has an 'area' of 2π. The 'area' of the applied pulse can be defined as:

$$\mathcal{A} = \int_{-\infty}^{\infty} dt \sqrt{|\Omega_R(t)|^2 + \Delta^2}. \tag{1.43a}$$

Such self-induced transparency is only known to occur for a limited number of pulse shapes. Intraband effects, presence of multiple energy levels and dephasing are however expected to prevent self-induced transparency in many types of solids.

Chapter 2

Gauge invariance

Two aspects of the dynamics are highlighted in this chapter, namely the issue of gauge invariance and the inclusion of phenomenological decoherence. While *ab initio* data has been successfully used in the past to predict optical properties of solids, one of the novelties in this work is to formulate a gauge-independent approach that allows for the inclusion of phenomenological dephasing.
For system of pure states, this is mostly a review of the literature. It is then followed up by introducing novel, generalized equations of motion for open systems. At this point, the interaction with the environment is described at a phenomenological level, in order to be consistent with the independent-particle approximation. As such, the interaction with the environment is not derived from first principles.

2.1 Electromagnetic gauge for dynamical calculations

Calculations involving an electromagnetic field can always be done for an arbitrary choice of gauge, with the two most common choices being the velocity gauge ($\phi \equiv 0$) and the length gauge ($\mathbf{A} \equiv 0$). In the length gauge, the physically, observable electric field $\mathbf{F}(\mathbf{r}, t)$ is contained entirely in the scalar potential $\phi(\mathbf{r}, t)$, whereas it is encoded entirely in the vector potential $\mathbf{A}(\mathbf{r}, t)$ in the velocity gauge. All physical observables are independent of the choice of gauge, but any approximation imposed on the equations to be solved may break gauge invariance. This includes discretization in time or space when solving the equations numerically. Approximations are often applied in order to keep calculations of complicated system feasible, and many approximations may break gauge invariance, which limits the validity of such approximations [36, 29, 31].
The gauge-dependent potentials are related to the physical field via

$$\mathbf{F}(t) = -\left(\nabla\phi(\mathbf{r}, t) + \frac{\partial \mathbf{A}(t)}{\partial t}\right). \tag{2.1}$$

From Eq. (2.1) it is clear that the two sets of fields $(\phi, \mathbf{A})$ and $(\phi + \partial_t X, \mathbf{A} - \nabla X)$ yield identical observables, where $X(\mathbf{r}, t)$ is an arbitrary function. This fact can be exploited to

change transform the fields from one gauge to another.
The dipole approximation is used throughout this work, and this approximation is equivalent to assuming the electric field is spatially homogeneous. Within this approximation, the fields can be expressed as the following simple four-vectors:

$$(\phi_{LG}, \mathbf{A}_{LG}) = (-\mathbf{F}(t) \cdot \hat{\mathbf{r}}, 0), \tag{2.2}$$

$$(\phi_{VG}, \mathbf{A}_{VG}) = (0, -\int_{-\infty}^{t} \mathbf{F}(t')dt'), \tag{2.3}$$

Eliminating either of the two potentials can simplify the numerical propagation significantly. Any intermediate gauge that contain both the scalar and the vector potential is also admissible, but inefficient as it requires evaluation of both the coordinate operator which appears in scalar potential, and the momentum operator which is coupled to the vector potential.

Several works have dealt with a real-time, quantum mechanical description of optical responses of bulk solids in the length gauge [132, 7] and the velocity gauge [12]. Each method suffers from its own drawbacks, and remedies are often based on the choice of gauge. Self-energies, non-local potentials and decoherence are more naturally handled in the length gauge, as this gauge is less likely to introduce numerical artifacts when gauge invariance is broken by the terms added to the dynamical equations.
The length gauge requires evaluation of the coordinate operator, which turns to a derivative operator with respect to the crystal momentum in reciprocal space. This can be problematic because the cell-periodic part of the wave functions $|u_{n\mathbf{k}}\rangle$ are not necessarily smooth functions of $\mathbf{k}$. The issue may be handled by normalizing the phases of the wave functions ad hoc, or by introducing a covariant derivative. This approach is generally only applicable to pure states. While there is no need to evaluate derivatives when using the velocity gauge, care has to be taken when introducing relaxation operators in order to preserve the physical properties. As mentioned before, the velocity gauge is more likely to introduce numerical artifacts when gauge invariance is broken. This is partly due to the fact that a larger part of the Hilbert space gets populated during the exposure to an electric field when the wave functions are expanded in the basis of the field-free states. Another reason why calculations performed in the velocity gauge are more sensitive towards violation of gauge invariance, is that the observables are calculated as a sum over gauge dependent terms. Evaluation of the observables therefore relies on an exact cancellation of the gauge dependent terms of the sum. It is an open question whether a universal and practical scheme that treats optical responses at a quantum mechanical level for particles in periodic potentials in any arbitrary gauge exists.

Gauge invariance must also hold for open systems, where the system under consideration interacts with an environment and slowly decohere. The literature tends to favor implementations in the length gauge, where all coherence terms decay at constant rates [106]. Naively applying such constant decay rates to velocity gauge calculations, would

	Pure state	Mixed state
Ad hoc	Semiconductor Bloch Equations using finite difference	Semiconductor Bloch Equations using finite difference
Ab initio	Covariant derivative based on the modern theory of polarization	Proposed method based on the covariant derivative

Table 2.1: Overview of approaches to solve the master equation in the length gauge. Matrix elements can be obtained *ad hoc* or *ab initio*, and the system under consideration can either be of pure states or mixed states.

lead to field-dependent decoherence rates [68], which are hard to interpret physically, and such terms may break the symmetries of the potential. Despite these technical difficulties, naive applications can still be found in the recent literature [61]

If the vector potential in the gauge under consideration is non-zero, the Thomas-Reiche-Kuhn sum rule needs to be satisfied in order to even evaluate the leading-order response correctly. This generally prohibits the use of ad hoc matrix elements, such as those found in tight-binding models. If the sum rule is not satisfied, the dispersion relation experienced by each electron can deviate significantly from the actual bands and thus lead to spurious electric currents.

The situation is different in the length gauge. In fact, the use of ad hoc matrix elements can be beneficial for solving the semiconductor Bloch equations, because the phases of the matrix elements can be chosen to be smooth functions of the crystal momentum. In the simplest cases, the matrix elements can be chosen to be constant and independent of the crystal momentum.

An overview of various approaches to solve the equation of motion in the length gauge is given in Table 2.1. To solve the Schrödinger and master equation using *ab initio* data, it is useful to implement covariant derivatives which can be determined from the modern theory of polarization [116].

Solutions for evolving the dynamics with pure states are well known and will be reviewed first in the next section. A method for simulating the dynamics of a mixed systems in the length gauge using *ab initio* data is more difficult, and part of the work for this thesis has been to propose a solution to this problem.

In the velocity gauge, propagation of wave functions at different $\mathbf{k}$ are independent of each other as long as no additional coupling is present. Such couplings may arise from e.g. two-body collisions or screening. For length gauge calculations, significantly fewer bands are needed to correctly reproduce motion of the wave functions, but fine $\mathbf{k}$-meshes are needed for numerical stability. In cases where a constant field is applied for times long enough for electrons to move several Brillouin zones in reciprocal space, length gauge

calculations are expected to be superior, as the periodicity in reciprocal space is explicitly enforced. Periodicity is not guaranteed in the velocity gauge, and a very large number of bands would be required to correctly describe displacements up to multiple Brillouin zone lengths. As electric fields produced by pulses oscillate, the electrons are, however, only expected to be displaced by one Brillouin zone at most.

Whenever the electromagnetic interaction between fields and solids can be described with plane waves, the fields and the transition matrix elements have simple relations. Capturing the effects of intraband motion necessitates a proper description of gauge invariance.

2.2 Hamiltonian dynamics

In this section the relevant equations of motion for Hamiltonian dynamics are presented together with various approaches for solving the equations in the length and velocity gauge. Approaches dealing with mixed systems and gauge transformation of decoherence terms are deferred to Section 2.3.

Quantum coherence is conserved in quantum mechanical systems when interactions with an external environment is absent The equation of motion is the time-dependent Schrödinger equation, which is simpler and require less variables than the master equation used for mixed systems. The length gauge is considered first. Working in the length gauge allows for a simpler interpretation of the instantaneous probability amplitudes than in the velocity gauge. It also has the advantage that physical meaningful results can be obtained with relatively few bands [129]. Because of the simple interpretation of the probability amplitudes, it is possible to separate contributions to the polarization and the current into *inter*band and *intra*band.

2.2.1 Length gauge

Semiconductor Bloch Equation

Various approaches exist to calculate the dynamics in the length gauge, and two of the approaches are used in this work. The first approach is to express the equation as the semiconductor Bloch equations. Following Blount [18], the coordinate space operator is decomposed into two separate terms $\mathbf{r} = \mathbf{r}_{\text{inter}} + \mathbf{r}_{\text{intra}}$, where the intraband operator is calculated as a finite difference between neighboring $\mathbf{k}$-points. This approach implicitly assumes that the cell-periodic part of the wave functions are smooth with respect to $\mathbf{k}$. The semiconductor Bloch equation is of the form

$$i\hbar\partial_t|u_{n\mathbf{k}}(t)\rangle = \hat{H}_{\mathbf{k}}|u_{n\mathbf{k}}(t)\rangle + q\mathbf{F}(t)\cdot\hat{\mathbf{d}}_{\mathbf{k}}|u_{n\mathbf{k}}(t)\rangle + iq\mathbf{F}(t)\cdot\nabla_{\mathbf{k}}|u_{n\mathbf{k}}(t)\rangle. \tag{2.4}$$

Determining the electron dynamics thus reduces to solving a set of partial differential equations driven by an external force. It is useful when the matrix elements are taken ad hoc, or when dealing with certain systems where the phase of *ab initio* matrix elements can be adjusted in an ad hoc manner to make them continuous and differentiable with respect to $\mathbf{k}$.
Similarly to the coordinate operator, the velocity operator can also be decomposed into inter- and intraband components. The current density is then determined as

$$\mathbf{J} = \frac{q}{V}\sum_n \langle u_{n\mathbf{k}}|\hat{\mathbf{v}}_{\mathbf{k}}|u_{n\mathbf{k}}\rangle = \frac{q}{V}\sum_n \langle u_{n\mathbf{k}}|\hat{\mathbf{v}}_{\mathbf{k},\text{inter}}|u_{n\mathbf{k}}\rangle + \frac{q}{V}\sum_n \langle u_{n\mathbf{k}}|\hat{\mathbf{v}}_{\mathbf{k},\text{intra}}|u_{n\mathbf{k}}\rangle \tag{2.5}$$

If the time-dependent wave functions are expanded in the basis of stationary wave functions

$$|u_{n\mathbf{k}}(t)\rangle = \sum_m |u^0_{m\mathbf{k}}\rangle c_{mn}(t), \tag{2.6}$$

the current densities are then given as

$$\mathbf{J}_{\text{intra}}(t) = -\frac{e}{V}\sum_{n}\langle u_{n\mathbf{k}}|\hat{\mathbf{v}}_{\mathbf{k},\text{intra}}(\nabla_{\mathbf{k}}H_{0,\mathbf{k}})|u_{n\mathbf{k}}\rangle = -\frac{e}{Vm}\sum_{n,m}|c_{mn\mathbf{k}}|^2\nabla_{\mathbf{k}}\partial E_{m\mathbf{k}} \tag{2.7}$$

$$\mathbf{J}_{\text{inter}}(t) = -\frac{e}{V}\sum_{n\neq m}\langle u_{n\mathbf{k}}|\hat{\mathbf{v}}_{\mathbf{k},\text{inter}}|u_{m\mathbf{k}}\rangle = -\frac{2e}{V}\sum_{n}\sum_{l>m}\text{Re}\left\{c^*_{ln\mathbf{k}}c_{mn\mathbf{k}}\mathbf{v}_{lm}\right\}. \tag{2.8}$$

In the absence of an external field, the intraband current is constant whereas the interband contribution oscillates with the separation energies. These contributions to high harmonic generation can have different time-frequency spectrograms [148].

Whenever the stationary wave functions and the matrix elements of the interband part of the coordinate operator $\mathbf{r}_{\text{inter}}$ are not smooth functions of $\mathbf{k}$, it is beneficial to express the coordinate matrix as a covariant derivative instead. The covariant derivative can be derived using the formalism from the modern theory of polarization. Several approaches exist to numerically calculate the derivative, and alternative methods are based on introducing a generalized derivative [8], or link operators [132]. Resorting to an ordinary finite difference scheme to approximate the derivative is only possible if the wave functions are smooth functions of $\mathbf{k}$. A particularly simple choice for continuous ad hoc matrix elements is to use $\mathbf{k}$-independent values, and several results in the literature have been derived under the assumption of constant, $\mathbf{k}$-independent transition matrix elements [128, 106]. Generalized derivatives have only been demonstrated for evaluation of nonlinear susceptibilities. Link operators suffers from a serious drawback in that they do not have the same periodicity as the Brillouin zone. Consequently, working with the covariant derivative is the most attractive choice.

Lagrangian approach based on the geometric phase

Within the framework of the modern theory of polarization, the polarization response is determined from the geometric phase. The geometric phase associated with unitary motion along a path $\mathcal{C}$ parameterized with $\theta \in [0, \Theta]$ is [113]

$$\gamma = \arg\langle\psi(0)|\psi(\Theta) + i\int_0^{\Theta}\langle\psi(\theta)|\partial_\theta\psi(\theta)\rangle d\theta. \tag{2.9}$$

For electrons in periodic potentials, the wave functions are parameterized by the crystal momentum $\mathbf{k}$, and the path in the Brillouin zone can be parallel to one of the reciprocal lattice vectors. The cell-periodic part of the wave functions can usually be chosen to be periodic functions of the crystal momentum, so $|u_{n\mathbf{k}+\mathbf{b}_i}\rangle = |u_{n\mathbf{k}}\rangle$, where $\mathbf{b}_i$ is a reciprocal lattice vector. A line integral from $\mathbf{k}$ to $\mathbf{k}+\mathbf{b}_i$ therefore corresponds to a loop, and can be determined by the integral in Eq. (2.9). Considering a single electronic band n, the geometric phase along for wave functions with these end points is

$$\gamma_{n,\mathbf{k}_0,i} = i\int_0^{|\mathbf{b}_i|} dk\langle u_{n,\mathbf{k}_0+k\hat{\mathbf{b}}_i}|\partial_k|u_{n,\mathbf{k}_0+k\hat{\mathbf{b}}_i}\rangle \tag{2.10}$$

where $\hat{\mathbf{b}}_i$ is the unit vector of the reciprocal space vector. In order to calculate the geometric phase on a discretized grid, the integral can be divided into a sum of integrals:

$$\gamma_{n,\mathbf{k}_0,i} = i \sum_{\mathbf{k}=\mathbf{k}_0}^{\mathbf{k}-\Delta\mathbf{k}} \int_0^1 dq \langle u_{n\mathbf{k}+q\Delta\mathbf{k}} | \partial_q | u_{n\mathbf{k}+q\Delta\mathbf{k}} \rangle \tag{2.11}$$

$$= \frac{i}{2} \sum_{\mathbf{k}=\mathbf{k}_0}^{\mathbf{k}-\Delta\mathbf{k}} \int_0^1 dq \langle u_{n\mathbf{k}} | \partial_q u_{n\mathbf{k}+q\Delta\mathbf{k}} \rangle - \langle \partial_q u_{n\mathbf{k}+q\Delta\mathbf{k}} | u_{n\mathbf{k}} \rangle + \mathcal{O}(|\Delta\mathbf{k}|^2) \tag{2.12}$$

$$= \sum_{\mathbf{k}=\mathbf{k}_0}^{\mathbf{k}-\Delta\mathbf{k}} \mathrm{Im} \left\{ \int_0^1 dq \partial_q \log \langle u_{n\mathbf{k}} | u_{n\mathbf{k}+q\Delta\mathbf{k}} \rangle \right\} + \mathcal{O}(|\Delta\mathbf{k}|^2) \tag{2.13}$$

$$= \sum_{\mathbf{k}=\mathbf{k}_0}^{\mathbf{k}-\Delta\mathbf{k}} \mathrm{Im} \left\{ \log \langle u_{n\mathbf{k}} | u_{n\mathbf{k}+\Delta\mathbf{k}} \rangle \right\} + \mathcal{O}(|\Delta\mathbf{k}|^2), \tag{2.14}$$

where the sum is over evenly space points $\mathbf{k} = \mathbf{k}_0 + j\Delta\mathbf{k}$ for positive integers j. The local contributions to the geometric phase, $\varphi_{n\mathbf{k}\alpha} = \mathrm{Im}\{\log\langle u_{n\mathbf{k}} | u_{n\mathbf{k}+\Delta\mathbf{k}_\alpha} \rangle\}$ are gauge-dependent, but the sum over the line integral is gauge-independent. Gauge independence arises as a consequence of the periodicity of the Brillouin zone, which effectively causes the integral to be over a closed loop. A similar approach can be applied to the many-body wave function $|\Psi_\mathbf{k}\rangle$ for N_V occupied valence bands, where the overlaps between the many-body wave function at neighboring $\mathbf{k}$-points are calculated as [98]

$$\langle \Psi_\mathbf{k} | \Psi_{\mathbf{k}+\Delta\mathbf{k}} \rangle = \det \begin{vmatrix} \langle \phi_{1,\mathbf{k}} | \phi_{1,\mathbf{k}+\Delta\mathbf{k}} \rangle & \cdots & \langle \phi_{1,\mathbf{k}} | \phi_{N_V,\mathbf{k}+\Delta\mathbf{k}} \rangle \\ \vdots & \ddots & \vdots \\ \langle \phi_{N_v,\mathbf{k}} | \phi_{1,\mathbf{k}+\Delta\mathbf{k}} \rangle & \cdots & \langle \phi_{N_V,\mathbf{k}} | \phi_{N_V,\mathbf{k}+\Delta\mathbf{k}} \rangle \end{vmatrix}. \tag{2.15}$$

The geometric phase enters the expression for the polarization via the derivative operator:

$$\mathbf{P}(t) = \frac{1}{V} \sum_n \int_{V_{\mathrm{BZ}}} d\mathbf{k} \, \langle u_{n\mathbf{k}} | q\hat{\mathbf{r}} | u_{n\mathbf{k}} \rangle \tag{2.16}$$

$$= \frac{q}{V} \sum_n \int_{V_{\mathrm{BZ}}} d\mathbf{k} \, \langle u_{n\mathbf{k}} | i\nabla_\mathbf{k} | u_{n\mathbf{k}} \rangle \tag{2.17}$$

In order to obtain the polarization response, a sum over all spatial directions is required at each $\mathbf{k}$-point. For each Bloch function or set of degenerate Bloch functions, the polarization can be obtained from the discretized formula for the geometric phase [62]:

$$\mathbf{P}(t) = \frac{q}{2\pi V N_k} \sum_\alpha N_\alpha \mathbf{R}_\alpha \mathrm{Im}\{\log \prod_k \det S_{\alpha,k,k+1}\}$$

$$= \frac{q}{2\pi V N_k} \sum_\alpha \sum_k N_\alpha \mathbf{R}_\alpha \mathrm{Im}\{\log \det S_{\alpha,k,k+1}\}, \tag{2.18}$$

where $\mathbf{R}_\alpha$ is the lattice vector, N_α is the number of $\mathbf{k}$-points along the corresponding reciprocal vector and N_k is the total number of $\mathbf{k}$-points in the Brillouin zone. The current density can then be determined as the temporal derivative of the polarization:

$$\mathbf{J}(t) = \frac{q}{2\pi V N_k} \sum_{\mathbf{k}} \sum_{\alpha} N_\alpha \mathbf{R}_\alpha \mathrm{Tr}\left[S^{-1}_{\mathbf{k},\mathbf{k}+\Delta\mathbf{k}_\alpha} \frac{\partial}{\partial t} S_{\mathbf{k},\mathbf{k}+\Delta\mathbf{k}_\alpha} \right]. \tag{2.19}$$

The current obtained from the geometric phase is identical to the expectation value of the current operator Eq. (2.5), which can be shown when calculating the expectation value using pure states. While the current in Eq. (2.5) can be evaluated unambiguously for any arbitrary distribution, the geometric phase is only applicable to systems where bands are initially uniformly occupied. This is one of the drawbacks when determining the polarization from the geometric phase. The determinants evaluated in Eq. (2.18) are generally complex-valued, which can lead to ambiguities when evaluating the logarithm. For this reason Eq. (2.19) is preferred when analyzing the polarization response.

Having defined the polarization and current in terms of the geometric phase, the Euler-Lagrange equations can be derived in order to obtain the equations of motion. This leads to a well-known expression for the covariant derivative, which provides a systematic way of calculating the derivative operator for pure states [116].
The Lagrangian can be obtained from a Legendre transformation of the Hamiltonian with respect to the variables $|u_{n\mathbf{k}}\rangle$ and $|\dot{u}_{n\mathbf{k}}\rangle$ as

$$\begin{aligned}\mathcal{L}(t) &= i\hbar \sum_{n}^{N_V} \sum_{\mathbf{k}} \langle u_{n\mathbf{k}} | \dot{u}_{n\mathbf{k}} \rangle - \langle u_{n\mathbf{k}} | \hat{H}_{\mathbf{k}}(t) | u_{n\mathbf{k}} \rangle \\ &= i\hbar \sum_{n}^{N_V} \sum_{\mathbf{k}} \langle u_{n\mathbf{k}} | \dot{u}_{n\mathbf{k}} \rangle - \langle u_{n\mathbf{k}} | \hat{H}_{0,\mathbf{k}}(t) | u_{n\mathbf{k}} \rangle - \langle u_{n\mathbf{k}} | \mathbf{E}(t) \cdot \hat{\mathbf{P}}_{\mathbf{k}} | u_{n\mathbf{k}} \rangle.\end{aligned} \tag{2.20}$$

where $\hat{\mathbf{P}}_{\mathbf{k}} = q\hat{\mathbf{r}}_{\mathbf{k}}$ is the polarization operator. The equation of motion can then be determined as

$$\frac{\partial}{\partial t}\left(\frac{\partial \mathcal{L}}{\partial \langle \dot{u}_{n\mathbf{k}}|} \right) = \frac{\partial \mathcal{L}}{\partial \langle u_{n\mathbf{k}}|}. \tag{2.21}$$

With the help of Eq. (2.18) for the polarization of the discretized system, the functional derivative of the polarization becomes:

$$\begin{aligned}\frac{\delta \mathbf{P}(t)}{\delta \langle u_{n\mathbf{k}}|} &= \frac{q}{2\pi V N_k} \sum_{\alpha} \sum_{\mathbf{q}} N_\alpha \mathbf{R}_\alpha \;\; \frac{\delta}{\delta \langle u_{n\mathbf{k}}|} \left(\log\det S_{\mathbf{q},\mathbf{k}+\Delta\mathbf{k}_\alpha} - \log\det S^*_{\mathbf{q},\mathbf{k}+\Delta\mathbf{k}_\alpha} \right) \\ &= \frac{q}{2\pi V N_k} \sum_{\alpha} N_\alpha \mathbf{R}_\alpha \sum_{m} \{ (S^{-1}_{\mathbf{k},\mathbf{k}+\Delta\mathbf{k}_\alpha})_{mn} | u_{m\mathbf{k}+\Delta\mathbf{k}_\alpha} \rangle - (S^{-1}_{\mathbf{k},\mathbf{k}-\Delta\mathbf{k}_\alpha})_{mn} | u_{m\mathbf{k}-\Delta\mathbf{k}_\alpha} \rangle \}\end{aligned} \tag{2.22}$$

The derivative is not linear in the wave functions, and requires an evaluation of the inverse matrix ($S^{-1}_{\mathbf{k},\mathbf{k}+\Delta\mathbf{k}_\alpha}$). This mixing of wave functions from different bands is, however, important for handling degenerate states.
If only a single occupied band is present, the equation reduces to

$$i\hbar|\dot{u}_{n\mathbf{k}}\rangle = \hat{H}_{0,\mathbf{k}}|u_{n\mathbf{k}}\rangle + \frac{q}{2\pi V N_k}\sum_\alpha N_\alpha \mathbf{E}(t)\cdot\mathbf{R}_\alpha\left(\frac{|u_{n\mathbf{k}+\Delta\mathbf{k}_\alpha}\rangle}{\langle u_{n\mathbf{k}}|u_{n\mathbf{k}+\Delta\mathbf{k}_\alpha}\rangle} - \frac{|u_{n\mathbf{k}-\Delta\mathbf{k}_\alpha}\rangle}{\langle u_{n\mathbf{k}}|u_{n\mathbf{k}-\Delta\mathbf{k}_\alpha}\rangle}\right). \quad (2.23)$$

2.2.2 Velocity gauge

One of the main advantages of the velocity gauge is that wave functions at each and every **k**-point is decoupled from wave functions at other **k**-points in the independent particle-approximation. Therefore, the equations of motion for each wave function can be solved independently, which makes it easy to distribute calculation over multiple isolated processors, when solving the equations numerically. it is also straightforward to simulate the dynamics on an irregular **k**-grid. This can be beneficial if only parts of the Brillouin zone need to be sampled. This can be the case if high resolution in certain parts of the zone is needed, or if it is sufficient to sample the zone at random. This can be particularly useful when calculating the response for a pulse propagating through a three-dimensional medium, since the set of randomly chosen **k**-points can be chosen differently at each point in real space. One of the drawbacks of the velocity gauge is that a large number of bands are required, and that the momentum matrix operator can be calculated accurately. Solving the dynamical equations in the velocity gauge require momentum matrix elements to a high precisions. This requires a large basis set when expanding the wave functions on a real-space grid in order to calculate the spatial derivatives accurately.

Once the diagonal Hamiltonian and momentum operator has been determined in the basis of stationary states, the calculation of the optical response reduces to solving a set of coupled differential equations. In the dipole approximation, $\mathbf{A}(\mathbf{r},t) = \mathbf{A}(t)$ and the Hamiltonian reads:

$$\hat{H} = \frac{(\hat{\mathbf{p}} - q\mathbf{A}(t))^2}{2m} + V(\hat{\mathbf{r}}) \tag{2.24}$$

$$= \frac{\hat{\mathbf{p}}^2}{2m} + V(\hat{\mathbf{r}}) - \frac{q}{m}\mathbf{A}(t)\cdot\mathbf{p} + \frac{q^2}{2m}\mathbf{A}^2(t) = \hat{H}_0 + \hat{H}_{\mathrm{int}}(t). \tag{2.25}$$

In the Schrödinger picture the TDSE has the generic form

$$i\hbar\frac{d}{dt}|\psi_{n\mathbf{k}}\rangle = (\hat{H}_0 + \hat{H}_{\mathrm{int}}(t))|\psi_{n\mathbf{k}}\rangle. \tag{2.26}$$

Transforming to the interaction picture removes the scalar terms, and reduces the systems of equations to an even simpler form:

$$\frac{\partial}{\partial t}|\tilde{\psi}_{n\mathbf{k}}\rangle = \frac{q}{m}\mathbf{A}(t)\cdot\tilde{\mathbf{p}}|\tilde{\psi_{n\mathbf{k}}}\rangle. \tag{2.27}$$

where $|\tilde{\psi}_{i,\mathbf{k}}\rangle = e^{\mathrm{i}\hat{H}_0 t/\hbar}|\psi_{i,\mathbf{k}}\rangle$, $\tilde{\hat{\mathbf{p}}}_{\mathbf{k}} = e^{\mathrm{i}\hat{H}_0 t/\hbar}\hat{\mathbf{p}}_{\mathbf{k}}e^{-\mathrm{i}\hat{H}_0 t/\hbar}$, and $\hat{H}_0$ is the unperturbed Hamiltonian. The electric current can be evaluated as

$$\mathbf{J}_{\hat{\mathbf{v}}}(t) = \frac{q}{V}\sum_{\mathbf{k}\in\mathrm{BZ}}\mathrm{Tr}[\hat{\mathbf{v}}_{\mathbf{k}}\hat{\rho}_{\mathbf{k}}] \tag{2.28}$$

where $\hat{\mathbf{v}}_{\mathbf{k}} = (\hat{\mathbf{p}}_{\mathbf{k}} - q\mathbf{A}(t))/m$. If the Thomas-Reiche-Kuhn sum rule is satisfied for all valence bands and all of the conduction bands that get populated during excitation, it is

sufficient to propagate the wave functions and evaluate the observables using Eq. (2.28). For three-dimensional potentials, a very large number of bands might be needed, which may limit the applicability of the approach. One of the difficulties with the velocity gauge is that an incomplete basis not only affects the wave functions when solving the numerical calculations, it also has a direct impact on the evaluation of observables. The observables, such as the absorbed energy and the velocity, depends on a sum of gauge-dependent quantities. Since the individual gauge-dependent terms can be several times larger than the sum, small deviations in either of the gauge-dependent terms can lead to to large errors. This issue is addressed in Section 3.4.

Although the dynamics at each $\mathbf{k}$-point is independent of wave functions at other $\mathbf{k}$-points, it is still necessary to sample a large number of $\mathbf{k}$-points to ensure convergence. Whenever the vector potential is non-zero, all electrons have their crystal momentum shifted by $\Delta\mathbf{k} = q\mathbf{A}(t)$. Even if all electrons remain in the fully occupied valence bands, a current can still be observed if the currents generated at each $\mathbf{k}$-point due to the displacement do not cancel out. This will be the case if the $\mathbf{k}$-grid is sparse. Thus it is important to determine the magnitude of the spurious current to ensure that it will be orders of magnitude lower than the physical current. One way of eliminating the spurious current is by subtracting the corresponding adiabatically induced current. The contribution from valence band electrons that are displaced adiabatically is calculated by obtaining the a unitary transformation matrix that translates the electrons in reciprocal space, and calculate the corresponding momentum the electrons obtain due to the displacement. Such a unitary matrix $\hat{U}_{\mathbf{k},\mathbf{k}+q\mathbf{A}(t)}$, which shifts the crystal momentum of an electron from $\mathbf{k}$ to $\mathbf{k} + q\mathbf{A}(t)$ can be calculated by constructing the non-diagonal Hamiltonian $\tilde{H}_{\mathbf{k}+q\mathbf{A}(t)}$:

$$\tilde{H}_{\mathbf{k}+\mathbf{A}(t)} = \hat{H}_0 + \frac{q}{m}\mathbf{A}(t)\cdot\hat{\mathbf{p}} + \frac{q^2}{2m}A^2(t) \tag{2.29}$$

A non-unique unitary matrix can then be determined via numerical diagonalization:

$$\tilde{H}_{\mathbf{k}+q\mathbf{A}(t)} = \hat{U}_{\mathbf{k},\mathbf{k}+q\mathbf{A}(t)}\hat{H}_{\mathbf{k}+\mathbf{A}(t)}\hat{U}^{\dagger}_{\mathbf{k},\mathbf{k}+q\mathbf{A}(t)} \tag{2.30}$$

The following correction term therefore needs to be subtracted from the velocity of each electron:

$$\mathbf{v}_{\mathbf{k},\text{correction}}[\mathbf{A}(t)] = \text{Tr}\left(\hat{\rho}_{0,\mathbf{k}}\hat{U}_{\mathbf{k},\mathbf{k}+q\mathbf{A}(t)}\hat{\mathbf{v}}_{\mathbf{k}}\hat{U}^{\dagger}_{\mathbf{k},\mathbf{k}+q\mathbf{A}(t)} - \hat{\rho}_{0,\mathbf{k}}\hat{\mathbf{v}}_{\mathbf{k}}\right). \tag{2.31}$$

where $\rho_{0,\mathbf{k}}$ is the ground state density matrix. For weak fields this correction behaves as $N_{\text{eff}}\mathbf{A}(t)$, i.e. as a constant times the vector potential. For stronger fields a noticeable deviation occurs, and the simple expression would overestimate the correction term. This expression alleviates problems with the real-time polarization response when the grid is too coarse.

2.3 Open systems

In this section, first dephasing operators are considered, and afterwards the gauge transformation of a suitable class of such operators are considered. In the later subsections, the dynamical equations in the two gauges are reviewed, which includes the proposed scheme of solving the equations of motion in the length gauge for an open system.

To describe a mixed state, it is either necessary to work with an ensemble of wave functions or equivalently describe the systems in terms of a density matrix:

$$\hat{\rho} = \sum_n p_n |\psi_n\rangle\langle\psi_n|. \tag{2.32}$$

E.g. if a system of electrons is in a thermal state, the weights p_n correspond to to the Fermi-Dirac weights. An important feature of Hamiltonian dynamics is that if the wave functions are initially orthogonal, they will remain so forever. In addition, the weights of the wave functions do not change over time. The introduction of non-Hermitian terms causes the weights to change over time, and the wave function are no longer expected to be fully orthogonal. Instead, an orthogonal set of states can be constructed as a linear combination of the wave functions. The weight of these linear combinations change over time due to the non-Hermitian terms.

The master equation governs the dynamic for a mixed state. It can be derived for a system composed of the sub-system under consideration and an environment that acts as a bath. The sub-system and the environment interacts via a weak coupling $\hat{H}_I$, and the coupling must be sufficiently weak that the bath remains in its unperturbed state. The density matrix is then formally factored into the density matrix for the system and for the bath

$$\hat{\rho} = \hat{\rho}_S \otimes \hat{\rho}_B, \tag{2.33}$$

and then Hamiltonian is formally composed of parts that act on either of the two subsystems

$$\hat{H} = \hat{H}_S + \hat{H}_I + \hat{H}_B. \tag{2.34}$$

Various approaches to derive the master equation exists, and they generally rely on the Markov approximation. For the single-particle master equation, the Lindblad formalism can be applied to ensure that the trace and the positive semi-definiteness of the density matrix are preserved [74]. In the Lindblad formalism, interaction with the environment is done by introducing a superoperator,

$$\hat{\mathcal{L}}(\hat{\rho}) = \sum_\alpha \hat{L}_\alpha \hat{\rho} \hat{L}_\alpha^\dagger - \frac{1}{2}(\hat{L}_\alpha^\dagger \hat{L}_\alpha \hat{\rho} + \hat{\rho} \hat{L}_\alpha^\dagger \hat{L}_\alpha), \tag{2.35}$$

which is included in the master equation:

$$\mathrm{i}\hbar \partial_t \hat{\rho} = [\hat{\rho}, \hat{H}] + \mathrm{i}\hat{\mathcal{L}}(\hat{\rho}). \tag{2.36}$$

One of the advantages of introducing the Lindblad operators L_α is that the trace and the positive semi-definiteness of the density matrix are conserved regardless of the choice of operator. The next step is therefore to find an operator that represents a possible, and physically admissible dephasing mechanism. Since it is easier to interpret the meaning of decoherence operator in the length gauge, it is beneficial to express the Lindblad operator in the length gauge, and apply a gauge transformation to obtain the operator in the velocity gauge.

To this end, one can use operators of the form

$$\hat{L}_{LG} = f(\hat{\mathbf{p}}, \hat{H}_0), \tag{2.37}$$

when expressed in the length gauge. I.e. the Lindblad operator is an operator function that depends on the momentum operator and the Hamiltonian. The transformation between the gauges is known to be $\hat{U} = \exp(\mathrm{i}q\mathbf{A}(t)\cdot\hat{\mathbf{r}})$. As long as the electric field is homogeneous, the Lindblad operator transforms as

$$\hat{L}_{VG} = f\left(\hat{\mathbf{p}} - q\mathbf{A}(t), \hat{H}_0 - \frac{q}{m}\mathbf{A}\cdot\hat{\mathbf{p}} + \frac{q^2}{2m}A^2(t)\right). \tag{2.38}$$

Having a Lindblad operator that is exact in both gauges allows for rigorous comparisons of the two gauges. In the rest of the section, an explicit choice of the function f is used. In order to model decoherence that does not cause interband relaxation, the Lindblad operator is chosen to have the form

$$\hat{L}_{LG} = \sqrt{\gamma}\hat{H}_0. \tag{2.39}$$

This choice leads to energy-dependent dephasing rates, and keeps the model simple to solve numerically. This choice of Lindblad operator trivially commutes with the Hamiltonian, so it does not affect the energy of the system by spontaneously exciting electrons from one band to another. While the choice of Lindblad operator might seem arbitrary, it is no more arbitrary than what is commonly used in the literature. In fact, it is equivalent to the $\hat{\sigma}_z$ Pauli matrix, which is often used in the special case of a two-dimensional Hilbert space [38]. In addition, it has the property that coherence between degenerate states does not decay. In the length gauge, the off-diagonal $\rho_{\mathrm{LG},ij}$ terms decay at constant rates, with the rates depending on the energy differences of the states, i.e.

$$\mathcal{L}(\hat{\rho}_{\mathrm{LG}})_{ij} = -(\gamma/2)(E_i - E_j)^2\hat{\rho}_{\mathrm{LG},ij}. \tag{2.40}$$

In the velocity gauge it thus reads:

$$\hat{L}_{VG} = \sqrt{\gamma}\hat{U}\hat{H}_0\hat{U}^\dagger = \sqrt{\gamma}\left(\hat{H}_0 - \frac{q}{m}\mathbf{A}\cdot\hat{\mathbf{p}} + \frac{q^2}{2m}A^2(t)\right). \tag{2.41}$$

The physical origin of such a dephasing operator is determined by considering a system of electrons interacting with a bath of bosons. The system interacts with the bosons via the

annihilation operator b_n and creation operator $b_n^\dagger$. Such bosons can represent e.g. phonons. In the absence of an external electric field, the Hamiltonian of the combined system is then

$$\hat{\mathcal{H}} = \hat{H}_0 + \sum_n \mathcal{E}_n \hat{b}_n^\dagger \hat{b}_n + \sum_n \hat{H}_0(\gamma_n \hat{b}_n^\dagger + \gamma_n^* \hat{b}_n), \tag{2.42}$$

where $\hat{H}_0$ governs the Bloch electrons, $\sum_n \mathcal{E}_n \hat{b}_n^\dagger \hat{b}_n$ governs the dynamics of the bosons, and $\hat{H}_I = \sum_n \hat{H}_0(\gamma_n \hat{b}_n^\dagger + \gamma_n^* \hat{b}_n)$ describes the interaction of electron with the bosonic bath.

In the next step, the bath is assumed to be sufficiently large that the effect of the system onto the bath is negligible. It is also assumed that the external electric field does not affect the underlying dephasing mechanism.

Transforming the Hamiltonian into the interaction picture with respect to the bath yields

$$\begin{aligned}
\hat{\mathcal{H}} &= \hat{H}_0 + \sum_n H_0(\gamma_n \hat{b}_n^\dagger e^{i\mathcal{E}_n t} + \gamma_n^* \hat{b}_n e^{-i\mathcal{E}_n t}), \\
&\approx \hat{H}_0 \left[1 + 2 \sum_n |\gamma_n| \sqrt{N_n} \cos(\mathcal{E}_n t + \arg\gamma_n) \right] \\
&= \hat{H}_0 \left[1 + \eta(t) \right],
\end{aligned} \tag{2.43}$$

where $\eta(t)$ is a fluctuating function that depends on the coupling strengths γ_n. The bosonic eigenvalues are denoted $\mathcal{E}_n$ and occupation numbers are denoted as $N_n \gg 1$. Within the approximation encoded in Eq. (2.43), the effect of the bath on the system is to multiply the energies with $\lambda(t) = 1 + \eta(t)$. Such a modulation can result from the uniform deformation of a lattice potential:

$$\begin{aligned}
\hat{H}_{\lambda(t)} &= \frac{-\hbar^2}{2m} \nabla_{\mathbf{r}}^2 + \lambda(t) \hat{V}_{\mathrm{KS}} \left(\sqrt{\lambda(t)} \mathbf{r} \right) \\
&= \lambda(t) \left[\frac{-\hbar^2}{2m} \nabla_{\mathbf{s}}^2 + \hat{V}_{\mathrm{KS}}(\mathbf{s}) \right],
\end{aligned} \tag{2.44}$$

where $\mathbf{s} = \sqrt{\lambda(t)}\mathbf{r}$. If Bloch functions adiabatically follow changes of the lattice potential, their energies will be modulated with $\lambda(t)$. This may serve as a very rough model of a breather mode of lattice vibrations. It should, however, be kept in mind that a Kohn-Sham potential V_{KS} contains the Hartree potential and exchange-correlation potentials arising from the interaction with the other electrons in addition to the bare lattice potential.

The function $\eta(t)$ represents the time-dependent, stochastic deformation of the potential, where the randomness arises from the phase of the complex-valued coupling factors γ_n. In the limiting case of a stochastic function with a white noise spectrum, averaging over all possible realizations of $\eta(t)$ yields $\langle \eta(t) \rangle_\eta = 0$ and $\langle \eta(t)\eta(t') \rangle_\eta = \frac{1}{\tau}\delta(t - t')$. For

each realization of $\eta(t)$, the wave functions can formally be propagated in time as

$$\begin{aligned}|\psi_n(t+\Delta t)\rangle &= \hat{\mathcal{U}}(t+\Delta t,t)|\psi_n(t)\rangle \\ &\approx \left(1-\frac{i}{\hbar}\hat{H}_0\Delta t-\frac{i}{\hbar}\hat{H}_0\int_t^{t+\Delta t}dt'\eta(t')-\frac{1}{\hbar^2}\hat{H}_0^2\int_t^{t+\Delta t}dt'\int_t^{t'}dt''\eta(t')\eta(t'')\right)|\psi_n(t)\rangle,\end{aligned} \tag{2.45}$$

where only terms containing Δt to first order have been kept. The evolution of the density matrix is then:

$$\begin{aligned}\hat{\rho}(t+\Delta t) &= \left\langle\sum_n|\psi_n(t+\Delta t)\rangle\langle\psi_n(t+\Delta t)|\right\rangle_\eta = \left\langle\mathcal{U}(t+\Delta t,t)\rho(t)\mathcal{U}^\dagger(t+\Delta t,t)\right\rangle_\eta \\ &\approx \left\langle\left(1-\frac{i}{\hbar}H_0\Delta t-\frac{i}{\hbar}H_0\int_t^{t+\Delta t}dt'\eta(t')-\frac{1}{\hbar^2}H_0^2\int_t^{t+\Delta t}dt'\int_t^{t'}dt''\eta(t')\eta(t'')\right)\right. \\ &\quad \left.\rho(t)\left(1+\frac{i}{\hbar}H_0\Delta t+\frac{i}{\hbar}H_0\int_t^{t+\Delta t}dt'\eta(t')-\frac{1}{\hbar^2}H_0^2\int_t^{t+\Delta t}dt'\int_t^{t'}dt''\eta(t')\eta(t'')\right)\right\rangle_\eta \\ &\approx \rho(t)-\frac{i}{\hbar}[H_0,\rho(t)]\Delta t+\frac{\gamma}{2}\left(H_0\rho(t)H_0-\frac{1}{2}H_0^2\rho(t)-\frac{1}{2}\rho(t)H_0^2\right)\Delta t.\end{aligned} \tag{2.46}$$

At the last step, the terms quadratic in Δt have been dropped, and the following relation is used:

$$\left\langle\int_t^{t+\Delta t}dt'\int_t^{t'}dt''\eta(t')\eta(t'')\right\rangle_\eta = \frac{\hbar^2\gamma}{4}\Delta t. \tag{2.47}$$

Comparing Eq. (2.46) to the master equations (2.36) shows that the stochastic multiplicative perturbation of the Hamiltonian encoded in Eq. (2.43) leads to the decoherence operator introduced in Eq. (2.39).

2.3.1 Geometric phase for mixed systems

The geometric phase is derived for pure states, and difficulties arise when applying it to mixed systems. The geometric phase is generally not defined for metallic systems, and a mixed system can be regarded as a sum over metallic systems. When considering a single, non-uniformly occupied band it is, however, possible to interpret the integrand of a closed-loop integral for the geometric phase $\gamma_{\mathbf{k}}$ for a wave function $|w_{n\mathbf{k}}(t)\rangle = \sqrt{p_{n\mathbf{k}}}|u_{n\mathbf{k}}(t)\rangle$ in a well-defined manner:

$$\begin{aligned}\gamma_{\mathbf{k}} &= \mathrm{Im}\{\langle w_{n\mathbf{k}}(t)|\nabla_{\mathbf{k}}|w_{n\mathbf{k}}(t)\rangle\} \\ &= \mathrm{Im}\{\langle u_{n\mathbf{k}}(t)|p_{n\mathbf{k}}\nabla_{\mathbf{k}}+\frac{1}{2}(\nabla_{\mathbf{k}}p_{n\mathbf{k}})|u_{n\mathbf{k}}(t)\rangle\} \\ &= p_{n\mathbf{k}}\,\mathrm{Im}\{\langle u_{n\mathbf{k}}(t)|\nabla_{\mathbf{k}}|u_{n\mathbf{k}}(t)\rangle.\end{aligned} \tag{2.48}$$

In this trivial example, the contribution at any $\mathbf{k}$-point is proportional to the population $p_{n\mathbf{k}}$. For non-degenerate uniformly distributed bands, the total response can be obtained

as a sum over all of the bands without any further assumptions:

$$\mathbf{P}(t) = \sum_n p_n \mathbf{P}_n(t) = \frac{q}{2\pi V N_k} \sum_\alpha \sum_{\mathbf{k}} N_\alpha \mathbf{R}_\alpha p_{n\mathbf{k}} \mathrm{Im}\{\log\langle u_{n\mathbf{k}}(t)|\nabla_{\mathbf{k}}|u_{n\mathbf{k}}(t)\rangle\}, \tag{2.49}$$

for normalized functions $|u_{n\mathbf{k}}\rangle$.
For a multiband system, where only a subset of the bands are occupied, a naive application of the covariant derivative fails, as the density matrix is not invertible when it contains unoccupied states. Even a naive application of the covariant derivative for a single-band system fails, as $\langle u_{n\mathbf{k}}|\partial_{\mathbf{k}}|u_{n\mathbf{k}}\rangle$ vanishes by definition, even if the band is not uniformly occupied. Therefore, it is not possible to use the same formalism to evaluate the electric currents for systems of mixed states.

Generalizations to parallel transport for systems that do not conserve $p_{n\mathbf{k}}$ have been put forward by Uhlmann [125] and Sjöquist [114]. The covariant derivative allows for parallel transport of either a single Bloch function or a subspace of degenerate Bloch functions from one $\mathbf{k}$-point to a neighboring one. For a mixed system it is convenient to also introduce a set of orthogonal states $|v_{n\mathbf{k}}\rangle$:

$$\hat{\rho}_{\mathbf{k}}(t) = \sum_n p_{n\mathbf{k}} |v_{n\mathbf{k}}(t)\rangle\langle v_{n\mathbf{k}}(t)| \tag{2.50}$$

The covariant derivatives can, in principle, be calculated separately for each state $|v_{n\mathbf{k}}\rangle$ or subspace of degenerate states $|v_{n\mathbf{k}}\rangle$. For systems with degenerate subspaces the polarization can be evaluated as

$$\mathbf{P}(t) = \frac{q}{2\pi V N_k} \sum_\alpha \sum_{\mathbf{k}} N_\alpha \mathbf{R}_\alpha \sqrt{p_{n\mathbf{k}} p_{n\mathbf{k}+1}} \mathrm{Im}\{\log\det \mathcal{S}_{\mathbf{k},\mathbf{k}+\Delta\mathbf{k}_\alpha}\}, \tag{2.51}$$

where $(\mathcal{S}_{\mathbf{k},\mathbf{k}+\Delta\mathbf{k}_\alpha})_{nm} = \langle v_{n\mathbf{k}}(t)|v_{m\mathbf{k}+\Delta\mathbf{k}_\alpha}(t)\rangle$, and the corresponding electric current is then

$$\mathbf{J}(t) = \frac{q}{2\pi V N_k} \sum_{\mathbf{k}} \sum_\alpha N_\alpha \mathbf{R}_\alpha \mathrm{Tr}\left[\mathcal{S}^{-1}_{\mathbf{k},\mathbf{k}+\Delta\mathbf{k}_\alpha} \frac{\partial}{\partial t} \mathcal{S}_{\mathbf{k},\mathbf{k}+\Delta\mathbf{k}_\alpha}\right]. \tag{2.52}$$

For pure states $\mathcal{S}^{-1}_{\mathbf{k},\mathbf{k}+\Delta\mathbf{k}_\alpha}$ can readily be calculated. In order to evaluate the current for a mixed systems a normalized pseduo-inverse can be constructed by first performing a singular value decomposition $\mathcal{S} = U\Sigma V^\dagger$, and then normalize the singular values with respect to the $\mathbf{k}$-dependent densities:

$$(Y_{\mathbf{k},\mathbf{k}\pm\Delta\mathbf{k}_\alpha})_{ii} = \begin{cases} 1/\sqrt{(\Sigma_{\mathbf{k},\mathbf{k}\pm\Delta\mathbf{k}_\alpha})_{ii}}, & \text{if } (\Sigma_{\mathbf{k},\mathbf{k}\pm\Delta\mathbf{k}_\alpha})_{ii} \neq 0 \\ 0, & \text{otherwise.} \end{cases} \tag{2.53}$$

The normalized pseudo-inverse is then constructed as

$$\bar{\mathcal{S}}^{-1}_{\mathbf{k},\mathbf{k}\pm\Delta\mathbf{k}_\alpha} = U_{\mathbf{k},\mathbf{k}\pm\Delta\mathbf{k}_\alpha} Y_{\mathbf{k},\mathbf{k}\pm\Delta\mathbf{k}_\alpha} V^\dagger_{\mathbf{k},\mathbf{k}\pm\Delta\mathbf{k}_\alpha}. \tag{2.54}$$

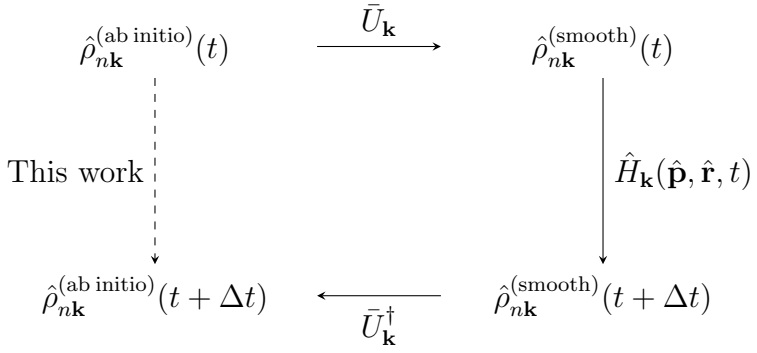

Figure 2.1: The density matrix $\hat{\rho}_{n\mathbf{k}}^{(\text{ab initio})}$ is constructed from a set of wave functions $|u_{n\mathbf{k}}^{(\text{ab initio})}\rangle$ that are not necessarily smooth functions of $\mathbf{k}$. A unitary, but unknown, matrix $\bar{U}_{\mathbf{k}}$ may be applied at wave functions at every $\mathbf{k}$ in order to transform the wave functions to a gauge where the derivative operator that appears in $\hat{H}_{\mathbf{k}}(\hat{\mathbf{p}}, \hat{\mathbf{r}}, t)$ can be evaluated more easily. In this section, a numerical approach is proposed to evaluate the derivative operator in the ab initio gauge for a mixed system.

Given that a meaningful geometric phase can be defined for the system of mixed states, the next step is consider if the geometric phase can be used for constructing a gauge-invariant derivative operator too. To do so, it is necessary to express the states in terms of a density matrix. The master equation in the length gauge reads

$$\begin{aligned} \mathrm{i}\hbar\partial_t \hat{\rho}_{\mathbf{k},\mathrm{LG}} &= [\hat{\rho}_{\mathbf{k},\mathrm{LG}}, \hat{H}_{\mathbf{k}}(t)] + i\gamma[\hat{L}_{\mathbf{k}}, [\hat{\rho}_{\mathbf{k},\mathrm{LG}}, \hat{L}_{\mathbf{k}}]] \\ &= [\hat{\rho}_{\mathbf{k},\mathrm{LG}}, \hat{H}_{0,\mathbf{k}} + \mathrm{i}q\mathbf{E}(t) \cdot \partial_{\mathbf{k}}] + \mathrm{i}\gamma[\hat{H}_{0,\mathbf{k}}, [\hat{\rho}_{\mathrm{LG}}, \hat{H}_{0,\mathbf{k}}]], \end{aligned} \tag{2.55}$$

where $\hat{\mathbf{r}} \to \partial_{\mathbf{k}}$ upon transformation to reciprocal space [18]. Equation (2.55) is similar to that of the semiconductor Bloch equation, and if the $\mathbf{k}$-dependent wave functions are expressed in a gauge that is smooth with respect to $\mathbf{k}$, an ordinary finite difference scheme can be applied to calculate the derivative operator. As illustrated in Figure 2.1, a gauge transformation can, in principle, be applied to transform the wave functions obtained numerically from *ab initio* methods from their original gauge, to a gauge where the wave functions are smooth functions of $\mathbf{k}$. In this gauge, the wave functions can be propagated using a finite difference scheme, and afterwards transformed back to their original gauge. This path is shown with the solid arrows in the Figure. Although the transformation matrices $\bar{U}_{\mathbf{k}}$ are time-independent and only needs to be determined once, they would have to be obtained via a numerical optimization procedure. The alternative approach followed in this section is marked with a dashed line in the Figure, and it consists of evaluating the derivative operator for density matrices in their original gauges.

Based on Eq (2.51), the derivative needed for the master equation Eq. (2.55) is approxi-

mated as

$$[\hat{\rho}_{\mathbf{k},\mathrm{LG}}, \mathrm{i}\partial_{\mathbf{k}}] = \mathrm{i}(\mathcal{S}_{\mathbf{k},\mathbf{k}+\Delta\mathbf{k}}\,\tilde{\rho}_{\mathbf{k}+\Delta\mathbf{k},\mathrm{LG}}\,\mathcal{S}^{\dagger}_{\mathbf{k},\mathbf{k}+\Delta\mathbf{k}} - \mathcal{S}_{\mathbf{k},\mathbf{k}-\Delta\mathbf{k}}\,\tilde{\rho}_{\mathbf{k}-\Delta\mathbf{k},\mathrm{LG}}\,\mathcal{S}^{\dagger}_{\mathbf{k},\mathbf{k}-\Delta\mathbf{k}})\,\tilde{\rho}_{\mathbf{k},\mathrm{LG}} + \mathrm{h.c.} \quad (2.56)$$

where the density matrices have been normalized as $\tilde{\rho}_{\mathbf{k}} = \sum_n \sqrt{p_{n\mathbf{k}}}|v_{n\mathbf{k}}\rangle\langle v_{n\mathbf{k}}|$.
The derivative in Eq. (2.56) yields the same dipole matrix elements

$$d_{ij\mathbf{k}} = \mathcal{S}_{ij\mathbf{k}+\Delta\mathbf{k}}\mathcal{S}^{-1}_{jj\mathbf{k}+\Delta\mathbf{k}} - \mathcal{S}_{ij\mathbf{k}-\Delta\mathbf{k}}\mathcal{S}^{-1}_{i\mathbf{k},j\mathbf{k}-\Delta\mathbf{k}} \quad (2.57)$$

as those that can be obtained from the covariant derivative between an occupied and an unoccupied state. These matrix elements are also consistent with the dipole elements

$$(\mathbf{d}_{\mathbf{k}})_{ij} = (iq\hbar/m_e)(\mathbf{p}_{\mathbf{k}})_{ij}/(E_{j\mathbf{k}} - E_{i\mathbf{k}}) \quad (2.58)$$

between non-degenerate states. One of the advantages of the current implementation is that for fine $\mathbf{k}$-meshes, the terms $\langle v_{n\mathbf{k}+\Delta\mathbf{k}}|v_{m\mathbf{k}}\rangle$ approaches a Kronecker delta up to an irrelevant phase factor in the absence of degenerate states. Whenever decoherence terms are present in the master equation, the occupation probabilities $p_{n\mathbf{k}}$ are not independent of time, and the states $|v_{n\mathbf{k}}\rangle$ have to be calculated from the density matrix numerically at every point in time.

2.3.2 Velocity gauge for mixed states

It is straightforward to calculate the evolution of the density matrix in the velocity gauge by solving the master equation with the Lindblad term:

$$\mathrm{i}\hbar\partial_t\hat{\rho}_{\mathbf{k},\mathrm{VG}} = [\rho_{\mathbf{k},\mathrm{VG}}, \hat{H}_{0,\mathbf{k}} - q\mathbf{A}(t)\cdot\hat{\mathbf{p}}_{\mathbf{k}}] + \mathrm{i}\gamma[H_0 - \frac{q}{m}\mathbf{A}(t)\cdot\hat{\mathbf{p}}_{\mathbf{k}}, [\hat{\rho}_{\mathbf{k},\mathrm{VG}}, \hat{H}_0 - \frac{q}{m}\mathbf{A}(t)\cdot\hat{\mathbf{p}}_{\mathbf{k}}]], \quad (2.59)$$

where the scalar quantity $\frac{q^2}{2m}\mathbf{A}^2(t)$ has been omitted as it commutes with every operator.

2.3.3 Monte Carlo Wave Function method

Modeling decoherence is also achievable by means of the Monte Carlo Wave Function method (MCWF) [82]. The velocity gauge is known for requiring a large basis in order to satisfy the sum rules, which makes the MCWF method ideal for calculations performed in this gauge. The MCWF method replaces the problem of propagating all N_b^2 elements in the density matrix by propagating N_v valence band wave functions each containing N_b elements. For systems where the number of conduction bands is significantly larger than the number of valence bands, a significant reduction in the computational time is expected. The dynamics is determined by deterministically propagating the Bloch functions from $|u_{n\mathbf{k}}(t)\rangle$ to $|u_{n\mathbf{k}}(t+\Delta t)\rangle$ using the non-hermitian Hamiltonian:

$$\tilde{H}_{\mathbf{k}} = \hat{H}_{\mathbf{k}}(t) - \frac{i\hbar}{2}\hat{L}^{\dagger}_{\mathbf{k}}(t)\hat{L}_{\mathbf{k}}(t). \quad (2.60)$$

For a Hermitian matrix, the norm of the wave functions is conserved, but the non-Hermiticity of $\tilde{H}_{\mathbf{k}}$ causes the norm of propagated wave function to diminish. If the wave function is normalized at time t, the propagated wave function $|u_{n\mathbf{k}}(t+\Delta t)\rangle$ is accepted with probability $p = \langle u_{n\mathbf{k}}(t+\Delta t)|u_{n\mathbf{k}}(t+\Delta t)\rangle < 1$. If the solution is not accepted, a jump occurs with probability $\delta p = 1 - p \ll 1$, and the propagated function is instead taken to be $|u_{n\mathbf{k}}(t+\Delta t)\rangle = \hat{L}_{\mathbf{k}}|u_{n\mathbf{k}}(t)\rangle$. The probability of a jump, to lowest order in the discrete time step, depends only on the non-Hermitian part of the Hamiltonian:

$$\begin{aligned}\delta p &= 1 - \langle u_{n\mathbf{k}}(t+\Delta t)|u_{n\mathbf{k}}(t+\Delta t)\rangle &(2.61)\\ &\approx \Delta t\langle u_{n\mathbf{k}}(t)|\hat{L}^{\dagger}_{\mathbf{k}}(t)\hat{L}_{\mathbf{k}}(t)|u_{n\mathbf{k}}(t)\rangle + O(\Delta t^2). &(2.62)\end{aligned}$$

The calculation of the wave function $|u_{n\mathbf{k}}(t+\Delta t)\rangle$ is therefore stochastic, and can be summarized as:

$$|u_{n\mathbf{k}}(t+\Delta t)\rangle = \begin{cases} |\tilde{u}_{n\mathbf{k}}(t+\Delta t)\rangle = f\left(\tilde{H}_{\mathbf{k}}, \Delta t, |u_{n\mathbf{k}}(t)\rangle\right) & \text{if} \quad x < \Delta t\langle u_{n\mathbf{k}}(t)|\hat{L}^{\dagger}_{\mathbf{k}}(t)\hat{L}_{\mathbf{k}}(t)|u_{n\mathbf{k}}(t)\rangle \\ |v_{n\mathbf{k}}(t+\Delta t)\rangle = \hat{L}_{\mathbf{k}}(t)|u_{n\mathbf{k}}(t)\rangle & \text{otherwise} \end{cases} \tag{2.63}$$

where $x \in [0,1]$ is a randomly generated number at every time step, and f represents the numerical scheme used to propagate the wave function deterministically by a time step Δt. The statistical ensemble average at $t_{i+1} = t_i + \Delta t$ is then

$$\begin{aligned}\hat{\rho}^{(i+1)}_{n\mathbf{k}} &= p_{i+1}|\tilde{u}^{(i+1)}_{n\mathbf{k}}\rangle\langle\tilde{u}^{(i+1)}_{n\mathbf{k}}| + (1-p_{i+1})|v^{(i+1)}_{n\mathbf{k}}\rangle\langle v^{(i+1)}_{n\mathbf{k}}| \\ &= p_i|u^{(i)}_{n\mathbf{k}}\rangle\langle u^{(i)}_{n\mathbf{k}}| + p_i\left[\hat{H}^{(i)}_{\mathbf{k}}, |u^{(i)}_{n\mathbf{k}}\rangle\langle u^{(i)}_{n\mathbf{k}}|\right] \\ &- ip_i\Delta t\hat{L}^{(i)\dagger}_{\mathbf{k}}\hat{L}^{(i)}_{\mathbf{k}}|u^{(i)}_{n\mathbf{k}}\rangle\langle u^{(i)}_{n\mathbf{k}}| - ip_i\Delta t|u^{(i)}_{n\mathbf{k}}\rangle\langle u^{(i)}_{n\mathbf{k}}|\hat{L}^{(i)\dagger}_{\mathbf{k}}\hat{L}^{(i)}_{\mathbf{k}} \\ &+ (1-p_i)\hat{L}|u^{(i)}_{n\mathbf{k}}\rangle\langle u^{(i)}_{n\mathbf{k}}|\hat{L}^{(i)\dagger}_{\mathbf{k}} + \mathcal{O}(\Delta t^2) \end{aligned} \tag{2.64}$$

where $(1-p_i) = \Delta t p_i + O(\Delta t^2)$. Even if the error when calculating $|u^{(i+1)}_{n\mathbf{k}}\rangle$ is of order $\mathcal{O}(\Delta t^m)$, where m depends on the numerical scheme, the convergence rate is limited to $\mathcal{O}(\Delta t^2)$ as the MCWF-method is an approximation to the master equation. After each step the wave functions can be normalized for the sake of numerical stability.

While the MCWF-method can also be applied in the length gauge, the benefits of doing so are less obvious. Since the propagation of wave functions depend on wave functions at neighboring $\mathbf{k}$-point, a quantum jump occurring at only one point would cause discontinuities in the excitation densities, which complicates the evaluation of the derivative operator. Alternatively, quantum jumps could occur at all $\mathbf{k}$-points simultaneously, but this would be an inefficient procedure as each calculation is relatively slow, and a large number of independent calculations are required to obtain averaged quantities that are smooth functions of time. Because of the stochastic nature of such a solution, the results are only guaranteed to agree with the deterministic master equation in the limit of infinite runs. The averaged quantities converge at a rate $1/\sqrt{N_{\text{runs}}}$ with respect to the number of

independent simulations N_{run}.

The MCWF method was originally shown to yield the same results as the master equation with first-order propagators [82]. In systems with a strong external force, such as those considered here, it is more practical to propagate wave functions with a higher-order scheme. The probability of a quantum jump is time dependent due the time dependency of the Lindblad operator and state dependency. Consequently, the probability of a quantum jump has to be calculated even if all external fields are absent, which slows down propagation in comparison to deterministic approaches.

2.4 Conclusion

Parts of this chapter were devoted to reviewing well-known approaches for solving the dynamical equations in the length gauge and the velocity gauge. Various approaches can be found in the literature to treat the following problems: (i) interactions proportional to the coordinate operator break spatial translation symmetry of the Hamiltonian, (ii) perturbative methods tend to break electromagnetic gauge invariance, and (iii) mixed states that arise when phenomenological decoherence is included break the structure of the many-body wave functions.
To these ends, a new approach for introducing decoherence operators in the length gauge master equation was proposed. This method is based on numerically decomposing a mixed system in weighted, orthogonal components, and calculating the covariant derivative for each subspace of degenerate components. The method relies on the completeness of the basis, but has the advantage of being compatible with *ab initio* data. This approach has been implemented in a open-source package, which is presented in the next chapter.

Chapter 3

Numerical implementation

Numerical models are essential for predicting material properties and for investigating dynamics that cannot be determined analytically. Several approaches exist to approximate the dynamics governed by the many-particle Schrödinger equation in order to make solutions tractable. These models range from time-dependent generalizations of static tight-binding models to dynamics of electrons in a pseudopotential over *ab initio* approaches starting from density functional theory. Optical responses can then be evaluated from many-body perturbation theory [50, 57, 72], by solving Bethe-Salpeter equation [101, 7]or by applying time-dependent density functional theory [90].

This chapter describes an approach based on solving the time-dependent problem in a basis of Kohn-Sham orbitals that are calculated *ab initio*. This approach has been implemented in the publicly available Python package Ultrafast Light-Matter Interaction Code, `ulmic`.

Ab initio models allow for a systematic approach to determine properties of a large variety of materials. For each material under consideration, the calculation of the ground state and the calculation of the optical properties can be separated into two independent steps. Quantum mechanical simulations are then used to determine the real-time response numerically.

Electron dynamics is modeled in a periodic potential using the independent particle approximation. The wave functions are expanded in periodic Bloch functions, and the electronic system is always taken to initially reside in the ground state, i.e. it consists of an ensemble of valence band electrons, which incoherently populates the valence bands. For illustrative purposes, analytical potentials are also used for one-dimensional and two-dimensional periodic lattices. While the latter approach does not rely on density functional theory, it can be considered equivalent by considering it as the Kohn-Sham potential, and self-consistently determine the external potential that would give rise this particular Kohn-Sham potential.

The first part of the chapter introduces the density functional theory packages that are used in this work. The desired data is extracted from the various codes, and the format of the data is aligned. Afterwards, the implementation of the `ulmic`-code is described in detail. Lastly, one-dimensional examples are considered using analytical potentials to

demonstrate the robustness of the formalism.

3.1 Integration with density functional theory packages

In order to develop a robust and reliable tool for determining opto-electric properties of a wide range of materials, it is advantageous to leverage the efforts that have been devoted to develop density functional theory codes over the past decades. As many packages exist, it is desirable to develop a flexible interface, such that data from a number of the popular codes is easily extracted and can be used as input for `ulmic`.

The wave functions contain all relevant information related to the ground state, so `ulmic` can only be independent of the choice of exchange-correlation potential if the ground state data is sufficient. When solving the dynamical equations, this translates into assuming that the time-dependent density does not change significantly such that the exchange-correlation term is practically time-independent. While density functional theory only allows for determining the ground state, a set of unoccupied excited states can be determined, and these provide a convenient basis when solving the time-dependent problem. The approach pursued here can be considered an approximation to time-dependent density functional theory. While TDDFT is capable of including electron-electron interactions and may include time-dependent exchange-correlation terms, it is unclear to what extent approaches based on TDDFT correctly capture the dynamics. Time-dependent exchange-correlation potentials are especially complicated, and calculations based on time-dependent exchange correlation potentials beyond ALDA are rare. Recent calculations with ALDA show that neglecting the time-dependency of the xc-energy has little impact of high-harmonic spectra.

The external density functional theory codes used in this work are Wien2k, GPAW, QUANTUM ESPRESSO and Abinit. Data from the all-electron code Wien2k [14], and pseudopotential-based codes, such as GPAW [32], Abinit [45] and QUANTUM ESPRESSO [43] have been extracted and tested with `ulmic`. Energies and matrix elements can be obtained readily from GPAW and from Wien2k by using the `optic` module [2]. Data from Abinit and QUANTUM ESPRESSO can be extracted with the help of the code Yambo [79]. The benefit of interfacing the code with multiple existing DFT codes is to make it more accessible to a larger group of researchers and to verify the reproducibility of the various DFT codes. Reproducibility among different DFT codes is of interest, and at least for band gaps, modern codes tend to produce results that are similar up to sufficiently high accuracy [71].

Workflow

Once the self-consistent problem has been solved and the ground state density has been determined, the wave functions for a large number of excited state are calculated. The wave functions are calculated for an equidistant grid of $\mathbf{k}$ points, typically a Monkhorst-Pack grid. For each wave function the energy $E_{n\mathbf{k}} = \langle\psi_{n\mathbf{k}}|\hat{H}|\psi_{n\mathbf{k}}\rangle$ is determined, and the matrix

elements of the momentum operator $\mathbf{p}_{nm\mathbf{k}} = \langle\psi_{n\mathbf{k}}|\hat{\mathbf{p}}|\psi_{m\mathbf{k}}\rangle$ are calculated for pairs of wave functions at each $\mathbf{k}$ point. Overlap integrals $S_{nm\mathbf{k},\mathbf{k}+\Delta\mathbf{k}_\alpha} = \langle\psi_{n\mathbf{k}}|\psi_{m\mathbf{k}+\Delta\mathbf{k}_\alpha}\rangle$ are calculated between wave functions at neighboring $\mathbf{k}$ points. When calculating the overlap integrals, it is important that the gauges for the wave functions have the same periodicity as the Brillouin zone. I.e. for wave functions at $\mathbf{k}$ and $\mathbf{k}+\Delta\mathbf{k}_\alpha$, where both points lie within the first Brillouin zone the overlap is straightforward to calculate:

$$S_{nm,\mathbf{k},\mathbf{k}+\Delta\mathbf{k}_\alpha} = \langle\psi_{n\mathbf{k}}|e^{-i\Delta\mathbf{k}_\alpha\cdot\mathbf{r}}|\psi_{m\mathbf{k}+\Delta\mathbf{k}_\alpha}\rangle. \tag{3.1}$$

Along the edge of the Brillouin zone, the wave functions at the points lying outside the first Brillouin zone are calculated from the translation of a points in the interior region:

$$S_{nm,\mathbf{k},\mathbf{k}+\Delta\mathbf{k}_\alpha} = \langle\psi_{n\mathbf{k}}|e^{-i\Delta\mathbf{k}_\alpha\cdot\mathbf{r}}|\psi_{n\mathbf{k}+\Delta\mathbf{k}_\alpha-\mathbf{G}_\alpha}e^{i\mathbf{G}_\alpha\cdot\mathbf{R}}\rangle. \tag{3.2}$$

Practically all maintained DFT codes are interfaced with Wannier90, which is a popular program for constructing Wannier functions [83]. The codes are therefore capable of producing matrices containing the overlap integrals between neighboring wave functions.

At this stage, all of the necessary information for calculating the dynamics in the independent particle approximation can be extracted. I.e. wave functions do not have to be loaded into `ulmic`, and they can henceforth be discarded.
For further developments, it is possible to calculate the self-energy in order to correct the band gap predicted by e.g. LDA-based calculations. Several options exist to calculate the self-energy. GPAW allows for calculating G_0W_0 and GW_0 with self-consistent energies. Abinit is capable of the calculating GW-corrected wave functions self-consistently. For Wien2k, the codes `exciting`, `GAP` and `GAP2` can be used. For QUANTUM ESPRESSO, the codes Yambo [79] and BerkeleyGW [28] can be used.

3.2 ULMIC

The interface to the density functional theory data, as well as an implementation of the equations of motion have been written to the package `ulmic`. The code is designed for maximum portability, and is available on the Python Package Index repository. It includes just-in-time compilation (JIT) to increase performance and message passing interface (MPI) to account for scalability.

As mentioned earlier, the purpose of `ulmic` is to take advantage of the existing codes and frameworks that are concerned with calculating material properties *ab initio*, and use DFT to calculate real-time optical responses for short, intense laser pulses.
As an example, the code can be used to calculate the dynamics of electrons in a GaAs crystal under the exposure of a infrared pulse in the velocity gauge as:

```
#!/usr/env/python
from ulmic import Medium, Pulses UltrafastLightMatterInteraction

medium = Medium('GaAs.hdf5')
pulse = Pulses(['default_IR'])
time = np.linspace(-200,200,100)
ulmi = UltrafastLightMatterInteraction(medium,pulse,time)
result = ulmi.run_stepwise('vg','tdse')
```

The code has also been set up for visualizing equilibrium properties of the density functional theory data stored in the hdf5 files that can be generated from the data from the external codes:

```
#!/usr/env/python
from ulmic import Medium

medium = Medium('GaAs.hdf5')
medium.show.band_structure()
medium.show.susceptibility()
medium.show.berry_curvature_path()
medium.show.berry_curvature_plane()
```

3.2.1 Overview

The `ulmic` code is composed of a set of independent modules. The main modules are the following ones:

- **Medium**: All relevant data obtained from density functional theory calculations are stored in standardized hdf5-format[34]. The Medium module is responsible for reading the hdf5-file and storing data derived from the raw input data. The module also contains methods for manipulating the data, methods for calculating equilibrium properties such as the optical susceptibilities, methods for checking the completeness of the basis, such as convergence and sum rules, and methods for visualization of e.g. band structures.

- **Pulses**: This module contains the methods necessary for evaluating the electric fields. Fields can either be defined in terms of analytical functions or read from a file. The method is also designed to manipulate experimentally measured fields read from a file to ensure their temporal and spectral properties are well-behaved.

- **UltrafastLightMatterInteraction** (ULMI): Provide numerical implementations for solving the equations of motion for the wave functions and for density matrices. The numerical results are contained in an object that contains method for further post-processing.

- **Analyse**: Used for analyzing results from a calculation. This generally involves visualization of the time- and frequency response, as well as verifying the self-consistency of the results by comparing observables that can calculated in multiple gauge-dependent ways.

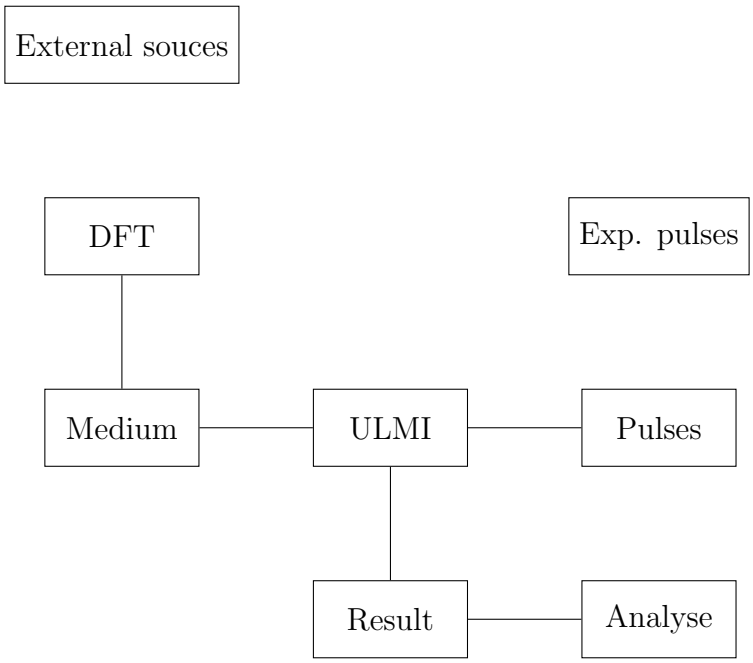

Figure 3.1: Schematic overview of the modules that are part of ultra-fast light-matter interaction code, `ulmic`. External sources refer to online repositories such as the Novel Materials Discovery Laboratory (NOMAD) [87] from which references to converged DFT solutions can be obtained. DFT data is processed by the Medium module, and experimentally measured pulses by the Pulses module. Both modules are used for the core UltrafastLightMatterInteraction module. Numerical solutions are afterwards processed by the Result and Analyse modules.

3.2.2 Implementation and scaling

The main task of `ulmic` is to solve the equations of motion, namely the time-dependent Schrödinger equation (TDSE) and the master equation. In the Schrödinger picture the TDSE has the generic form

$$i\hbar\frac{d}{dt}|u_{n\mathbf{k}}\rangle = (\hat{H}_{0,\mathbf{k}} + \hat{H}_{\mathrm{int},\mathbf{k}}(t))|u_{n\mathbf{k}}\rangle. \tag{3.3}$$

The electrons evolve with a stationary phase which depends on their particular energy. As the span of energies can be large, the phase of some of the electronic states oscillates rapidly at a frequency of up to $\omega_{\max} = (\max_{n,\mathbf{k}}\{E_{n\mathbf{k}}\} - \min_{n,\mathbf{k}}\{E_{n\mathbf{k}}\})/\hbar$. The oscillation period sets an upper limit on the allowed step size $\Delta t \sim 1/\omega_{\max}$. To reduce the influence of the rapidly evolving wave functions on the numerical stability it is beneficial to transform the equation to the interaction picture:

$$i\hbar\frac{d}{dt}|\tilde{u}_{n\mathbf{k}}\rangle = e^{i\hat{H}_{0,\mathbf{k}}t}\hat{H}_{\mathrm{int},\mathbf{k}}(t)e^{-i\hat{H}_{0,\mathbf{k}}t}|\tilde{u}_{n\mathbf{k}}\rangle. \tag{3.4}$$

In the interaction picture, the rapidly evolving phases only appear in the interaction Hamiltonian. This allows for arbitrarily large time steps whenever the field is not present, i.e. at times when $\hat{H}_{\mathrm{int},\mathbf{k}} = 0$. The wave functions are expanded in the basis of Kohn-Sham orbitals

$$|\tilde{u}_{n\mathbf{k}}(t)\rangle = \sum_n c_{mn\mathbf{k}}(t)|\tilde{u}^0_{m\mathbf{k}}\rangle. \tag{3.5}$$

Velocity gauge Hamiltonian

In the velocity gauge $\hat{H}_{\mathrm{int},\mathbf{k}} = \frac{e}{m}\mathbf{A}(t)\cdot\hat{\mathbf{p}}_{\mathbf{k}} + \frac{e^2}{2m}A^2(t)$, and the equations of motion reduce to a set of ordinary differential equations for the expansion coefficients:

$$i\hbar\frac{d}{dt}c_{mn\mathbf{k}}(t) = \sum_l h_{nl}(t)c_l(t). \tag{3.6}$$

where $h_{nl}(t) = [e^{i\hat{H}_{0,\mathbf{k}}t}\hat{H}_{\mathrm{int},\mathbf{k}}(t)e^{-i\hat{H}_{0,\mathbf{k}}t}]_{nl}$. For fully occupied valence bands, the initial conditions are $|c_{mn\mathbf{k}}(t_0)| = \delta_{nm}$ for $n < N_V$.

The ordinary differential equations can be solved using a Runge-Kutta scheme, which is an explicit, non-unitary scheme and is accurate to fourth order, $\mathcal{O}(\Delta t^4)$. If unitarity is important, an exponential scheme can be employed to arbitrarily high order:

$$\hat{\mathcal{H}} = \hat{H}(t) - \frac{1}{2!}dt\hat{H}' + \frac{1}{3!}dt^2\hat{H}'' + \frac{i}{12}dt^2[\hat{H},\hat{H}'] + ... \tag{3.7}$$

Solving the TDSE using an explicit scheme yields a scaling of $\mathcal{O}(N_k N_v N_b^2)$. It is dominated by matrix-vector multiplication. For master equation approaches, the scaling is $\mathcal{O}(N_k N_b^3)$ as it is dominated by matrix-matrix-multiplication.

Semiconductor Bloch equations

In the length gauge $H_{\text{int},\mathbf{k}} = -e\mathbf{F}(t) \cdot \mathbf{r}$, and the coordinate operator can be written in terms of a derivative operator with respect to the crystal momentum. If the derivative operator can be expressed as a finite difference, the equations of motion become partial differential equations that are linear in the expansion coefficients $c_{mn\mathbf{k}}(t)$. This is the case with the semiconductor Bloch equations introduced in Eq. 2.4, and a numerical scheme like the Crank-Nicholson scheme is well suited for solving the partial differential equations.

Implicit methods, such as the Crank-Nicholson, can be unitary, and designed for partial differential equations, but require solving a matrix equation at every time step. The Crank-Nicholson method is best suited for one-dimensional systems where the wave functions are smooth functions of the crystal momentum. A drawback of the Crank-Nicholson scheme is that each time step is only accurate to second order in time, i.e. $O(\Delta t^2)$. As the dynamics is driven by a strong electric field, more accurate schemes are desirable.

Covariant derivative-based Hamiltonian

When using the covariant gauge calculated from the polarization in Eq. (2.22) the equations of motion are no longer linear in the expansion coefficients, and a numerical scheme that can handle non-linearities is required. Such a scheme could be a Runge-Kutta scheme, even if such schemes are generally not suitable for solving partial differential equations. If decoherence is present, the calculations involve singular value decompositions, which also scale as $\mathcal{O}(N_k N_b^3)$ [118].

The covariant derivative is used to calculate the geometric phase, and the accuracy of the geometric phase depends on the discretization in $\mathbf{k}$ space. The phase can either be evaluated as a line integral in space by multiplying the matrices in Eq. (2.18) before calculating the determinant, or by evaluating the determinant at each $\mathbf{k}$ point using only the information of the nearest neighbor. The latter approach is more suited for parallel implementations, and is therefore employed here. For the calculation of the $\mathbf{k}$-dependent phase-contributions to the geometric phase, only the nearest-neighbor overlaps are required:

$$\phi_{k_n}^{(2)} = \langle u_{k_n} | u_{k_{n+1}} \rangle - \langle u_{k_n} | u_{k_{n-1}} \rangle + \mathcal{O}(\Delta k^2). \tag{3.8}$$

The phases can be calculated to higher order as well, but this also requires information from the second-nearest neighbors [88]:

$$\phi_{k_n}^{(4)} = \left[\frac{4}{3}\langle u_{k_n} | u_{k_{n+1}} \rangle - \frac{1}{6}\langle u_{k_n} | u_{k_{n+2}} \rangle\right] - \left[\frac{4}{3}\langle u_{k_n} | u_{k_{n-1}} \rangle - \frac{1}{6}\langle u_{k_n} | u_{k_{n-2}} \rangle\right] + \mathcal{O}(\Delta k^4) \tag{3.9}$$

To be compatible with standard DFT packages only the nearest-neighbor overlaps are required as input data for `ulmic`. The second-nearest neighbor overlaps can be constructed directly from successive calculations of nearest-neighbor overlaps, if the basis at every $\mathbf{k}$ point is sufficiently complete. If the basis is not sufficiently complete, inaccurate values of

the second-neighbor overlaps can cause the high-order finite derivatives to be less accurate than the first-order scheme.

Calculating the current and polarization from the geometric phase has one obvious drawback compared to determining them from the velocity operator. The intraband contribution is no longer guaranteed to be constant when implemented on a finite **k** mesh. In contrary, if ΔE is the typical energy difference between neighboring **k** points, the intraband current will oscillate with periods of $(\hbar/\Delta E)$, which necessitates the use of a fine mesh. Similarly, the polarization that can be evaluated from the geometric phase is necessarily bounded from above. I.e. a constant, finite residual current causes the polarization to increase linearly with time, but constant currents cannot be supported indefinitely for a finite set of **k** points when the contribution from each point oscillates with time.

3.2.3 Convergence

One way of determining the accuracy of the obtained solutions is to check for the self-consistency of the input parameters. The diagonal momentum matrix elements can be calculated from the spatial derivative of the wave functions or from the derivative of the energy bands with respect to the crystal momentum:

$$\mathbf{p}_{nn\mathbf{k}} = \langle\psi_{n\mathbf{k}}| - i\hbar\nabla|\psi_{n\mathbf{k}}\rangle = \langle\psi_{n\mathbf{k}}|[\hat{H}, \hat{\mathbf{r}}]|\psi_{n\mathbf{k}}\rangle = \nabla_{\mathbf{k}} E_n(\mathbf{k}). \tag{3.10}$$

This can be used to check that the a calculation of the diagonal elements of the momentum operator in real space at a single **k**-point is consistent with the derivative of the energies in reciprocal space.

Likewise, the effective mass can be calculated at every **k**-point in order to verify the Thomas-Reiche-Kuhn sum rule. The effective mass is calculated as the second derivative of the energy, or equivalently as the first derivatives of the diagonal elements of the momentum matrix:

$$\frac{\partial^2}{\partial k_i \partial k_j} E_n(\mathbf{k}) = \frac{\partial}{\partial k_i} p_{j,nn} = \frac{\partial}{\partial k_j} p_{i,nn} = \frac{1}{m_{ij}} \tag{3.11}$$

The Thomas-Reiche-Kuhn sum rule introduced in Eq. (1.27) is said to be satisfied if:

$$f_{\mathrm{TRK}}(E, p, \mathbf{k}, \alpha, \beta) = \left| \frac{2}{m} \sum_l \frac{p_{in\mathbf{k},\alpha} p^*_{jl\mathbf{k},\beta}}{E_{n\mathbf{k}} - E_{l\mathbf{k}}} - \delta_{ij} + m \frac{\partial^2 E_{n\mathbf{k}}}{\partial k_\alpha \partial k_\beta} \right| < \varepsilon_{\mathrm{TRK}} \tag{3.12}$$

for a given tolerance $\varepsilon_{\mathrm{TRK}}$. If the sum is truncated at a fixed band index N, the rule is necessary violated, but N can be chosen sufficiently large that the sum rule is satisfied for the lowest band. Bands with an index close to N necessarily violates the sum rule. For $\alpha = \beta$ and $n = N$, the sum in Eq. 3.12 consists purely of negative contributions. Therefore, effective masses predicted from the momentum matrix elements deviate significantly from the actual effective masses.
The Thomas-Reiche-Kuhn sum depends on the fundamental operator identity:

$$\hat{\mathbf{r}}\hat{\mathbf{p}} - \hat{\mathbf{p}}\hat{\mathbf{r}} = i\hbar, \tag{3.13}$$

which may also be evaluated directly for the time-dependent wave functions. Once the basis is truncated the identity is necessarily violated. The Thomas-Reiche-Kuhn sum rule is ideal for evaluating the identity for the individual bands, whereas Eq. (3.13) can be evaluated at any point in time during the excitation process. The identity yields an effective number of valence electrons, which is also often used as a measure of convergence in density functional theory calculations. The benefit of introducing the concept of effective number of electrons in electrodynamical calculations is that it may be used to make results obtained with only a small number of bands more reliable.

If a high degree of self-consistency has been reached, it is possible to determine energies and momentum matrix elements of the wave functions with a crystal momentum of $\mathbf{k} + \Delta\mathbf{k}$ using only the values for wave functions with at crystal momentum of $\mathbf{k}$. This extrapolation procedure introduced in Eq. (1.30) serves as an alternative to e.g. Wannier interpolation:

$$\hat{H}'_{\mathbf{k}}(\Delta\mathbf{k}) = \hat{H}_{\mathbf{k}} + \frac{1}{2}\Delta\mathbf{k}^2 + \Delta\mathbf{k} \cdot \hat{\mathbf{p}}_{\mathbf{k}}. \tag{3.14}$$

The extrapolation of band energies does not only allow for obtaining a finer $\mathbf{k}$ mesh. It also allows for the possibility to check whether velocity-gauge calculations can be expected to be converge with respect to the number of bands for a given field strength. The deviation between the energies extrapolated from a point $\mathbf{k}_0$ and the actual values determined from density functional theory at $\mathbf{k}$ can be quantified as

$$\delta_{\text{extra},m\mathbf{k}} = \sum_{\Delta\mathbf{k}' \in \text{nNN}} \left| \tilde{E}_{m\mathbf{k}}(\Delta\mathbf{k}) - E_{m\mathbf{k}+\Delta\mathbf{k}} \right| \tag{3.15}$$

where $\tilde{E}_{m\mathbf{k}}(\Delta\mathbf{k})$ is the mth eigenvalue of the displaced Hamiltonian $\hat{H}'_{\mathbf{k}}(\Delta\mathbf{k})$, nNN refers to the n-nearest neighbors and $E_{m\mathbf{k}+\Delta\mathbf{k}}$ are the actual eigenvalues of the Hamiltonian $\hat{H}_{\mathbf{k}+\Delta\mathbf{k}}$.

Local potentials

While the code is designed for *ab initio* input data, it is very instructive to calculate responses from electrons in analytical potentials. The cell-periodic part of the wave function can be calculated as eigenfunctions to the field-free Hamiltonian:

$$\left[\frac{(\hat{\mathbf{p}}+\hbar\mathbf{k})^2}{2m}+V(\mathbf{r})-E_{n\mathbf{k}}\right]u_{n\mathbf{k}}(\mathbf{r})=0. \tag{3.16}$$

For a numerical implementation, it is convenient to expand the cell-periodic Bloch functions in a set of basis functions. A convenient choice is plane waves, and the number of basis functions is related to the maximum value of $\mathbf{G}$ to be included in the expansion, which determines the cutoff-energy of the expansion:

$$u_{j\mathbf{k}}(\mathbf{r})=\sum_{\mathbf{G}}c_{j,\mathbf{G}\mathbf{k}}e^{i2\pi\mathbf{r}\cdot\mathbf{G}}=\sum_{nml}c_{j,nml\mathbf{k}}e^{i2\pi\mathbf{r}\cdot(n\mathbf{G}_1+m\mathbf{G}_2+l\mathbf{G}_3)}, \tag{3.17}$$

where $\mathbf{G}=n\mathbf{G}_1+m\mathbf{G}_2+l\mathbf{G}_3$. For a local potential $V(\mathbf{r})$, the solution can be found via diagonalization of the Hamiltonian:

$$\frac{(2\pi\mathbf{G}+\mathbf{k})^2}{2m}c_{j,nml\mathbf{k}}+\sum_{\mathbf{G}'}\int_{\mathcal{V}}V(\mathbf{r})e^{i2\pi\mathbf{r}\cdot(\mathbf{G}'-\mathbf{G})}\,d\mathbf{r}c_{j,n'm'l'\mathbf{k}}=E_{n\mathbf{k}}c_{j,nml\mathbf{k}} \tag{3.18}$$

$$\left[\frac{(2\pi(n\mathbf{G}_1+m\mathbf{G}_2+l\mathbf{G}_3)+\mathbf{k})^2}{2m}c_{j,nml\mathbf{k}}\right. \tag{3.19}$$

$$\left.+\sum_{n'm'l'}\int_{\mathcal{V}}V(\mathbf{r})e^{i2\pi\mathbf{r}\cdot((n'-n)\mathbf{G}_1+(m'-m)\mathbf{G}_2+(l'-l)\mathbf{G}_3)}\,d\mathbf{r}c_{j,n'm'l'\mathbf{k}}\right]=E_{n\mathbf{k}}c_{j,nml\mathbf{k}} \tag{3.20}$$

A simple approach to measure degree of convergence ϵ of the wave functions with respect to the cut-off energy and the resolution of the spatial grid, is to apply the real space Hamiltonian $\hat{H}_{\mathbf{k}}(\mathbf{r})$ to the wave functions, i.e. $\epsilon=|u_{n\mathbf{k}}(\mathbf{r})-H_{\mathbf{k}}(\mathbf{r})u_{n\mathbf{k}}(\mathbf{r})/E_{n\mathbf{k}}|$ for $E_{n\mathbf{k}}\neq 0$.

3.3 Convergence test in 1D

To verify that solving the equations of motion in the length and velocity gauge yield the same results, the dynamics for a one-dimension system is calculated. The optical current induced by a few-cycle pulse is determined using the momentum operator and the geometric phase formalism. For the sake of simplicity, the one-dimensional potential is defined as

$$V_{1\mathrm{D}}(x) = -\sum_{n=-\infty}^{\infty} V_0 \mathrm{sech}\left(\frac{x - n a_{\mathrm{lat}}}{a_0}\right), \tag{3.21}$$

and the stationary solutions are calculated through an exact diagonalization of the Bloch functions expanded in a basis of plane waves. The real space contains 800 points per unit cell, and a basis of 41 plane waves is used. For $V_0 = 1.0$, $a_{\mathrm{lat}} = 5.0$ and $a_0 = 0.2$ the band gap between the two lowest bands is 7.3 eV. The electrons are taken to be spinless, and the lowest band is taken to be filled, while all other bands are empty. For $\gamma = 0.1$ the dephasing time at the position of the minimum band gap is 6.7 fs according to Eq. (2.39). The electric field is derived from a Gaussian function

$$E(t) = \frac{E_{\max}}{\omega}\frac{d}{dt}\left(e^{-2\ln 2\frac{t^2}{t^2_{\mathrm{FWHM}}}}\sin(\omega t)\right) \tag{3.22}$$

which ensures that the definite integral over the electric field over all times vanishes. The electric field parameters are taken to be $\hbar\omega = 1.6$ eV and $t_{\mathrm{FWHM}} = 2$ fs, which causes the spectrum of the pulse to be very broad as $\omega t_{\mathrm{FWHM}} \sim \pi$. Field strengths up to $E_{\max} = 1.5$ V/Å are used, as this is sufficiently strong to accelerate the electron across half the Brillouin zone, i.e. $qE_{\max}a_{\mathrm{lat}}/\omega\hbar \sim \pi$.

Hartree atomic units are used for the rest of the section unless the unit is specifically stated. For this convergence study, non-ionizing high harmonic generation is considered, as this is a phenomena that has been studied well in the literature [119], [56],[44].

The optically induced current is shown in Figure 3.2 (a). High order harmonics are generated as excitations interact with the electric field, while the current oscillates and decay to a constant value after the external field vanishes. The current is, however, unsuited for obtaining a power spectrum, as it generally has a finite value after the pulse. In contrast, the acceleration decays to zero in the presence of dephasing, which makes it a better choice for obtaining a smooth spectrum. The power spectrum of the corresponding acceleration is show in Figure 3.2 (b) for different field strengths. A clear transition can be seen from the regime of perturbative harmonics at a field strength of 0.1 V/Å, to plateaus characteristic of non-perturbative harmonic generation at 0.5 V/Å. Finally, a fully developed non-perturbative response that forms a continuous spectrum of harmonics is observed at field strengths 1.5 V/Å.

As has been pointed out in previous papers [147], the appearance of additional plateaus can be explained by the presence of multiple conduction bands. The plateau that appears in the calculation for $E_{\max} = 0.5$ V/Å in the region 15 eV - 25 eV disappears if the calculation would be limited to only include a single conduction band.

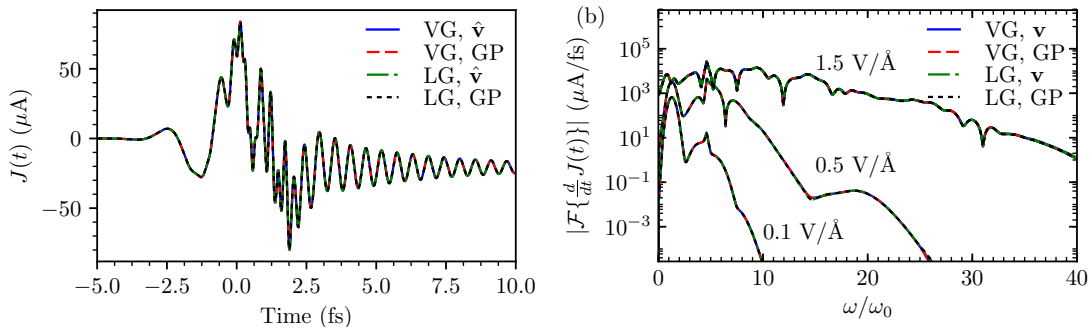

Figure 3.2: (a) Time-resolved induced current for the ground state subjected to a pulse with a peak electric field strength of 1.5 V/Å. Power spectrum of the acceleration for pulses of varying peak field strength. In both plots an excellent agreements between the length gauge (blue, red) and velocity gauge (green, black) and between the current obtained via the velocity operator (blue, green) and the geometric phase (red, black) are observed.

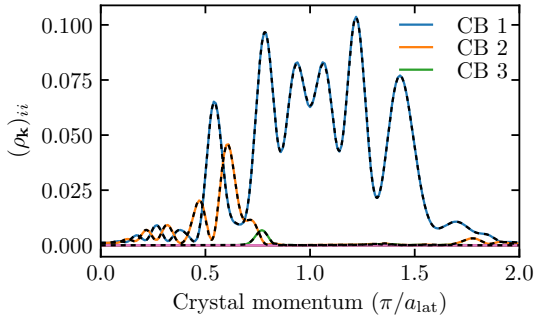

Figure 3.3: Distributions of electrons in the conduction bands (CB) after excitation by a pulse with $E_{\max} = 1.5$V/Å according to a velocity gauge calculation (colored, solid lines) and length gauge calculation (black, dashed lines).

The distributions of electrons at the end of the pulse is shown in Figure 3.3. The excellent agreement of the results obtained in the two gauges, despite the presence of dephasing, confirms that the proposed approaches do not break gauge invariance.

A comparison of results obtained with the Monte Carlo Wave Function method to those obtained using the deterministic methods is shown in Figure 3.4. For the chosen field strength of 1.5 V/Å, the spectrum in Figure 3.4(b) converges fast for photon energies up to $\approx 20\omega_0$. Because of the high field strength, the peak at the fundamental frequency splits into two separate peaks [85]. As quantum jumps lead to discontinuities in either the observables or their derivatives, their frequency spectra contain noisy components. Consequently, it is necessary to take an average over many runs. The results shown here is an average of the optical response over 200 runs, and is reasonably converged when compared to the response from the deterministic master equation approach. As expected, the results converge as $\sqrt{N_{\text{run}}}$, and this behavior is observed in Figure 3.4(c). The method is therefore less suited for analyzing low-magnitude high-frequency components. As only 8

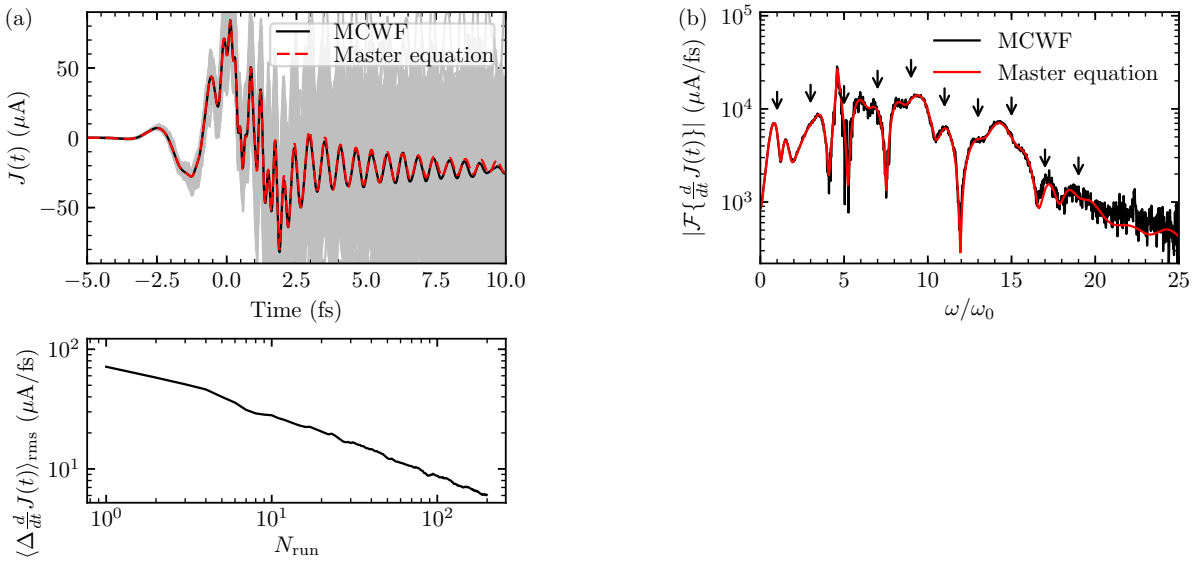

Figure 3.4: (a) Time-resolved induced current for the ground state subjected to a pulse with a peak electric field strength of 1.5 V/Å. Power spectrum of the acceleration for pulses of varying peak field strength. In both plots an excellent agreements between the length gauge (blue, red) and velocity gauge (green, black) and between the current obtained via the velocity operator (blue, green) and the geometric phase (red, black) are observed.

bands were necessary for convergence in this one-dimensional example, the MCWF method did not outperform the master equation approach in terms of computation time.

Uniform decoherence rates

To demonstrate that the use of uniform dephasing rates in the velocity gauge corresponds to a field-dependent dephasing mechanism that is difficult to interpret, the results presented in Figure 3.2 are now calculated with constant off-diagonal decay rates for the density matrix. All of the states are chosen dephase at a rate

$$\mathcal{L}_{\mathrm{LG}}(\rho)_{ij} = \mathcal{L}_{\mathrm{VG}}(\rho)_{ij} = \gamma_0 \rho_{ij}(1 - \delta_{ij}) \tag{3.23}$$

where δ_{ij} is the Kronecker symbol. As the dephasing terms are not gauge-invariant, the two master equations do not correspond to the same physical system, so the dielectric response is expected to be visibly different. Although terms that break gauge invariance are of limited interest from a physical point of view, the results may still be of relevance as such dephasing terms are frequently encountered in the literature.

The dephasing rate is taken to be $\gamma_0 = 2.1$ fs^{-1}, which corresponds to the energy-dependent dephasing rate from the previous section evaluated at the average energy difference between the valence band and lowest conduction band. The outcomes of solving the master equation with these new terms are shown in Figure 3.5. The time-dependent electric currents are visibly different. In the spectral domain, the two new energy-independent

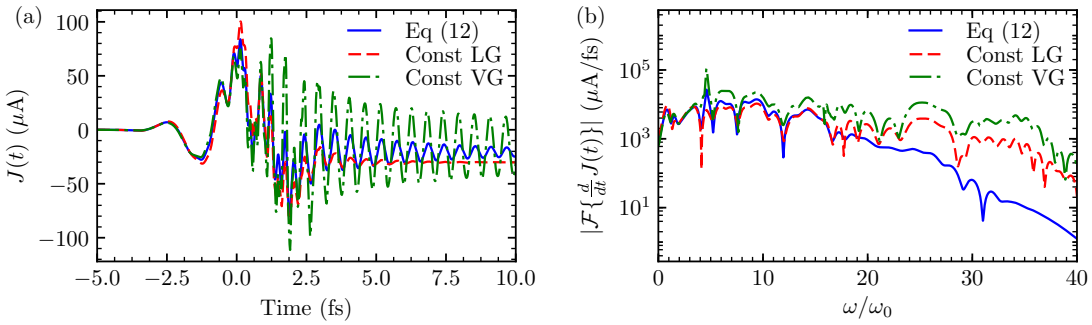

Figure 3.5: (a) Optical current evaluated with the dephasing rates given in Eq. (2.40) (blue), and evaluated using constant dephasing rates in length gauge (red) and velocity gauge (green). (b) Spectral components of the corresponding accelerations.

dephasing models produce spectral intensities that significantly exceed those presented in the Figure 3.2, especially at the high frequencies ($\omega > 25\omega_0$). The fact that the spectral intensities are higher is not surprising, as those oscillations are damped much faster when using energy-dependent dephasing rates. Interestingly, the amplitude of the current is significantly larger when using constant decay rates for to model dephasing in the velocity gauge. Comparing the spectrograms shows that the length-gauge result and the velocity-gauge result are qualitatively similar at high frequencies, but that the velocity-gauge result overestimates the peak at the fundamental band gap by almost two order of magnitudes in comparison to the length-gauge result.

3.4 Adiabatic corrections

In order to improve run-time performance of calculations in the velocity gauge, it is relevant to examine if the requirement of using a large basis set can be relaxed under certain, non-trivial conditions. The velocity gauge usually demands a basis with many more states than length-gauge or Houston-basis simulations [148]. The purpose of this section is to derive analytical corrections to the polarization response evaluated with a relatively small number of bands, and to test range of validity of this approach. It is shown that it works well for strong fields for one-dimensional potentials [150].

One of the advantages of the velocity gauge, in contrast to the length gauge, is that an external field does not break the spatial periodicity. Since the periodicity of the lattice potential is preserved, the Bloch theorem applies to both $\hat{H}_0$ and $\hat{H}(t)$, where

$$\hat{H}(t) = \hat{H}_0 + \hat{H}_{\text{int}} = \hat{H}_0 + \frac{e}{m}\mathbf{A}(t)\cdot\hat{\mathbf{p}} + \frac{e^2}{2m}A^2(t). \tag{3.24}$$

On the other hand, the use of a truncated basis eventually leads to numerical artifacts if a constant field is applied. This fact can be made clear by representing the constant, homogeneous electric field in the velocity gauge $\mathbf{A}(t) = -\mathbf{F}_0 t$ and calculate the displaced Hamiltonian

$$e^{i\frac{q}{\hbar}\mathbf{F}_0\cdot\hat{\mathbf{r}}t}\hat{H}(\hat{\mathbf{r}},\hat{\mathbf{p}})e^{-i\frac{q}{\hbar}\mathbf{F}_0\cdot\hat{\mathbf{r}}t} = H(\hat{\mathbf{r}},\hat{\mathbf{p}}-\mathbf{F}_0 t) = H(\hat{\mathbf{r}},\hat{\mathbf{p}}) + \frac{1}{2}(\mathbf{F}_0 t)^2 - \mathbf{F}_0 t\cdot\hat{\mathbf{p}}. \tag{3.25}$$

The eigenvalues of the field-dependent Hamiltonian diverge for $t\to\infty$ if $\hat{H}$ and $\hat{\mathbf{p}}$ are finite-dimensional matrices. For an infinite-dimensional matrices with matrix elements calculated to infinitely high precision the eigenvalues would vary periodically in time according to the equilibrium band structure.

The adiabatic corrections introduced in this section are also relevant regarding the issue of diverging zero-frequency responses for e.g. the dielectric functions. Length gauge calculations can produce reliable results with a relatively small number of bands because information of band structure at points far away from the initial crystal momentum $\mathbf{k}_0$ is accessed via the derivative operator, whereas velocity gauge calculations require a large number of bands because all information of band structures at every $\mathbf{k}$-point is encoded in the matrix elements at a single point. To achieve numerical convergence a much larger basis is therefore expected to be required: $\mathcal{N}_{\text{VG}} \gg \mathcal{N}_{\text{LG}}$. If a large number of bands are included, and the spectrum of transition energies vastly exceeds the frequency of the external fields, a significant fraction of the dynamics may be expected to be adiabatic. In such cases, the dynamics is simple to calculate, and a simple approximation to the untruncated basis may be found.

As a first step, the corrections are assumed to be a function of the instantaneous vector potential only. The approximation is expected to hold for any function $\mathbf{A}(t)$, and one may choose the function to be

$$\mathbf{A}(t) = \text{Re}\left[\mathbf{a}e^{\gamma t - \mathrm{i}\omega_0 t}\right]. \tag{3.26}$$

All electrons are assumed to initially reside in completely filled valence bands. Since the valence bands are separated from the conduction bands by an energy gap, the current is expected to be bounded for a sufficiently low frequency:

$$\lim_{\gamma\to 0+}\lim_{\omega_0\to 0}\mathbf{j}(t)\equiv 0. \tag{3.27}$$

The response that naively can be calculated for a truncated basis $\mathbf{j}_N$differs from the actual response that would be calculated with a complete basis set $\mathbf{j}$. The difference is denoted $\Delta\mathbf{j}_N$:

$$\Delta\mathbf{j}_N=\lim_{\gamma\to 0+}\lim_{\omega_0\to 0}\big[\mathbf{j}(t)-\mathbf{j}_N(t)\big]=-\lim_{\gamma\to 0+}\lim_{\omega_0\to 0}\mathbf{j}_N. \tag{3.28}$$

I.e. the actual response vanishes, while the response for for a truncated basis is expected to be non-zero. In the adiabatic limit, $\Delta\mathbf{j}_N$ is a function of $\mathbf{A}(t)$.
The first-order correction to the current density is straightforwardly calculated using first-order perturbation theory. To first order, the time-dependent coefficients of the wave functions expressed in the basis of stationary states are

$$c^{(n)}_{q\mathbf{k}}(t)\approx e^{-\frac{\mathrm{i}}{\hbar}\epsilon_n(\mathbf{k})t}\delta_{qn}-\frac{e}{2\hbar m_0}e^{\left(\gamma-\frac{\mathrm{i}}{\hbar}\epsilon_n(\mathbf{k})\right)t}\left(\frac{e^{-\mathrm{i}\omega_0 t}\big(\mathbf{p}_{qn}(\mathbf{k})\cdot\mathbf{a}\big)}{\omega_{qn}(\mathbf{k})-\omega_0-\mathrm{i}\gamma}+\frac{e^{\mathrm{i}\omega_0 t}\big(\mathbf{p}_{qn}(\mathbf{k})\cdot\mathbf{a}^*\big)}{\omega_{qn}(\mathbf{k})+\omega_0-\mathrm{i}\gamma}\right), \tag{3.29}$$

where the transition frequencies ω_{qn} are expressed in terms of the band energies ϵ_q:

$$\omega_{qn}(\mathbf{k})=\frac{\epsilon_q(\mathbf{k})-\epsilon_n(\mathbf{k})}{\hbar}. \tag{3.30}$$

Using $\mathbf{a}^*=2\mathbf{A}(t)e^{-\gamma t-\mathrm{i}\omega_0 t}-\mathbf{a}e^{-2\mathrm{i}\omega_0 t}$ and taking the limit $\omega_0\to 0$, the current for each valence ban n reduces to

$$\lim_{\omega_0\to 0}\mathbf{j}_{n\mathbf{k}}=-\frac{e}{m_0}\mathbf{p}_{nn}+\frac{e^2}{m_0}\mathbf{A}-\frac{2e^2}{\hbar m_0^2}\sum_i\frac{\mathrm{Re}\left[(\omega_{in}+\mathrm{i}\gamma)\big(\mathbf{p}_{in}\cdot\mathbf{A}\big)\mathbf{p}_{ni}\right]}{\gamma^2+\omega_{in}^2}+\mathcal{O}\left(\mathbf{A}(t)^2\right). \tag{3.31}$$

To obtain the dielectric response, the current is summed over all occupied bands. As long as γ remains finite, all potentially divergent terms arising due to degeneracies cancel. After the cancellation, one can take the limit $\gamma\to 0+$. Summing over all bands and integrating over the first Brillouin zone results in the following expression:

$$\begin{aligned}\lim_{\gamma\to 0+}\lim_{\omega_0\to 0}\mathbf{j}\approx&-\frac{e}{m_0}\sum_{n\in\mathrm{VB}}\int_{\mathrm{BZ}}\frac{d^3\mathbf{k}}{(2\pi)^3}\,\mathbf{p}_{nn\mathbf{k}}\\&-\frac{e^2}{m_0}\int_{\mathrm{BZ}}\frac{d^3\mathbf{k}}{(2\pi)^3}\left\{N_{\mathrm{VB}}\mathbf{A}-\frac{2}{m_0}\sum_{n\in\mathrm{VB}}\sum_{i\neq n}\frac{\mathrm{Re}\Big[\big(\mathbf{p}_{ni}\cdot\mathbf{A}\big)\mathbf{p}_{in}\Big]}{\hbar\omega_{in}}\right\}.\end{aligned} \tag{3.32}$$

The first term on the right-hand side of this expression vanishes as $p_{nn\mathbf{k}}=\nabla_{\mathbf{k}}\epsilon_{n\mathbf{k}}$ are odd functions in $\mathbf{k}$ due to the energy bands $\epsilon_{n\mathbf{k}}$ being even functions in $\mathbf{k}$ whenever time-reversal symmetry is present. The second term is of the form

$$\frac{2A_\alpha}{m_0}\sum_{n\in\mathrm{VB}}\sum_{i\neq n}\frac{\mathrm{Re}[p_{ni\mathbf{k},\alpha}p_{in\mathbf{k},\beta}]}{\hbar\omega_{in}}. \tag{3.33}$$

The Thomas-Reiche-Kuhn sum rule dictates that such terms vanish when integrated over the whole Brillouin zone. If the basis used for calculating the electric responses is truncated, the sums do not vanish, and it will therefore be a source of spurious currents.
Consequently, a truncated basis demands that a correction term has to be introduced to counter the terms that no longer cancel out. For a calculation with N bands the correction terms to first order is therefore:

$$\Delta\mathbf{j}^{(1)} = \frac{e^2}{m_0}\int_{\mathrm{BZ}}\frac{d^3\mathbf{k}}{(2\pi)^3}\left\{N_{\mathrm{VB}}\mathbf{A} - \frac{2}{m_0}\sum_{n\in\mathrm{VB}}\sum_{i\neq n}^{N}\frac{\mathrm{Re}\Big[\big(\mathbf{p}_{ni}\cdot\mathbf{A}\big)\mathbf{p}_{in}\Big]}{\hbar\omega_{in}}\right\}. \tag{3.34}$$

If the crystal symmetry demands that the electric current must flow along the laser polarization, then Eq. (3.34) is equivalent to substituting the actual number of valence bands, N_{VB}, with an effective one, $N_{\mathrm{VB}}^{\mathrm{eff}}$. Indeed, by multiplying both sides of Eq. (3.34) with $\mathbf{A}$ and relying on $\Delta\mathbf{j}^{(1)} \parallel \mathbf{A}$, one may obtain

$$\Delta j^{(1)} = A(t)\frac{e^2}{m_0}\int_{\mathrm{BZ}}\frac{d^3\mathbf{k}}{(2\pi)^3}\left\{N_{\mathrm{VB}} - \frac{2}{m_0}\sum_{n\in\mathrm{VB}}\sum_{i\neq n}^{N}\frac{\Big|\mathbf{e}_{\mathrm{L}}\cdot\mathbf{p}_{in}\Big|^2}{\hbar\omega_{in}}\right\}, \tag{3.35}$$

where $\mathbf{e}_{\mathrm{L}}$ is a unit vector pointing along $\mathbf{A}$. Therefore,

$$N_{\mathrm{VB}}^{\mathrm{eff}} = \frac{2}{m_0}\sum_{n\in\mathrm{VB}}\sum_{i\neq n}^{N}\frac{\Big|\mathbf{e}_{\mathrm{L}}\cdot\mathbf{p}_{in}\Big|^2}{\hbar\omega_{in}}. \tag{3.36}$$

Comparison of this expression with Eq. (2.28) illustrates that the correction amounts to substituting $\mathbf{A}(t)$ with $\mathbf{A}(t)N_{\mathrm{VB}}^{\mathrm{eff}}/N_{\mathrm{VB}}$. For elliptically and circularly polarized external fields, the factor $N_{\mathrm{VB}}^{\mathrm{eff}}$ may be a time-dependent function due to the changing direction of the field.

3.4.1 Demonstration for one-dimensional potential

In order to demonstrate that a reduction in conduction bands can be achieved without compromising convergence, the proposed approximation is used when calculating the response for a one-dimensional system. Compared to a system with three spatial dimensions, this arrangement requires significantly less computational resources to obtain a fully converged solution. The corrections to the current density can be written as an expansion in powers of the vector potential:

$$\Delta j(t) = \sum_n c_n A^n(t). \tag{3.37}$$

The procedure used to generate the first-order correction in the previous section can be generalized to generate higher orders as well. The three lowest order corrections are [150]:

$$c_1 = \frac{e^2}{m_0}\int_{\mathrm{BZ}}\frac{dk}{2\pi}\left\{N_{\mathrm{VB}} - \frac{2}{\hbar m_0}\sum_{n\in\mathrm{VB}}\sum_{i\neq n}^{N}\frac{|p_{in}|^2}{\omega_{in}}\right\}, \tag{3.38}$$

$$c_2 = \frac{3e^3}{\hbar^2 m_0^3}\sum_{n\in\mathrm{VB}}\int_{\mathrm{BZ}}\frac{dk}{2\pi}\left\{\sum_{i\neq n}^{N}\sum_{j\neq n}^{N}\frac{p_{ij}p_{ni}p_{jn}}{\omega_{in}\omega_{jn}} - p_{nn}\sum_{i\neq n}^{N}\frac{|p_{in}|^2}{\omega_{in}^2}\right\}, \tag{3.39}$$

$$c_3 = -\frac{4e^4}{\hbar^3 m_0^4}\sum_{n\in\mathrm{VB}}\int_{\mathrm{BZ}}\frac{dk}{2\pi}\left\{\sum_{i\neq n}^{N}\sum_{j\neq n}^{N}\sum_{\ell\neq n}^{N}\frac{\mathrm{Re}[p_{ji}p_{in}p_{\ell j}p_{n\ell}]}{\omega_{in}\omega_{jn}\omega_{\ell n}} - \right. \tag{3.40}$$

$$\left.\sum_{i\neq n}^{N}\sum_{j\neq n}^{N}\frac{(\omega_{in}+\omega_{jn})\left(\frac{|p_{in}p_{jn}|^2}{2} + p_{nn}\,\mathrm{Re}[p_{ij}p_{ni}p_{jn}]\right)}{\omega_{in}^2\omega_{jn}^2} + p_{nn}^2\sum_{i\neq n}^{N}\frac{|p_{in}|^2}{\omega_{in}^3}\right\}. \tag{3.41}$$

These coefficients only depend on the equilibrium properties of the solid and the initial distribution of electrons in reciprocal space. I.e. they are independent of the laser pulse parameters.

Atomic units are used in the following for the numerical results, i.e. $\hbar = e = m_0 = 1$, unless specified otherwise. The lattice potential is taken to be noncentrosymmetric

$$V(x) = \sum_q\left\{-2.2\left(1-\tanh\big(0.9(x-qa)\big)^2\right) + 0.01\sin\left(\frac{2\pi(x-qa)}{a}\right)\right\}. \tag{3.42}$$

where $a = 9.45$ a.u. $= 5$ Å is the lattice constant. The lowest two energy bands are taken to be fully occupied. This ensures that the most energetic valence band electrons are located at the Γ-points, i.e. at $k = 0$. The energy gap between the second and the third bands equals $\epsilon_3(0) - \epsilon_2(0) = 9$ eV, which is close to the band gap of quartz. For the numerical results presented in this section 61 uniformly spaced crystal momenta were included, and conduction bands with energies up the ϵ_{cut} were included. The cut-off energy is calculated from the bottom of the lowest conduction band. The vector potential is given by:

$$A(t) = -\theta(\tau_{\mathrm{L}} - |t|)\frac{E_0}{\omega_0}\cos^4\left(\frac{\pi t}{2\tau_{\mathrm{L}}}\right)\sin(\omega_0 t), \tag{3.43}$$

where E_0 is the maximum amplitude of the electric field, ω_0 is the central frequency of the laser pulse, $\theta(x)$ is the Heaviside step function, and τ_{L} is related to the full width at half maximum of the envelope of $A^2(t)$:

$$\tau_{\mathrm{FWHM}} = \frac{4\tau_{\mathrm{L}}}{\pi}\arccos\left(2^{-1/8}\right). \tag{3.44}$$

The photon energy is $\hbar\omega_0 = 0.06$ a.u. $= 1.65$ eV, which corresponds to a central wavelength of 750 nm. The width of the pulse is $\tau_{\mathrm{FWHM}} = 4$ fs.

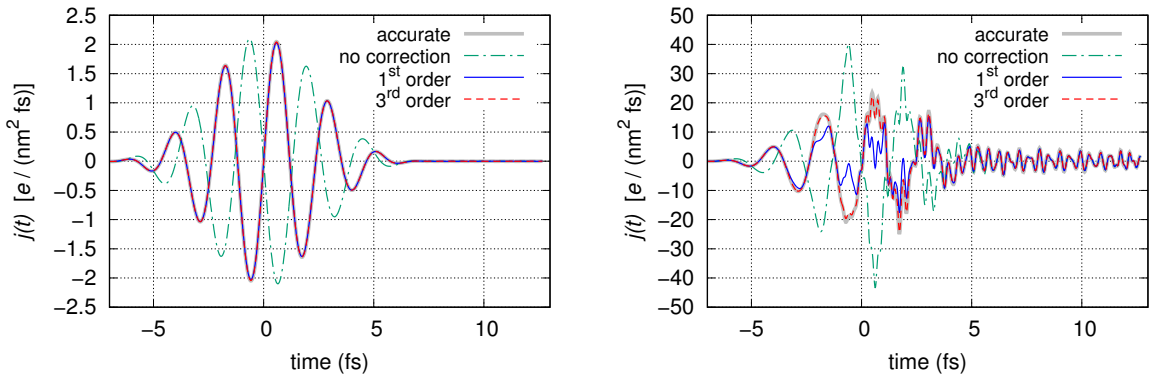

Figure 3.6: The electric current density evaluated for pulses with peak electric fields of (a) 0.1 V/Å and (b) 1 V/Å. The grey curves show current densities evaluated with a cut-off energy that was sufficient for convergence without corrections (2391.4 eV). The other curves represent outcomes of TDSE simulations with $\epsilon_{\mathrm{cut}} = 25$ eV without corrections (green dash-dotted curve), with the first-order correction (solid blue curve), and with the correction terms up to the third order (red dashed curve).

The aim of the numerical results is to show that accurate results can be obtained with less computational resources when the correction terms are applied. To this end, the optically induced current is shown in Figure 3.6 (a) for $E_0 = 0.1$ V/Å and Figure 3.6 (b) for $E_0 = 1.0$ V/Å. In both cases the current density is multiplied by a constant factor $\sigma = 0.1533(\mathrm{nm})^{-2}$ such that the refractive index at the central laser wavelength equals $n_{\mathrm{ref}} = 1.47$, which is the refractive index of thin-film fused silica at 750 nm [37]. It also allows for expressing the current as a three-dimensional current density with units of $e/(\mathrm{nm}^2\,\mathrm{fs})$. The current density labeled as "accurate" is calculated with a cut-off energy of $\epsilon_{\mathrm{cut}} = 2391.4$ eV, which corresponds to using 40 energy bands. This value of ϵ_{cut} is sufficiently large that the results are converged with respect to the number of bands. The other curves are evaluated for $\epsilon_{\mathrm{cut}} = 25$ eV, which corresponds to only keeping the lowest three conduction bands of the one-dimensional model in the simulation. When using such a small number of number of conduction bands, the sum rules are far from being satisfied, and the real-time response deviates significantly from the converged result. Including the first-order correction, specified by Eqs. (3.37) and (3.38), greatly improves the accuracy. For a peak electric field of $E_0 = 1.0$ V/Å, significant deviations to the converged results occur when using the first-order correction, but the deviations are further reduced when the third-order correction are included as well. The second order corrections vanish for systems where both the energy bands and the distributions of electron are symmetric functions of k. This demonstrates that the corrections are useful for predicting both simple linear optical responses and highly nonlinear responses. As the corrections are adiabatic, they only affect the response for times where the vector potential is present.

In order to further quantify the significance of the correction terms, the relative devia-

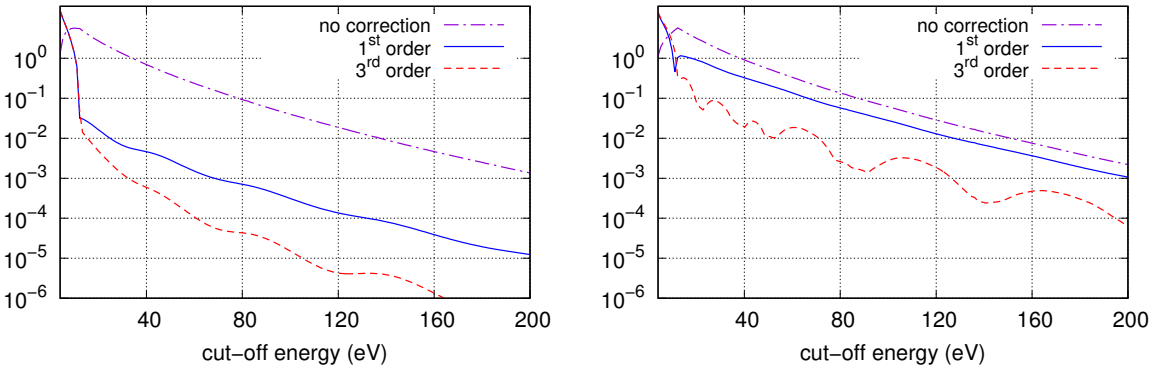

Figure 3.7: Discrepancies between accurate and approximate current densities evaluated using Eq. (3.45) for (a) $E_0 = 0.1$ V/Å and (b) $E_0 = 1$ V/Å. The results presented here were obtained with $\epsilon_{\text{cut}} = 25$ eV.

tion between the converged current $j(t)$ and a current $j[\epsilon_{\text{cut}}](t)$ obtained using bands up to ϵ_{cut} is defined as:

$$\delta[\epsilon_{\text{cut}}] = \frac{\max_t |j(t) - j[\epsilon_{\text{cut}}](t)|}{\max_t |j(t)|}. \tag{3.45}$$

The deviation as a function of ϵ_{cut} is shown in Figure 3.7 for $E_0 = 0.1$ V/Å and $E_0 = 1.0$ V/Å. For the moderately strong peak field equal to $E_0 = 0.1$ V/Å, the first-order correction reduces δ by two orders of magnitude for cut-off energies above 25 eV. The third-order correction decreases the discrepancy even further, with the improvement being best for high cut-off energies.

The improvement due to the analytical corrections is less dramatic at the higher field strength $E_0 = 1$ V/Å, but the third-order correction roughly reduces the deviation by an order of magnitude. The dependency on the cut-off energy is shown for a continuous range of electric fields strengths in Figure 3.8. In panel (a) only the first-order correction is applied, while both first- and third-order corrections are applied to the current in panel (b). The results show that it is indeed possible to significantly increase the accuracy of results obtained in the velocity gauge with the help of correction terms when the sum rules are not satisfied. This is important since numerical implementations require a truncation of the basis, and thus invariably violate the sum rules .In calculations done for three spatial dimensional it may also be necessary to truncate the number of bands due to constraints on computational resources. Surprisingly, the deviation does not decrease monotonously with the cut-off energy cf. Figure 3.7, and for a few selected cut-off energies the it doesn't increase monotonously with the field strength, cf. Figure 3.8. The success of the corrections indicate that further developments in this direction can reduce the computational load even further. It is encouraging that the success of the correction terms is not limited to linear responses. While the method was developed by considering the static limit of the electric fields, the numerical demonstration proves that the approach is relevant for

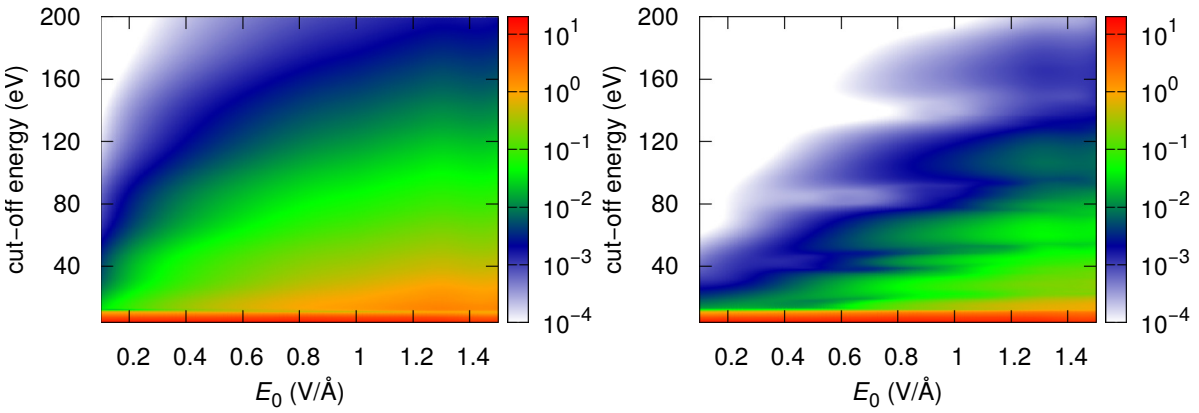

Figure 3.8: The discrepancy, δ, between the accurate current density and that evaluated with corrections up to (a) the first and (b) the third order.

femtosecond pulses in the near-infrared regime. Generalizations to systems with partially filled bands are also possible.

3.5 Conclusion

Numerical considerations for solving the time-dependent Schrödinger equation and the master equation for electrons subject to strong, time-dependent electric fields were presented. The approaches discussed here have been implemented in the publicly available open-source package `ulmic`. This includes a new scheme for calculating the dynamics of mixed quantum states in the length gauge, which was introduced in Chapter 2.
Numerical results for optical excitation of electrons in one-dimensional potentials were presented. In contrast to electrons in three-dimensional potentials, convergence of the optical response could readily be obtained to a very high degree. An excellent agreement between results obtained in the velocity gauge using conventional approaches and the length gauge was demonstrated. It was also verified that the electric current in both cases could be determined from two numerically independent operators for mixed systems. Consequently, these demonstrations also confirmed the usefulness and the gauge-invariance of Lindblad operator that can be constructed from the field-free Hamiltonian.
In order to reduce the computational load for calculations with non-vanishing vector potentials, the Monte Carlo Wave Function method was shown to work in the strong field regime. Adiabatic corrections were also considered, and demonstrated to work well in reducing the computational requirements for modeling electrons in one-dimensional potentials.

Chapter 4

Strong-field, resonant excitations of semiconductors

Resonant excitations can be simple in atomic systems, and the optical response of a semiconductor bears strong resemblance to that of an atomic system in certain regimes. However, the high density of electrons in solids leads to an absence of discrete, clearly separable energy levels. Moreover, the strong coupling to the environment limits the duration over which quantum coherence is preserved, and it is generally orders of magnitudes shorter than for atomic systems. The microscopic dynamics are therefore more complex than that of atomic systems, but understanding the optical responses for semiconducting media is important for developing electro-optical semiconducting devices.

While several studies in the recent years focused on light-solid interactions dominated by either interband or intraband dynamics, the aim of this chapter is to consider a regime where both effects are present. To this end, numerical calculations are carried out to model the interaction of a strong, resonant few-femtosecond pulse with bulk GaAs. Both excitation dynamics and generation of optically induced currents are examined in detail.

4.1 Introduction

Recent papers on strong-field interactions of short pulses have dealt with systems where none of the spectral components of the pulse were in resonance with the fundamental band gap [41, 103, 109, 64, 108, 105, 78, 126, 53, 127]. In those studies the band gap of the medium was several times larger than the central frequency of the light. Consequently, the absorption of several photons is needed to excite an electron to a conduction band. To first order, such materials are transparent with respect to the incoming light, and the light-induced processes are largely reversible due to the inefficient excitation process [103, 109, 108]. A plausible explanation why non-resonant cases were mostly studied is that materials would undergo irreversible structural changes and ultimately get ablated if resonant excitations at these field strengths were considered. For non-resonant transitions, much higher field strengths can be applied before laser ablation occurs. Just below the damage threshold, one may expect the interband and intraband dynamics to be strongly coupled.

Gallium arsenide is a widely studied material, and it is well suited for studying resonant excitations. It has an experimentally measured direct band gap of $E_g = 1.42$ eV at room temperature, and this photon energy is readily accessible with existing laser technology. When bulk GaAs is excited with a weak laser pulse with photon energy $\hbar\omega_{\mathrm{L}} = E_g$, the excitation dynamics is mostly limited to electrons at the band edge. The dynamics for those electrons resembles that of electrons in an atomic system, because of the negligible importance of intraband motion. The dynamics is then dominated by the interband response and characterized by the Rabi frequency:

$$\hbar\omega_{\mathrm{Rabi}} = d_{cv}F_0, \tag{4.1}$$

where F_0 is the field strength and d_{cv} is the dipole moment between the lowest conduction band and the uppermost valence band. Analytical solutions exist for low field strengths where $\hbar\omega_{\mathrm{Rabi}} \ll E_g$, but these solutions are only relevant for atomic systems, as they require the coherence time to be much greater than the duration of an optical cycle. At high field strengths, i.e. $\hbar\omega_{\mathrm{Rabi}} \sim E_g$ the dynamics is highly nonlinear, and this regime is referred to as carrier-wave Rabi flopping. In this regime, it is insufficient to describe the electric fields in terms of an envelope and a central frequency. The actual positions of the maxima of the oscillating field become important, and the dynamics depend on the carrier-envelope phase φ_{CE}. At such field strengths, a Rabi frequency can still be defined for the optical transitions in a solid, but the significance of the individual Rabi frequencies between pairs of states becomes less pronounced due to the number of closely-lying energetic states and the **k**-dependence of transition matrix elements.

The intraband motion causes the crystal momentum of the electrons to change at a rate proportional to the instantaneous field strength. As the Brillouin zone is periodic in the crystal momentum, the frequency at which electrons traverse the Brillouin zone and return to their initial crystal momentum is described by the Bloch frequency:

$$\hbar\omega_{\mathrm{Bloch}} = eF_0a_{\mathrm{lat}}. \tag{4.2}$$

The effect of intraband motion is generally negligible when $\hbar\omega_{\mathrm{Bloch}} \ll \hbar\omega_{\mathrm{L}}$ because the field changes reverses direction faster than a significant displacement in the Brillouin zone can occur.

In order to observe resonant, strong-field interactions in solids, it is therefore necessary that $\hbar\omega_{\mathrm{L}} \sim E_g$, and that neither the Bloch frequency nor the Rabi frequency are significantly smaller than the laser frequency. On physical grounds, it may be expected that $|d_{cv}| \approx e a_{\mathrm{lat}}$, as these quantities have the same dimensions, and are both related to the dimensions of the unit cell potential. Consequently, the following relations hold in the carrier-wave Rabi flopping regime for solids:

$$\hbar\omega_{\mathrm{Bloch}} \approx \hbar\omega_{\mathrm{Rabi}} \approx E_g. \tag{4.3}$$

Under these conditions, the intraband dynamics may fundamentally affect the resonant excitation. This has been a hitherto unexplored regime, and will therefore be the focus of this chapter. The resulting dynamics may, however, deviate significantly from the carrier-wave Rabi flopping observed in atomic systems due to the interplay between interband and intraband dynamics. The estimates presented here ignore many-particle effects such as renormalization of the band gap that occurs during the build-up of charge carriers, which is known to happen at high fields. However, the excitation process and the intraband dynamics occur on time scales smaller than typical collision times, so the many-body effects are presumed to be negligible.

Effects such as electron–electron collisions, momentum relaxation and recombination of electrons with holes occur on different time scales. While electron–electron collisions occur on time scales of 10 fs- 100 fs, relaxation of momentum occurs on time scales 100 fs - 1 ps, and recombination typically occur on time scales of 1 ns, i.e.

$$\tau_{\mathrm{coll}} \ll \tau_{\mathrm{relax}} \ll \tau_{\mathrm{recomb}}. \tag{4.4}$$

Determining these decay times *ab initio* is a non-trivial task, and accounting for all of these effects complicates the dynamics even further. When considering the response to a few-fs pulses a phenomenological dephasing is expected to be a sufficient approximation to the non-Hamiltonian part of the dynamics.

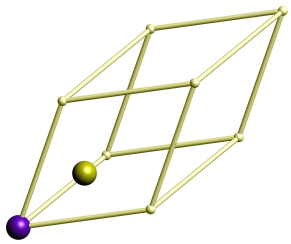

Figure 4.1: Primitive unit cell of GaAs containing exactly one Ga atom and one As atom. Inversion symmetry is visibly broken along the line intersecting both atoms.

4.2 Properties of GaAs and field parameters

GaAs is not only studied well, and used in many technological applications, it is also a simple and representative semiconductor. Non-destructive measurements on GaAs were carried out in the resonant regime at high field strengths [85], and measurements of the damage threshold were considered in [54]. GaAs has a face-centered crystal structure, and lacks a center of inversion symmetry. The primitive lattice vectors are

$$\mathbf{a}_1 = (0, a_{\text{lat}}/2, a_{\text{lat}}/2),\ \mathbf{a}_2 = (a_{\text{lat}}/2, 0, a_{\text{lat}}/2),\ \mathbf{a}_3 = (a_{\text{lat}}/2, a_{\text{lat}}/2, 0),$$

and the reciprocal lattice vectors are

$$\mathbf{b}_1 = (-2\pi/a_{\text{lat}}, 2\pi/a_{\text{lat}}, 2\pi/a_{\text{lat}}),\ \mathbf{b}_2 = (2\pi/a_{\text{lat}}, -2\pi/a_{\text{lat}}, 2\pi/a_{\text{lat}}),$$
$$\mathbf{b}_3 = (2\pi/a_{\text{lat}}, 2\pi/a_{\text{lat}}, -2\pi/a_{\text{lat}}).$$

In reciprocal space, the fundamental band gap is located at the $\Gamma = (0, 0, 0)$. The path from the Γ-point to one of the high-symmetry points $X = (2\pi/a_{\text{lat}}, 0, 0)$, located at the border of the first Brillouin zone, can be parameterized as $\lambda(\mathbf{b}_2 + \mathbf{b}_3)$ for $\lambda \in [0, 0.5]$. Similarly the path from $\Gamma = (0, 0, 0)$ to $L = (\pi/a_{\text{lat}}, \pi/a_{\text{lat}}, \pi/a_{\text{lat}})$ is parameterized as $\lambda(\mathbf{b}_1 + \mathbf{b}_2 + \mathbf{b}_3)$.

Since the location of the Ga and As atoms in the reduced coordinates are $\mathbf{r}_{\text{Ga}} = (1/4, 1/4, 1/4)$ and $\mathbf{r}_{\text{As}} = (0, 0, 0)$, the lattice potential along the direction $\mathbf{a}_1+\mathbf{a}_2+\mathbf{a}_3 \parallel \mathbf{b}_1+\mathbf{b}_2+\mathbf{b}_3 \parallel |\vec{\Gamma L}|$ has no center of inversion. An electric field which is polarized along this direction can therefore lead to optical rectification and generate even-numbered harmonics. On the contrary, the lattice potential has a center of symmetry along $\mathbf{a}_2 + \mathbf{a}_3 - \mathbf{a}_1 \parallel \mathbf{b}_2 + \mathbf{b}_3 \parallel |\vec{\Gamma X}|$ and no even harmonics can be generated.

A significant reduction of the computation time can be achieved by considering the dynamics along a single line in the Brillouin zone. This is possible as long as the external field is linearly polarized and the calculations are done in the independent particle approximation. The total three-dimensional response can in principle be obtained by performing a series of one-dimensional calculations. In this work, only the line that intersects the Γ-point at the centre of the Brillouin zone and one of the X-points at the border of the first Brillouin zone is considered. Most of the electrons are expected to be excited at the Γ–point, as this is the location of the fundamental band gap. As the direction of

the electric field is parallel to this line in reciprocal space, only electrons with an initial crystal momentum along this line will ever get accelerated to the Γ-point. Electrons with an initial crystal momentum that is far from this particular line of crystal momenta only undergo non-resonant dynamics. The residual excitation density away from the Γ-point is therefore expected to be much lower.

Calculating the dynamics *ab initio* is composed of two steps. First, the valence and conduction band orbitals are calculated using Wien2k, and in the second step the master equation is solved. The ground state wave functions in GaAs are calculated on a Monkhorst-Pack grid with $16 \times 16 \times 16$ $\mathbf{k}$ points using the LDA exchange-correlation potential. The band gap is however only 0.41 eV, which is significantly less than the experimentally observed value of 1.42 eV. Once a converged set of wave functions is obtained, the modified Becke–Johnson Trans-Blaha potential is applied [123]. More specifically, the TB09 meta-GGA exchange-correlation potential [123] was used together with spin-orbit coupling. This increases the band gap to 1.55 eV, which is in much better agreement with experiments. This value also happens to be close to the band gap measured at cryogenic temperatures, which is 1.52 eV [15]. The most energetic valence bands and the lowest lying conduction bands are shown in Figure 4.2 (a). The valence bands are referred to as the split-off band (so), the light hole band (lh) and the heavy hole band (hh) in the literature, and the three lowest conduction bands are here referred to as c_1, c_2 and c_3. To calculate the dynamics in the length gauge, it is however necessary to obtain the dipole matrix elements, which can be constructed from the momentum matrix elements and the energies

$$\mathbf{d}_{ij}(\mathbf{k}) = \mathrm{i}e\hbar \frac{\mathbf{p}_{ij}(\mathbf{k})}{m_0[E_i(\mathbf{k}) - E_j(\mathbf{k})]} \tag{4.5}$$

for $i \neq j$. Since only a single line in the Brillouin zone is considered, it is possible to find a gauge in which the matrix elements are smooth functions of the crystal momentum. As GaAs does not have a center of inversion, the matrix elements can be complex. If a center of inversion symmetry were present, the phase ambiguity of the matrix elements can be reduced to a factor of -1. Symmetry arguments can, however, still be applied, as the crystal is symmetric with respect to inversion along the direction of the external electric field. In this case, transition elements can be divided into real matrix elements that are symmetric with respect to $\mathbf{k}$ and imaginary matrix elements that are antisymmetric with respect to $\mathbf{k}$.

After applying an iterative approach to find a smooth gauge, a spline interpolation procedure is then applied to both energies and matrix elements. This is necessary to resolve the $\mathbf{k}$-dependent dynamics in details. The number of $\mathbf{k}$ points between the endpoints $\Gamma = (0, 0, 0)$ and $\Gamma' = (4\pi/a)$ thus increases from 16 to 600. The dipole matrix element magnitudes along this line are shown in Figure 4.2 (b) for the strongest coupled bands. It shows that the transitions are strongest at the centre of the Brillouin zone.

The band structure is also used to obtain the reduced electron mass by fitting the gap between the lowest conduction band and the light-hole band with a second-order

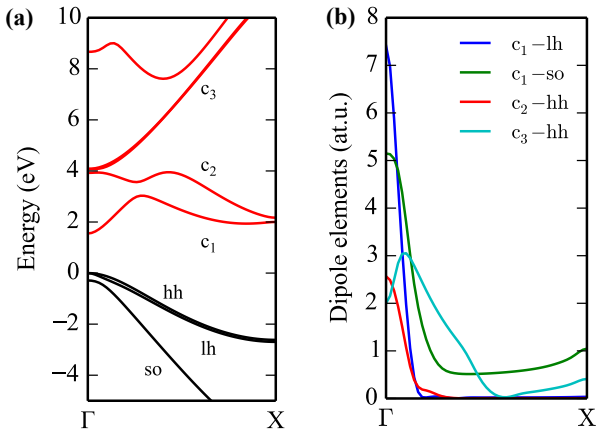

Figure 4.2: (a) The energies of the three highest valence bands (black) and the five lowest conduction bands (red) of GaAs along the line from the Γ-point to an X-point. All of the bands are doubly degenerate. (b) Magnitude of the dipole moments $|\mathbf{d}_{ij}(\mathbf{k})|$ for the most important interband transitions.

polynomial within $|\mathbf{k}| \leq 0.05 k_{\max}$. The result is $0.053 m_0$, which is in agreement with the experimentally measured effective mass.

In the second step, the dynamics is calculated using the semiconductor Bloch equations in the form of the master equation with phenomenological dephasing:

$$\frac{\partial}{\partial t}\rho_{\mathbf{k},ij} = \left[\frac{\delta_{ij}-1}{T_2} + \frac{\mathrm{i}}{\hbar}(E_{i\mathbf{k}} - E_{j\mathbf{k}})\right]\rho_{\mathbf{k},ij} + \frac{1}{\hbar}\mathbf{F}(t)\cdot\left(e\nabla_{\mathbf{k}}\rho_{\mathbf{k},ij} - \mathrm{i}[\hat{\mathbf{d}},\hat{\rho}_{\mathbf{k}}]_{ij}\right). \tag{4.6}$$

The diagonal elements of the density matrix, $n_i(\mathbf{k},t) = \rho_{ii}(\mathbf{k},t)$, are dimensionless probabilities to find an electron with crystal momentum $\mathbf{k}$ in band i. T_2 is dephasing time and $e > 0$ is the elementary charge. Since Eq. (4.6) is a first order, linear, partial differential equation with periodic boundary conditions it is straightforward to solve the equation numerically using the Crank-Nicholson scheme [25].
The electric field of the laser pulse in the medium $\mathbf{F}(t)$ is taken to be linearly polarized along the Γ–X direction in the Brillouin zone of GaAs, where the X point is at $\mathrm{X} = (k_{\max}, 0, 0) = (1.11\,\text{Å}^{-1}, 0, 0)$. The field projection on the Γ–X direction is denoted by $E(t)$ and its amplitude by E_0.

It is desirable to study interactions for an electric field which has a bounded frequency spectrum and an envelope with a single major peak. The field can therefore be defined to have a compact support in the frequency domain, and a Nuttall window can be used to reduce the magnitude of the pedestals in the time domain. An explicit expression for the positive-frequency part of the pulse spectrum that satisfies theses requirements is

$$\tilde{F}(\omega) = \tilde{F}_0 \exp(\mathrm{i}\varphi_{\mathrm{CE}})w\big[(\omega-\omega_0+\Delta\omega)/(2\Delta\omega)\big], \tag{4.7}$$

where φ_{CE} is the carrier-envelope phase. The Nuttall window is defined as

$$w(\omega) = \theta(\omega+\Delta\omega-\omega_0)\theta(\Delta\omega+\omega_0-\omega)\sum_{n=0}^{3} a_n \cos\left(\frac{2\pi n(\omega-\omega_0)}{2\Delta\omega}\right) \tag{4.8}$$

where $\theta(\omega)$ is the Heaviside step function. The coefficients are $a_0 = 0.355768$, $a_1 = -0.487396$, $a_2 = 1/2 - a_0$, and $a_3 = -(1/2 + a_1)$. The Nuttall window is centered at $\omega_0 = \hbar^{-1}E_g$ with a compact support in the interval $E_g - \hbar\Delta\omega \le \hbar\omega \le E_g + \hbar\Delta\omega$ where $\hbar\Delta\omega = 0.8$ eV. The central wavelength of the pulse is $\lambda_0 = 2\pi c/\omega_0 = 800$ nm, which results in a central photon energy of $\hbar\omega_0 = 1.55$ eV.

All spectral components are taken to be in phase in order to obtain a Fourier-transform limited pulse. The pulse has a full width at half maximum (FWHM) of 5 fs in the time domain, and it is truncated at $t_{\min} = -36.2$ fs and $t_{\max} = 36.2$ fs. The field $F(t)$ is shown in Figure 4.3(a) in the time domain, and Figure 4.3(b) shows the power spectrum of the pulse $|F(\omega)|^2$ after the truncation in the time domain.

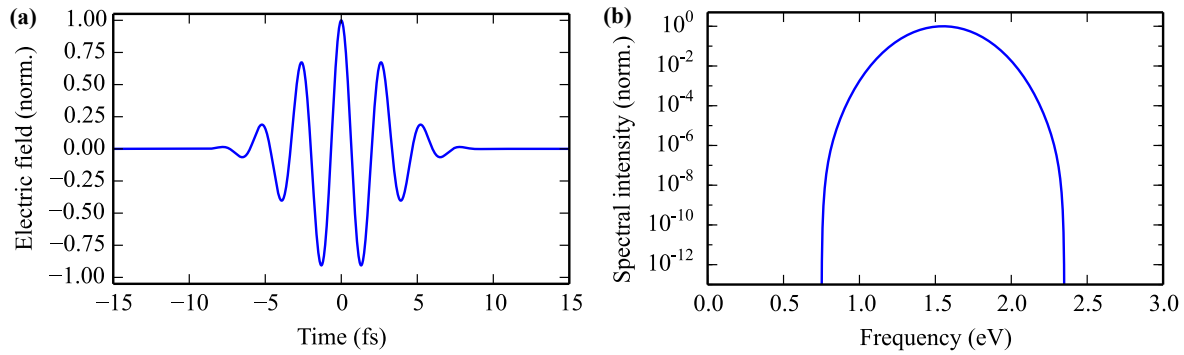

Figure 4.3: (a) Normalized electric field $F(t)$ inside the medium for $\phi_{\mathrm{CE}} = 0$. (b) The power spectrum of the laser pulse $|F(\omega)|^2$.

4.3 Control of optically induced currents

Before considering the excitation dynamics in detail, it is relevant to first consider how the residual excitations and optically induced residual currents depend on the field strength and the carrier-envelope phase of the pulse. This also helps to identify the various regimes of non-linear dynamics. The dynamical equations are solved for various electric field strengths and carrier-envelope phases while the spectrum of the pulse is kept constant. The macroscopic responses are easiest to compare to experimental results, and will be considered first in this section. The microscopic responses are needed to describe the excitation dynamics and are considered afterwards.

The three macroscopic quantities to be considered here are the excitation density n, the electric current j and the transferred charge Q. In the limit of strong interband dephasing, the electric current is dominated by the intraband component, and this component depends solely on the distribution of the excitation density n. Likewise, for a constant intraband current, the transferred charge changes at a constant rate proportional to the residual current.

The number of bands included in the simulations, as well as the dephasing time, are also varied in order to understand their significance. After solving for the dynamics, the residual excitation probability is obtained by integrating over the electron distribution along the Γ–X direction:

$$\bar{n}_{\mathrm{res}}^{(1\mathrm{D})} = \frac{1}{2k_{\max}} \sum_{i\in\mathrm{CB}} \int_{-k_{\max}}^{k_{\max}} \rho_{ii}(t_{\max}, k)\, dk. \tag{4.9}$$

The three-dimensional excitation probabilities are then estimated by noticing that most transition matrix elements from valence bands to the lowest conduction band are only significant for $|\mathbf{k}| \lesssim 0.1k_{\max} = \Delta k$. Within this cylinder, the excitation profile can be approximated as independent of the distance from the symmetry axis, and the three-dimensional excitation probability can be related to the one-dimensional probability by

$$\bar{n}_{\mathrm{res}}^{(3\mathrm{D})} \sim \Delta k^2 \bar{n}_{\mathrm{res}}^{(1\mathrm{D})} a_{\mathrm{lat}}^2/(2\pi). \tag{4.10}$$

A calculation of the residual excitation as function of the maximum electric field strength is shown in Figure 4.4 (a). The density is shown as the probability of any of the conduction bands being occupied. The excitation probability averaged over the whole Brillouin zone is estimated to be $\sim 2.8 \times 10^{21}$ cm^{-3} at a field strength of $F_0 = 0.8$ V/Å. This is below the free-carrier density of 10^{22} cm^{-3}, which is expected to mark the damage threshold [55]. Four sets of parameters are used for the results shown in Figure 4.4, and cover calculations done with six electronic bands, and calculations done with two bands. Although two bands are insufficient for modeling the dynamics that would be observed in an experiment, the results obtained by such calculations are significantly simpler to analyze. In the two-band simulations, only the uppermost valence band (hh) and the lowest conduction band (c_1) are considered. For each of the cases, the dynamics is simulated for a finite dephasing time $T_2 = 10$ fs, and an infinitely long dephasing time $T_2 = \infty$.

For all four sets of parameters, Rabi-like dynamics is expected to occur at low field strengths, and carrier-wave Rabi flopping at higher field strengths. Signatures of carrier-wave Rabi flopping (CWRF) was claimed to have been observed at $F_0 = 0.4$ V/Å at a comparable central laser frequency [84, 86]. This field is much smaller than what is required to accelerate an electron from the Γ point to the boundary of the Brillouin zone, which is $F_0 = 0.9$ V/Å for $\lambda_0 = 800$ nm.

According to Figure 4.4 (a), the Rabi oscillations can only be clearly identified in the two-band model, and in the absence of dephasing. The calculations with six bands shows much smaller modulations in the residual excitation density. Not surprisingly, a finite dephasing time T_2 also reduces the modulations.

Once electrons have been excited to the conduction bands, a residual current remains until the average momentum equilibrates due to momentum relaxation. Since energy and momentum relaxation typically occurs on time scales of 100 fs, these relaxations are neglected when considering the residual currents immediately after the pulses have passed. When neglecting the oscillating interband currents the remaining residual intraband current reads:

$$j(F_0, \varphi_{\mathrm{CE}}, t_{\max}) = -\frac{2e}{(2\pi)^3} \int_{\mathrm{BZ}} d^3k \, \mathrm{Tr}[\rho_{\mathbf{k}}(t_{\max}) \hat{\mathbf{v}}_{\mathrm{intra}}] \cdot \hat{\mathbf{e}} \tag{4.11}$$

$$= -\frac{2e}{(2\pi)^3} \sum_i \int_{\mathrm{BZ}} d^3k \, n_i(\mathbf{k}, t_{\max}) \mathbf{v}_{\mathrm{intra}}(\mathbf{k}) \cdot \hat{\mathbf{e}}. \tag{4.12}$$

The absolute value of the CEP-maximized residual electric current is shown in Figure 4.4 (b), and is defined as

$$j_{\max}(F_0) = \max_{\varphi_{\mathrm{CE}}}[j(F_0, \varphi_{\mathrm{CE}})]. \tag{4.13}$$

When the field is weak, the photocurrent is generated due to interference of one-photon-absorption and two-photon-absorption, also know as ω+2ω interference [4, 35]. In this case,

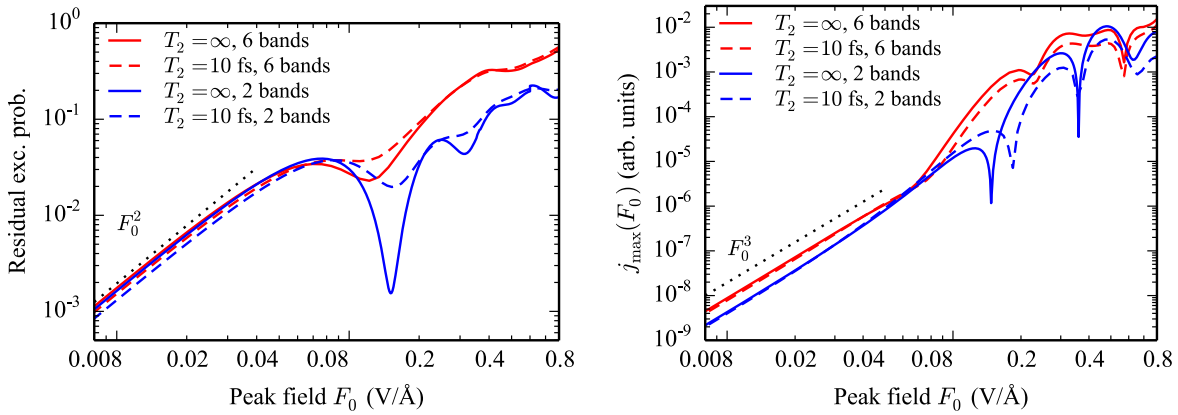

Figure 4.4: (a) Residual excitation probability $\bar{n}_{res}^{(1D)}$ as a function of the peak field. (b) The maximal value of the residual current density when maximizing over the carrier-envelope phase $j_{\max}(F_0) = \max_{\varphi_{CE}}[j(F_0, \varphi_{CE})]$. In both plots, the solid and dashed lines were obtained with $T_2 = \infty$ and $T_2 = 10$ fs, respectively. Red curves represent six-band calculations (3 VBs, 3 CBs), whereas blue curves show the two-band results (1 VB, 1 CB).

it is known that the current scales as $j_{\max}(F_0) \propto F_0^3$, which is also clearly demonstrated in the plot. This scaling is due to the probability amplitudes of one- and two-photon processes are proportional to F_0 and F_0^2, respectively, while their interference makes a contribution proportional to F_0^3.

Similar behavior can be observed in the two-dimensional plots in Figure 4.5 that show the field- and CEP-dependence of the current simultaneously . The current shown in the plots is scaled be the field $F_0^{-3} j_{\text{res}}(F_0, \varphi_{CE})$ for better visibility. This ensures that the scaled current is constant with respect to the field at low field strengths, and highlights deviations from the F_0^3-dependency and the CEP-dependency. From the plots, it is also clear that there is center of inversion symmetry. I.e. reversing the field also reverses the residual current.

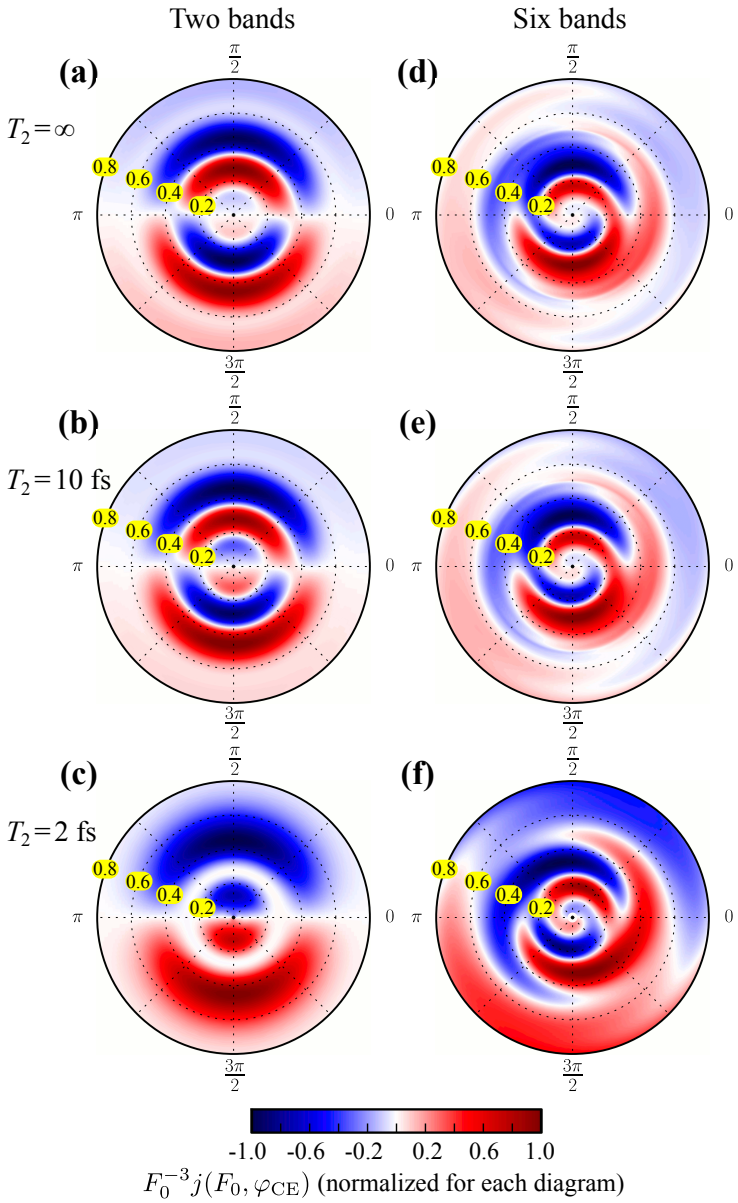

Figure 4.5: The residual current density $j(F_0, \varphi_{CE})$. In these diagrams, the distance to the origin corresponds to the pulse amplitude F_0, which varies from zero to 0.8 V/Å, while the angle to the horizontal axis encodes the carrier-envelope phase φ_{CE}. The color coding of $F_0^{-3} j(F_0, \varphi_{CE})$ is individually normalized for each diagram. Panels (a)–(c) show two-band results (1 VB, 1 CB), while panels (d)–(f) display six-band (3 VBs, 3 CBs) calculation results. Each horizontal pair of plots corresponds to a certain value of dephasing time T_2 as indicated by the labels.

In a subsequent step, the residual current is used to determine the transferred charge,

$$Q\left(F_0, \varphi_{\mathrm{CE}}\right) = \int_{-\infty}^{t_{\mathrm{cut}}} dt\, j\left(F_0, \varphi_{\mathrm{CE}}, t\right), \tag{4.14}$$

where the upper integration limit is set to $t_{\mathrm{cut}} = 8$ fs. The transferred charge is the same as the polarization used in Chapter 2. It has been used in several recent works [103, 66, 91], and may be better suited than the current for experimental verification, as it is expected to decay at an even slower rate than the current.

The plots of the residual current in Figure 4.5 and the transferred charge in Figure 4.6 share a number of similarities, which is not surprising due to the quantities being closely related. In both Figures, panels (a)–(c) show the response for a two-band system. Panel (d)–(f) show the response for calculations with the three lowest conduction bands and the three highest valence bands. These results are qualitatively converged with respect to the number of bands. The merit of the two-band calculations is the simplicity they provide, which makes a detailed analysis tractable. The observed CEP-dependency of both residual current and transferred charge implies that they are due to ultrafast, subcycle processes. The cases of $T_2 = \infty$ and fast dephasing $T_2 = 10$ fs differ very little, which suggests that there is fast effective dephasing within the purely Hamiltonian system described by the Schrödinger equation. Since the exact dephasing mechanisms are not known, and are non-trivial to calculate *ab initio*, the values of T_2 were chosen to represent the various regimes, e.g. $T_2 < 2\pi/\omega_{\mathrm{L}}$ and $T_2 \gg 2\pi/\omega_{\mathrm{L}}$. In comparison, the fastest electron interband dephasing time in GaAs that has been measured experimentally is $T_2 \sim 14$ fs [10], which is within the range of theoretical estimates [133]. At the same time, recent experiments on high-harmonic generation in solids [105, 78, 126, 53, 127] suggest that dephasing times in the strong-field regime may be on the order of a few femtoseconds.

Phenomenological T_2–dephasing has a stronger impact on the two-band results shown in panels (a)–(c) in Figures 4.5 and 4.6. Apparently, coherent effects suffer from effective dephasing induced by intraband motion in the presence of multiple bands. Similarly to Landau damping [69], this phenomenon is not related to electron-electron collisions or interaction with environment. For any chosen CEP, $j\left(F_0, \varphi_{\mathrm{CE}}\right)$ changes its sign at certain values of F_0. In the two-band model, the maximum magnitude of the current at any field amplitude is always obtained for the antisymmetric pulse ($\varphi_{\mathrm{CE}} = \pm\pi/2$).

In the more realistic six-band calculations, the residual current has a non-trivial dependency on the CEP, which causes the appearance of "vortices" in panels (d)–(f). For these calculations, three valence band and three conduction bands were included. Similar behavior is observed for the transferred charge in Figure 4.6. For the transferred charge, the vortex-patterns are even more pronounced. In contrast to the plots of the residual current, the vortex-structure is also visible in the in the two-band simulations.

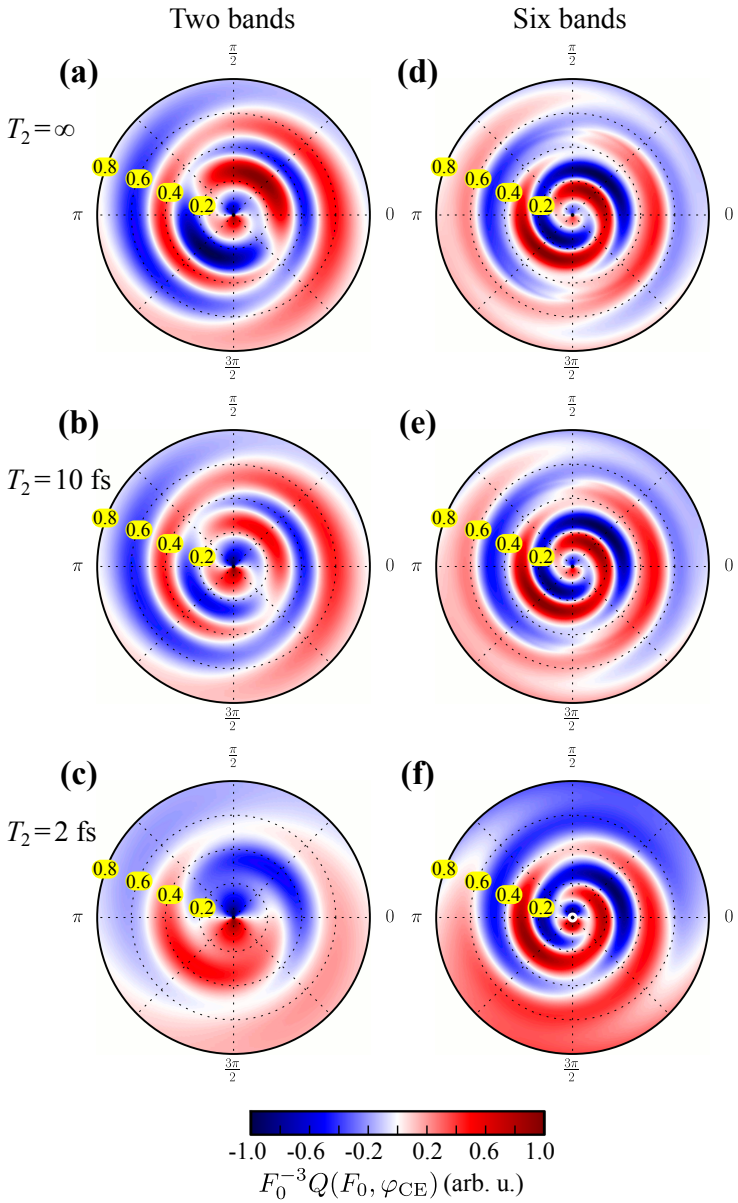

Figure 4.6: The residual current density $Q(F_0, \varphi_{\mathrm{CE}})$. Similarly to Figure 4.5, the distance to the origin corresponds to the pulse amplitude F_0, which varies from zero to 0.8 V/Å, while the angle to the horizontal axis encodes the carrier-envelope phase φ_{CE}. The color coding of $F_0^{-3}Q(F_0, \varphi_{\mathrm{CE}})$ is individually normalized for each diagram. Panels (a)–(c) show two-band results (1 VB, 1 CB), while panels (d)–(f) display six-band (3 VBs, 3 CBs) calculation results. Each horizontal pair of plots corresponds to a certain value of dephasing time T_2 as indicated by the labels.

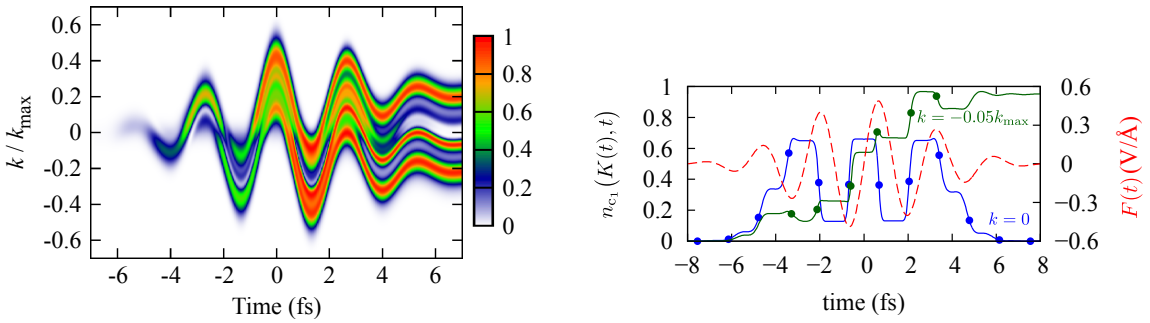

Figure 4.7: (a) Temporal evolution of the conduction-band population in a two-band simulation for $F_0 = 0.5$ V/Å, $\varphi_{\mathrm{CE}} = \pi/2$, $T_2 = \infty$. (b) Time dependence of the CB population in the two-band simulation (blue and green curves). It is calculated along reciprocal-space pathways $K(t)$ that satisfy the acceleration theorem. The starting point is the Γ point ($k = 0$) for the blue curve and $k = -0.05k_{\mathrm{max}}$ for the green curve. The bold dots on the curves denote moments of passage in the vicinity of the Γ point. The dashed red curve shows the electric field of the pulse ($F_0 = 0.5$ V/Å, $\varphi_{\mathrm{CE}} = \pi/2$).

4.4 Intraband-assisted kicked excitations

To analyze the origin of the currents in further detail, the time-dependent, k-resolved population of the lowest conduction band is shown in in Figure 4.7 (a). The plot confirms that interband transitions mainly take place near the Γ point, and that electron wave packets excited by different laser half-cycles interfere with each other. The interference affects the residual reciprocal-space population distributions, and asymmetric distributions eventually leads to a residual, ballistic electric current. Figure 4.7 (b) shows the time-dependent excitation probability of electrons with an initial crystal momentum of $k = 0$ and $k = 0.05k_{\mathrm{max}}$. The Figure illustrates that the excitation probabilities only change significantly whenever the electrons passes the Γ-point. Moreover, it also shows that the excitations can interfere either constructively or destructively and lead to very different residual excitation probabilities.

Motivated by the step-like change in excitation probability and the fact that the dipole moments are strongly peaked at the Γ-point, the excitation may be described by a model where the electrons are excited at discrete moments in time. I.e. one can consider an intraband-assisted "kick-like" interband transitions, which occurs whenever an electron passes the Γ-point, and every transition may interfere constructive of destructively with the previous transition. This type of dynamics is reminiscent of the dynamics observed for the "kicked" rotor, e.g. [39].
The crystal momentum of an electron with an initial crystal momentum $\mathbf{k}_0$ evolves as

$$\mathbf{K}(t) = \mathbf{k}_0 - \frac{e}{\hbar}\int_{t_0}^{t} \mathbf{F}(t')dt'. \tag{4.15}$$

Consequently, the energy difference between the original band v_i and the lowest conduction

band c_1 changes as $\Delta E_{c_1 v_i}(\mathbf{K}(t))$ and the dipole matrix element changes as $\mathbf{d}_{ij}(\mathbf{K}(t))$. In the following analysis, interband phase relaxation is neglected, i.e. $T_2 \to \infty$, so the analysis can be performed for wave functions instead of density matrices. Therefore, it is sufficient to consider the time-dependent Schrödinger equation instead of the master equation. The semiconductor Bloch equation for a one-dimensional system can be transformed from a partial to an ordinary differential equation [21, 65]. To do so, the following ansatz is used for the electronic wave function in order to eliminate the term proportional to $\nabla_{\mathbf{k}}$:

$$|\Psi_{\mathbf{k}}(t)\rangle = \sum_i \alpha_{i,\mathbf{k}}(t) e^{-\frac{\mathrm{i}}{\hbar}\int_{t_0}^{t} dt' \, E_i\left(\mathbf{K}(t')\right)} |\psi_i\big(\mathbf{K}(t)\big)\rangle, \tag{4.16}$$

where $\alpha_{i,\mathbf{k}}$ is the occupation coefficient for band i. Inserting the ansatz into the time-dependent Schrödinger equation yields the following differential equation:

$$\frac{d}{dt}\alpha_{i,\mathbf{k}}(t) = -\frac{\mathrm{i}}{\hbar}\sum_j \alpha_{j,\mathbf{k}}(t)\mathbf{F}(t)\cdot\mathbf{d}_{ij}\big(\mathbf{K}(t)\big)\exp\left[\frac{\mathrm{i}}{\hbar}\int_{t_0}^{t} dt' \Delta E_{ij}\big(\mathbf{K}(t')\big)\right]. \tag{4.17}$$

The dipole matrix elements $\mathbf{d}_{ij}(\mathbf{K}(t))$ thus depends on time via the crystal momentum, and are strongly peaked at the times t_n when the electron passes the Γ-point. Assuming that the excitations occur at discrete moments in time, the dipole is then approximated as

$$\mathbf{d}_{ij}\big(\mathbf{K}(t)\big) \approx \sum_n \delta(t-t_n)\int_{t_n-\Delta t}^{t_n+\Delta t} dt\, \mathbf{d}_{ij}\big(\mathbf{K}(t)\big), \tag{4.18}$$

where $\delta(t)$ is the Dirac delta-function. The integration is performed over a short interval of time ($\Delta t \ll t_{n+1} - t_n$) during which transitions are most probable, and the integration variable can be changed from time to crystal momentum:

$$\int_{t_n-\Delta t}^{t_n+\Delta t} dt\, \mathbf{d}_{ij}\big(\mathbf{K}(t)\big) = \int_{\mathbf{K}(t_n-\Delta t)}^{\mathbf{K}(t_n+\Delta t)} \frac{dk}{|\mathbf{K}'(t)|}\,\mathbf{d}_{ij}(\mathbf{K}(t)) \approx -\frac{\hbar}{e|F(t_n)|}\int_{-\Delta k}^{\Delta k} dk\, \mathbf{d}_{ij}\left(\mathbf{K}(t_n)+k\hat{\mathbf{e}}\right), \tag{4.19}$$

where $\Delta k = e\hbar^{-1}|F_0| \sim |\mathbf{K}'(t_n)|\,\Delta t$. Introducing

$$D_{ij}(\mathbf{k},t_n) = \frac{1}{e}\int_{-\Delta k}^{\Delta k} dk\, \mathbf{d}_{ij}\left(\mathbf{K}(t_n)+k\hat{\mathbf{e}}\right), \tag{4.20}$$

Eq. (4.17) can then be written as

$$\frac{d}{dt}\alpha_{i,\mathbf{k}}(t) \;\approx\; \mathrm{i}\sum_j \alpha_{j,\mathbf{k}}(t)\exp\left[\frac{\mathrm{i}}{\hbar}\int_{t_0}^{t} dt' \Delta E_{ij}\big(\mathbf{K}(t')\big)\right]\sum_n \delta(t\,-\,t_n)\mathrm{sgn}[F(t_n)]D_{ij}(\mathbf{k},t_n). \tag{4.21}$$

In this model, the probability amplitudes stay constant between kicks, and they change their values abruptly at each kick. A general solution of Eq. (4.21) can be written in the matrix form. For one particular transition at time t_n,

$$\alpha_{\mathbf{k}}(t_n + \Delta t) = e^{\mathrm{i}\hat{M}(\mathbf{k},t_n)}\alpha_{\mathbf{k}}(t_n - \Delta t), \tag{4.22}$$

where the elements of matrix $\hat{M}(\mathbf{k}, t_n)$ are given by

$$M_{ij}(\mathbf{k}, t_n) = \mathrm{sgn}[F(t_n)]D_{ij}(\mathbf{k}, t_n) \exp\left[\frac{\mathrm{i}}{\hbar}\int_{t_0}^{t_n} dt' \Delta E_{ij}\big(\mathbf{K}(t')\big)\right]. \tag{4.23}$$

Whenever the probability of a particular transition is small the exponent can be expanded in a Taylor series $e^{\mathrm{i}\hat{M}(\mathbf{k},t_n)} \approx 1 + \mathrm{i}\hat{M}(\mathbf{k}, t_n)$. In this approximation,

$$\Delta\alpha_{i,\mathbf{k}}(t_n) = \alpha_{i,\mathbf{k}}(t_n + \Delta t) - \alpha_{i,\mathbf{k}}(t_n - \Delta t) \tag{4.24}$$

$$\approx \mathrm{i}\,\mathrm{sign}[F(t_n)] \sum_j \left\{ \alpha_{j,\mathbf{k}}(t_n - \Delta t) D_{ij}(\mathbf{k}, t_n) \exp\left[\frac{\mathrm{i}}{\hbar}\int_{t_0}^{t_n} dt' \Delta E_{ij}\big(\mathbf{K}(t')\big)\right]\right\}. \tag{4.25}$$

Whether two particular excitation events at times t_{n_1} and t_{n_2} interfere constructively or destructively depends on the relative phase between $\Delta\alpha_{i,\mathbf{k}}(t_{n_1})$ and $\Delta\alpha_{i,\mathbf{k}}(t_{n_2})$, which is given by $\Delta\phi(\mathbf{k}) = \arg\left[\Delta\alpha^*_{i,\mathbf{k}}(t_{n_1})\Delta\alpha_{i,\mathbf{k}}(t_{n_2})\right]$. For transitions from band j to band $i \neq j$, Eq. (4.24) then yields

$$\Delta\phi_{ij}(\mathbf{k}) = \arg\left\{ \mathrm{sgn}[F(t_{n_1})F(t_{n_2})]\alpha^*_{j,\mathbf{k}}(t_{n_1} - \Delta t)\alpha_{j,\mathbf{k}}(t_{n_2} - \Delta t) D^*_{ij}(\mathbf{k}, t_{n_1}) D_{ij}(\mathbf{k}, t_{n_2}) \right.$$

$$\left. \times \exp\left[\frac{\mathrm{i}}{\hbar}\int_{t_{n_1}}^{t_{n_2}} dt' \Delta E_{ij}\big(\mathbf{K}(t')\big)\right]\right\}. \tag{4.26}$$

If both transitions take place at the same $\mathbf{k}$ (e.g. $\mathbf{k} = 0$), then $D_{ij}(\mathbf{k}, t_{n_1}) = D_{ij}(\mathbf{k}, t_{n_2})$. For small transition probabilities, the change of phase of the initial state $\arg[\alpha^*_{j,\mathbf{k}}(t_{n_1} - \Delta t)\alpha_{j,\mathbf{k}}(t_{n_2} - \Delta t)]$ can be neglected. This leads to the following result:

$$\Delta\phi_{ij}(\mathbf{k}) \approx \frac{\pi}{2}\Big(1 - \mathrm{sgn}[F(t_{n_1})F(t_{n_2})]\Big) + \frac{1}{\hbar}\int_{t_{n_1}}^{t_{n_2}} dt' \Delta E_{ij}\big(\mathbf{K}(t')\big). \tag{4.27}$$

The first term on the right-hand side of this equation disappears if t_{n_1} and t_{n_2} are separated by a full laser cycle, and it is equal to π if the laser field changes its sign between these two moments of time. Two kicks that promote electrons from band j to band i at times t_1 and t_2 interfere with each other according to the phase accumulated by the interband polarization between the kicks. For a particular electron with initial crystal momentum $\mathbf{k}$, this phase is approximately given by

$$\Delta\phi_{ij}(\mathbf{k}) = \frac{1}{\hbar}\int_{t_1}^{t_2} dt\, \Delta E_{ij}\big(\mathbf{K}(t)\big). \tag{4.28}$$

It is analogous to the Volkov phase [146] in atomic physics. When $\Delta\phi_{ij}(\mathbf{k}) = 2\pi q$, where integer q is the order of a nonlinear resonance, interference is constructive resulting in net excitation of electrons.

4.5 Effects of intraband motion

The kick-like transition described in the previous section is a clear manifestation of intraband-assisted excitations, and is denoted as "kicked anharmonic Rabi oscillations". Consequently, intraband-assisted resonances can then be identified. Figure 4.8 shows the residual distribution of electrons in the conduction bands after the light-matter interaction as function of the maximal field strength. The distributions are shown for two values of the CEP, $\phi_{\mathrm{CE}} = 0$ and $\phi_{\mathrm{CE}} = \pi/2$, and for both two-band and six-band calculations. For $\varphi_{\mathrm{CE}} = 0$, the k-resolved population is symmetric, so the residual intraband current is close to zero, in accordance with the polar plots shown in Figure 4.5. For $\varphi_{\mathrm{CE}} = \pi/2$, the residual conduction-band population becomes highly asymmetric in k in the region $F_0 \gtrsim 0.3$ V/Å and $|k|/k_{\mathrm{max}} \lesssim 0.1$.

The wave packets are easily identified in the two-band calculations, and resonances can also be identified at the Γ-point. It is also evident that a region of strongly nonlinear behavior occurs at $F_0 \gtrsim 0.5$ V/Å. The interplay with intraband motion gives rise to local maxima away from the Γ-point, and such local maxima are clearly present in Figure 4.8 (a) and (b) where $\varphi_{\mathrm{CE}} = 0$ and $\varphi_{\mathrm{CE}} = \pi/2$ respectively. In the last row, Figure 4.8 (c), the carrier-envelope phase is also $\varphi_{\mathrm{CE}} = \pi/2$, but the term that gives rise to intraband motion was excluded from the equation of motion. Omitting the intraband motion modified the dynamics significantly, and the residual distribution changes from asymmetric to symmetric, which causes the residual current to vanish. The location of those local maxima can be related to two-photon resonances. From Eq. (4.28), the two-photon resonance condition for an electron in a parabolic band would be $E_g + U_p = 2\hbar\omega_0$, where $U_p = e^2F_0^2/(4\mu\omega_0^2)$ is known as ponderomotive energy.

For GaAs, the effective mass is $\mu = 0.05m_0$, and accordingly, the two-photon resonance is expected to appear at $F_0 = 0.3$ V/Å for transitions from the light-hole band to the lowest conduction band. Calculations that take the non-parabolicity into account calculation yields $F_0 = 0.5$ V/Å, which is in agreement with the observation in Figure 4.8. The location of these resonances in reciprocal space shift to larger values of $|k|$ as the field strength increases.

Figure 4.9 shows the result of two-band calculations where the interband dynamics has been modified by reducing the dipole matrix elements by a factor of 10 in all three plots, and where the intraband term has been omitted for the results in in the last row. This is an attempt to disentangle intraband motion from Rabi oscillations. In the absence of detuning, this would decrease the Rabi frequency by the same factor. Intraband motion causes a large time-dependent detuning enabling interference effects that strongly resemble Rabi flopping, as one can see in Figure 4.9. There are indeed no signatures of Rabi oscillations if there is no intraband motion. However, in panels (a) and (b), periodic local minima of the conduction-band population occur at $k = 0$. The field strengths at which these minima occur are slightly larger than those in Figure 4.8.

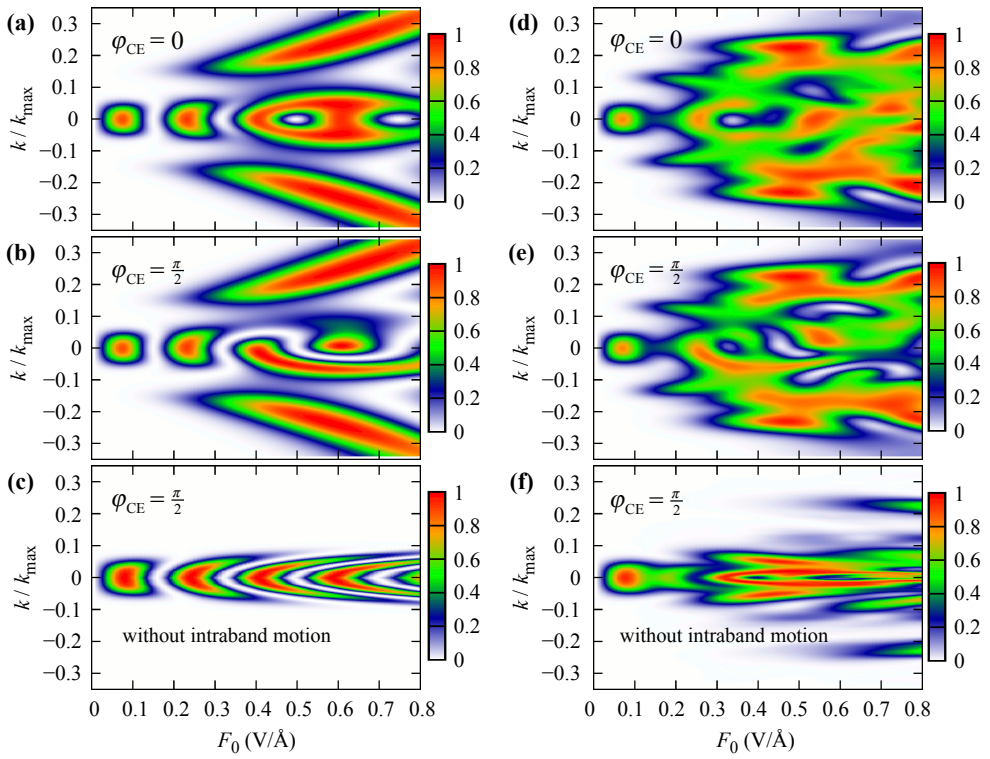

Figure 4.8: The residual population of the lowest conduction band $n_{c_1}(k, t_{max})$ in simulations with two (a)–(c) and six (d)–(f) bands without dephasing ($T_2 = \infty$). The CEP of the laser pulse is $\varphi_{CE} = 0$ in panels (a), (d) and $\pi/2$ in the other plots. Panels (c), (f) display population distributions obtained without intraband motion.

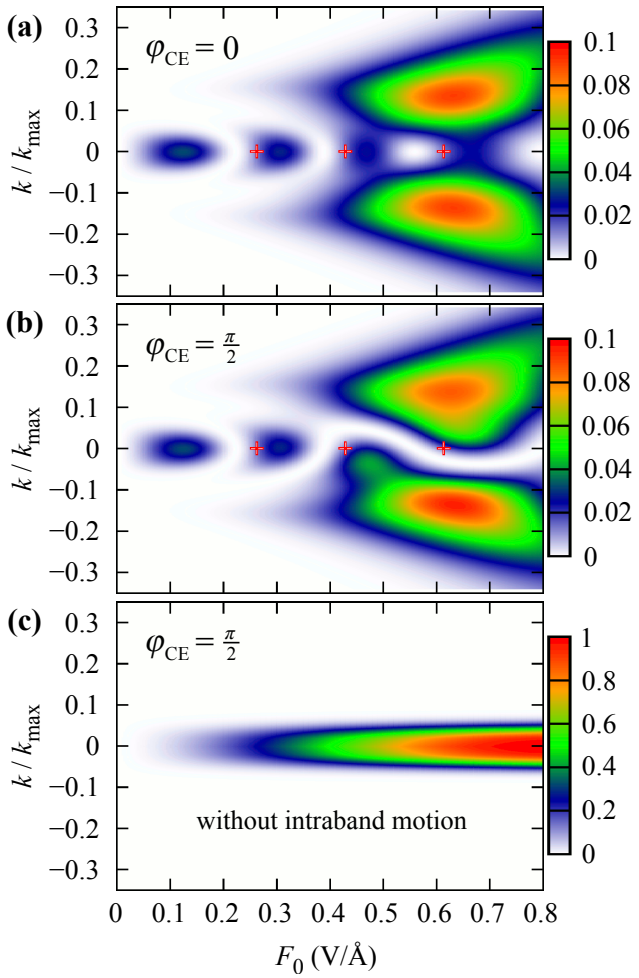

Figure 4.9: The same as Figure 4.8, but all the transition matrix elements are reduced by a factor of 10 in order to suppress Rabi oscillations. The red crosses indicate the peak field strengths where the pulse area $\mathcal{A}$ [see Eqs. (1.43)] is an integer multiple of 2π. Due to reduced excitation probabilities, panels (a) and (b) use a different color scale.

4.6 Conclusion

The work presented in this chapter was motivated by the hypothesis that carrier-wave Rabi flopping of electrons could be used to optically control currents in semiconductors. Numerical simulations instead indicated the existence of a novel regime of field-induced electron dynamics. The transfer of population between valence bands and conduction bands was seen to change from well-known Rabi oscillations at low field strength to intraband-assisted resonances at high field strengths. The effect of intraband motion could be interpreted in terms of a combination of a time-dependent modulation of the energy and a time-dependent modulation of the dipole moment. The former effect opens up multi-photon pathways, and occurs in materials where the band widths are larger than then excitation frequency, while the latter effect is important when the dipole moments are strongly peaked in the Brillouin zone. The effects are expected to be important to semiconductors in general, but only the former effect is expected to also be important for wide band gap insulators.

For GaAs, the two effects manifested themselves through a pronounced kick-like excitation mechanism. This dynamics was denoted "kicked anharmonic Rabi oscillations" when introduced in Wismer et al. [141]. It has later been observed experimentally that intraband motion indeed enhances injection of valence band electrons to the conduction band in GaAs [104].

Consequently, intraband motion enhances the sensitivity of optically induced currents to the carrier-envelope phase of few-cycle pulses. Such observations have also later been reported in experiments on the semi-metal graphene [51].

Finally, the numerical results presented here also demonstrate the time dependence of the lowest conduction band population for selected reciprocal-space pathways, and how they undergo very rapid changes at the moments of the kicks. These predicted effects are also expected to be experimentally observable as the asymmetric momentum distribution can be directly observed using angular resolved photoemission spectroscopy (ARPES) [26, 81, 47, 70], and the residual current can be detected through accompanying terahertz radiation [24, 67, 117].

Chapter 5

Optical Faraday effect in dielectrics

When an electromagnetic pulse propagates inside a polarizable medium subject to a static magnetic field that is parallel to the direction of propagation of the pulse, the plane of the polarization rotates over the course of propagation. This is known as the Faraday effect. The rate of rotation is proportional to the magnetic field strength, and the proportionality constant depends on the material and is known as the Verdet constant. Rotation of the polarization vector also occurs for pulses propagating through an optically active medium where the chiral symmetry is broken at the microscopic level. In this chapter, the effect of transient chirality induced in solid media by a strong, circularly polarized pulses is investigated. If a linearly polarized probe pulse co-propagates along the circularly polarized pulse, the transiently induced chirality can cause a rotation of the polarization vector of the probe pulse even if the medium is isotropic. This effect is known as the optical Faraday effect [5, 93, 94], and the purpose of the medium is to enable non-linear interactions between the photons from the two pulses. If the circular field also modifies the absorption of the medium, it will also affect the ellipticity of the probe pulse.

This class of phenomena was first discovered in atomic vapors [3, 73, 122]. In those measurements, the frequencies of a circularly polarized pump pulse and a linearly polarized probe pulses were tuned to atomic transitions in order to enhance the nonlinear interaction. For solid media it may be more relevant to investigate the dynamics for pulses with a central frequency which is only a fraction of the band gap as transparent materials have a higher damage threshold. In addition, light-induced ellipticity and polarization rotation were investigated for solids in the parametric and non-parametric cases, where the medium was transparent to either both laser pulses [27, 94] or just the pump pulse [96, 120].

The magnitude of the optical Faraday effect depends on the electric field amplitude, and the nonlinear effect is expected to become particularly significant for intensities that are currently available for few-cycle laser pulses [107, 115].

5.1 Third order response for a pump-probe set-up

The field of an electromagnetic pulse can be decomposed into a superposition of plane waves, and it is instructive to first consider the polarization response to spatially homogeneous plane waves

$$\mathbf{F}(z,t) = F_0 \int_{-\infty}^{\infty} d\omega\ \tilde{f}(\omega, z) e^{i\omega t}. \tag{5.1}$$

Even when the dynamics in the medium is highly nonlinear, the linear and lowest order nonlinearities are expected to have the highest intensities. The non-linear response is then dominated by the perturbative third-order response for materials when the second order non-linearity vanishes due to inversion symmetry. The goal of this chapter is to examine the electron dynamics in response to a linearly polarized probe pulse and a circularly polarized pump pulse. The probe pulse is taken to be sufficiently weak such that all terms that are non-linear in the probe field can be neglected. Sapphire is a uniaxial crystal with a threefold symmetry along the optic axis and belongs to the space group ($\bar{3}2/\mathrm{m}$). If a laser pulse propagates along the optic axis of sapphire the polarization response in the plane normal to the propagation axis will therefore be isotropic.

When analyzing the third-order polarization response it is instructive to decompose the electric field into circular components $\mathbf{F}(t) = \mathbf{F}_+(t) + \mathbf{F}_-(t)$. Each component is composed of photons with opposite spin vectors $\mathbf{S}$. The spin which will later be helpful for understanding the dynamics. Likewise, the polarization response can also be decomposed into a left-rotating and right-rotating component $\mathbf{P}(t) = \mathbf{P}_+(t) + \mathbf{P}_-(t)$. In addition, the origin of the left-rotating and right-rotating components can be traced to either of the two circular components of the electric field. Consequently, the polarization response can be divided into four components $\mathbf{P}_{\pm}^{(\pm)}$, where the superscript refers to the helicity of the electric field component that caused it.

The pump pulse is taken to be an intense, circularly polarized, infrared pulse and the probe pulse is taken to be a weak linearly polarized ultraviolet pulse. The term 'pump' refers to the pulse being sufficiently intense to induce a strong, nonlinear response, it does not necessarily indicate that a significant fraction of electrons are excited to the conduction band. The central frequencies of the pulses are also taken to be sufficiently far apart in order to minimize the spectral overlap of the pulses, such that their contributions to the non-linear response are easily distinguished.
As the pulses propagate in the medium, the third-order non-linearity leads to four-wave mixing. Only those components that contain the UV field to first order are, however, of interest for the optical Faraday effect. As sapphire has a three-fold symmetry around the optic axis, the generation of third-order circular harmonics are forbidden. Choosing $\omega_{\mathrm{UV}} = 3\omega_{\mathrm{IR}}$ thereby ensures that all measurable responses at the UV-frequency orthogonal to the probe pulse are due to the nonlinear interaction between the pulses.

Perturbation theory can by used to estimate the time-frequency response of the solid,

from which the magnitude and helicity at selected frequencies can be calculated [19]. The third-order polarization response is then

$$P_i(\omega_a+\omega_b+\omega_c)=\epsilon_0\sum_{jkl}\sum_{P(a,b,c)}\chi_{ijkl}(\omega_a+\omega_b+\omega_c;\omega_a,\omega_b,\omega_c)E_j(\omega_a)E_k(\omega_b)E_l(\omega_c), \quad (5.2)$$

where $P(a,b,c)$ refers to all permutations over the indices a,b, and c. The envelopes of the fields are f^{IR} and f^{UV} respectively, and the helicity of the pump pulse is taken to be positive. If the envelopes are sufficiently long and vary slowly, the two newly generated frequencies $\omega_{\mathrm{UV}}+2\omega_{\mathrm{IR}}$ and $\omega_{\mathrm{UV}}-2\omega_{\mathrm{IR}}>0$ will be the only non-vanishing contributions:

$$P_+^{(-)}(t;\omega_{\mathrm{UV}}+2\omega_{\mathrm{IR}})=\alpha(t)\chi^{(3)}_{2211}(\omega_{\mathrm{UV}}+2\omega_{\mathrm{IR}};\omega_{\mathrm{IR}},\omega_{\mathrm{IR}},\omega_{\mathrm{UV}})+\text{c.c.} \quad (5.3)$$

$$P_-^{(+)}(t;\omega_{\mathrm{UV}}-2\omega_{\mathrm{IR}})=\alpha(t)\chi^{(3)}_{2211}(\omega_{\mathrm{UV}}-2\omega_{\mathrm{IR}};-\omega_{\mathrm{IR}},-\omega_{\mathrm{IR}},\omega_{\mathrm{UV}})+\text{c.c.} \quad (5.4)$$

where $\alpha=12\sqrt{2}\epsilon_0\left[f^{\mathrm{IR}}(t)\right]^2 f^{\mathrm{UV}}(t)F_{\mathrm{IR}}^2F_{\mathrm{UV}}$. Due to conservation of energy, momentum and spin, the light generated at the frequency $\omega_{\mathrm{UV}}+2\omega_{\mathrm{IR}}$ has a positive helicity due to the absorption of one UV photon with negative helicity and two IR photons of positive helicity. Similarly, light generated at a frequency of $\omega_{\mathrm{UV}}-2\omega_{\mathrm{IR}}$ is due to the absorption of one UV photon with negative helicity and the emission of two IR photons At the UV frequency, both helicities are permitted, but the helicity of the emitted light is the same as that of the UV-photon that was involved in the process:.

$$P_+^{(+)}(t;\omega_{\mathrm{UV}})=\alpha(t)\Big[\chi^{(3)}_{1111}(\omega_{\mathrm{UV}};-\omega_{\mathrm{IR}},\omega_{\mathrm{IR}},\omega_{\mathrm{UV}})-\quad\chi^{(3)}_{2211}(\omega_{\mathrm{UV}};-\omega_{\mathrm{IR}},\omega_{\mathrm{IR}},\omega_{\mathrm{UV}})\Big]+\text{c.c.} \quad (5.5)$$

$$P_-^{(-)}(t;\omega_{\mathrm{UV}})=\alpha(t)\Big[\chi^{(3)}_{1111}(\omega_{\mathrm{UV}};-\omega_{\mathrm{IR}},\omega_{\mathrm{IR}},\omega_{\mathrm{UV}})-\quad\chi^{(3)}_{2211}(\omega_{\mathrm{UV}};\omega_{\mathrm{IR}},-\omega_{\mathrm{IR}},\omega_{\mathrm{UV}})\Big]+\text{c.c.} \quad (5.6)$$

5.2 Electromagnetic propagation

In order to account for the light-matter interaction it is necessary to also consider Maxwell's equations, which govern the propagation and time evolution of electromagnetic fields:

$$\nabla \cdot \mathbf{F} = \frac{\rho}{\epsilon_0} \qquad \nabla \times \mathbf{F} = -\frac{d\mathbf{B}}{dt} \tag{5.7}$$

$$\nabla \cdot \mathbf{B} = 0 \qquad \nabla \times \mathbf{B} = \mu_0 \mathbf{J} + \mu_0 \epsilon_0 \frac{d\mathbf{F}}{dt} \tag{5.8}$$

Assuming that $\nabla(\nabla \cdot \mathbf{E}) \approx 0$, which is a common approximation, the propagation of electric fields depend on the polarization response of the medium:

$$\nabla^2 \mathbf{F} = \mu_0 \frac{\partial \mathbf{J}}{\partial t} + \epsilon_0 \mu_0 \frac{\partial^2 \mathbf{F}}{\partial t^2}, \tag{5.9}$$

or alternatively:

$$\nabla^2 \mathbf{F} - \frac{1}{\epsilon_0 c^2} \frac{\partial^2}{\partial t^2} \left(\mathbf{D}^{(1)} \right) = \frac{1}{\epsilon_0 c^2} \frac{\partial^2 \mathbf{P}^{\mathrm{NL}}}{\partial t^2}, \tag{5.10}$$

where $\mathbf{D}(t) = \mathbf{P}(t) + \epsilon_0 \mathbf{F}(t) = \int_{-\infty}^{t} \mathbf{J}(t')\, dt' + \epsilon_0 \mathbf{F}(t)$ is the displacement field, $\mathbf{D}^{(1)} = \boldsymbol{\epsilon}\mathbf{F} = \epsilon_0(\mathbf{1} + \boldsymbol{\chi})\mathbf{F}$ is the displacement field to first order in the electric field, and $\mathbf{P}^{\mathrm{NL}} = \mathbf{P} - \epsilon_0 \boldsymbol{\chi}\mathbf{F}$ is the total polarization less the first order response. This form is convenient when parameterizing the propagation dynamics in terms of a refractive index.
If a uniform, static magnetic field is applied, a Drude-like response can be determined, by treating electrons as classical particles, and solving the Newtonian equations of motion. This leads to a polarization response orthogonal to the electric field due to the Lorentz force [22]. The dielectric tensor is then modified by the applied magnetic field. If the magnetic field is applied along the z-axis of an uniaxial medium, the dielectric tensor becomes a Hermitian matrix:

$$\boldsymbol{\epsilon} = \begin{pmatrix} \epsilon_{xx} & \epsilon_{xy} & 0 \\ \epsilon_{yx} & \epsilon_{yy} & 0 \\ 0 & 0 & \epsilon_{zz} \end{pmatrix} \tag{5.11}$$

For non-Hermitian tensors the eigenvalues can be complex with the absorption rate being proportional to the imaginary part of the eigenvalues. If the diagonal elements $\epsilon_{xx} = \epsilon_{yy}$ are real and the off-diagonal elements $\epsilon_{xy} = \epsilon_{yx}^*$ are purely imaginary, the eigenvectors are $v_1 = (1, i, 0)$ and $v_2 = (1, -i, 0)$, which corresponds to the polarization vectors of circularly polarized light. Light with the polarization vector v_1 experiences a dielectric constant of $\epsilon_{xx} - |\epsilon_{xy}|$ while light with the vector $v_2 = (1, -i, 0)$ experiences a dielectric constant of $\epsilon_{xx} + |\epsilon_{xy}|$. The right- and left-handed components therefore propagate at different rates, and the plane of polarization of a linearly or elliptically polarized pulse containing will therefore rotate. Since dispersion is related to absorption via the Kramers-Kronig relations, the absorption is finite, however small, for all frequencies. If one of the helical components is absorbed more efficiently than the other, the superposition is no longer balanced, and the initially linearly polarized field turns elliptical as it propagates through

the medium.

The purpose of applying a strong, circularly polarized pulse is to modulate the dielectric tensor in a similar manner in the absence of static magnetic fields. The propagation of the spectral components of the UV-pulse therefore gets modulated by the IR-pulse via the dielectric constant:

$$\mathbf{D}^{(1)}_{\mathrm{UV}}(\omega,\tau) = \boldsymbol{\epsilon}[\mathbf{F}_{\mathrm{IR}}](\omega,\tau)\mathbf{F}_{\mathrm{UV}}(\omega), \tag{5.12}$$

where τ is the delay between the pulses.
Instead of evaluating $\boldsymbol{\epsilon}[\mathbf{F}_{\mathrm{IR}}]\mathbf{F}_{\mathrm{UV}}$ directly, the quantum mechanical equations of motion for the electrons in the medium are solved, and the polarization response is used to evaluate the rate of rotation and the rate of induced ellipticity. In order to evaluate these rates, it is necessary to model the propagation of the pulse. To this end, the first-order propagation equation in the slowly-evolving wave approximation can be applied [20]:

$$\frac{\partial \mathbf{F}}{\partial z} = \mathrm{i}k(\omega)\mathbf{F}(z,\omega) + \frac{2\pi\mathrm{i}\omega}{cn(\omega)}\mathbf{P}^{\mathrm{NL}}(z,\omega), \tag{5.13}$$

where the wave vector for propagation along the crystal axis is given by $k(\omega) = \omega/n(\omega)$, and $n(\omega) = \sqrt{1+4\pi\chi^{(1)}(\omega)}$ is the refractive index. Note that this equation and the remaining equation in this chapter are expressed in cgs units in order to be in line with [144]. When the probe pulse propagates through the medium while the pump pulse is present, both the plane of polarization and the ellipticity changes. To investigate how the polarization of the probe pulse changes during the propagation along the z axis, the polarization angle $\theta(\omega,z)$ and ellipticity $\epsilon(\omega,z) = \tan\alpha(\omega,z)$ are defined in the frequency domain via

$$\frac{\left(F_x^{\mathrm{UV}}\right)^* F_y^{\mathrm{UV}}}{\left|F_x^{\mathrm{UV}}\right|^2 + \left|F_y^{\mathrm{UV}}\right|^2} = \frac{\cos\big(2\alpha\big)\sin\big(2\theta\big) + \mathrm{i}\sin\big(2\alpha\big)}{2}. \tag{5.14}$$

Separating the equation into real and imaginary parts yield two equations that can be solved for θ and α:

$$\alpha(\omega,z) = \frac{1}{2}\arcsin\left(\frac{2\mathrm{Im}\left[\left(F_x^{\mathrm{UV}}(\omega,z)\right)^* F_y^{\mathrm{UV}}(\omega,z)\right]}{|\mathbf{F}^{\mathrm{UV}}(\omega,z)|^2}\right), \tag{5.15}$$

$$\theta(\omega,z) = \frac{1}{2}\arcsin\left(\frac{2\mathrm{Re}\left[\left(F_x^{\mathrm{UV}}(\omega,z)\right)^* F_y^{\mathrm{UV}}(\omega,z)\right]}{|\mathbf{F}^{\mathrm{UV}}(\omega,z)|^2\cos\big(2\alpha(\omega,z)\big)}\right). \tag{5.16}$$

For a probe pulse initially polarized along the x axis, the first-order propagation equation is used to express the rate of change in terms of the polarization response. This yields the following expressions:

$$\left(\frac{\partial\theta}{\partial z} + \mathrm{i}\frac{\partial\epsilon}{\partial z}\right)\bigg|_{z=0} = \frac{\partial}{\partial z}\left(\frac{\left(F_x^{\mathrm{UV}}\right)^* F_y^{\mathrm{UV}}}{\left|\mathbf{F}^{\mathrm{UV}}\right|^2}\right)\bigg|_{z=0} = \frac{2\pi\mathrm{i}\omega\left(F_x^{\mathrm{UV}}(\omega,0)\right)^* P_y(\omega,0)}{cn(\omega)\left|F_x^{\mathrm{UV}}(\omega,0)\right|^2}. \tag{5.17}$$

where the following boundary conditions have been applied:

$$\left.\frac{\partial F_x^{\mathrm{UV}}}{\partial z}\right|_{z=0} = \mathrm{i}k(\omega)F_x^{\mathrm{UV}}(0,\omega) \quad , \quad \left.\frac{\partial F_y^{\mathrm{UV}}}{\partial z}\right|_{z=0} = \frac{2\pi\mathrm{i}\omega}{cn(\omega)}P_y^{\mathrm{NL}}(0,\omega)$$
$$\left.\frac{\partial \alpha}{\partial z}\right|_{z=0} = \left.\frac{\partial \epsilon}{\partial z}\right|_{z=0} \quad , \quad \left.\frac{\partial \left|\mathbf{F}^{\mathrm{UV}}\right|^2}{\partial z}\right|_{z=0} = -\frac{2\omega}{c}\left|F_x^{\mathrm{UV}}(0,\omega)\right|^2 \mathrm{Im}[n(\omega)], \quad (5.18)$$

and linear absorption has been neglected by setting $\mathrm{Im}[n(\omega)] = 0$.

Equation 5.17 allows for determining the rate at which the polarization plane of the probe pulse rotates and the change in ellipticity once the polarization response is know. The next step is to determine the polarization by relating it to the susceptibilities, which makes the analysis tractable. The perturbative polarization response can be expressed in terms of effective susceptibilities for weak to moderate fields. The response to each circularly polarized component of the probe pulse, $P_\pm(t,\omega_{\mathrm{UV}}) = \chi_\pm^{\mathrm{eff}} f_\pm^{\mathrm{UV}}(t) F_0^{\mathrm{UV}}$, is then

$$\begin{aligned}\chi_\pm^{\mathrm{eff}} &= \chi^{(1)} + \Delta\chi_\pm \\ &= \chi^{(1)} + 12F_{\mathrm{IR}}^2\left[\chi^{(3)}_{1111}(\omega_{\mathrm{UV}};-\omega_{\mathrm{IR}},\omega_{\mathrm{IR}},\omega_{\mathrm{UV}}) - \chi^{(3)}_{2211}(\omega_{\mathrm{UV}};\mp\omega_{\mathrm{IR}},\pm\omega_{\mathrm{IR}},\omega_{\mathrm{UV}})\right]. \quad (5.19)\end{aligned}$$

As long as the effective susceptibilities provide a good approximation for the nonlinear polarization at the UV frequency, Eq. 5.17 can be used to obtain the following expression for the polarization rotation in an isotropic medium:

$$\frac{d\theta(z,\omega_{\mathrm{UV}})}{dz} = \frac{2\pi\omega_{\mathrm{UV}}}{c}\mathrm{Re}\left[\frac{\Delta\chi_- - \Delta\chi_+}{n(\omega_{\mathrm{UV}})}\right]. \quad (5.20)$$

Thus, it is seen that the optical Faraday effect emerges if $\Delta\chi_- \neq \Delta\chi_+$. This translates into the following condition for the third-order susceptibility components:

$$\chi^{(3)}_{2211}(\omega_{\mathrm{UV}};\omega_{\mathrm{IR}},-\omega_{\mathrm{IR}},\omega_{\mathrm{UV}}) \neq \chi^{(3)}_{2211}(\omega_{\mathrm{UV}};-\omega_{\mathrm{IR}},\omega_{\mathrm{IR}},\omega_{\mathrm{UV}}). \quad (5.21)$$

5.3 Optical Faraday effect in Al_2O_3

Having described the optical Faraday effect in terms of susceptibilities, the next step is to consider a quantum mechanical numerical simulation of the transient chirality induced by an intense, few-cycle, infrared pulse. Short pulses are considered as they allow for high field strengths while keeping the laser fluence below the damage threshold, and thereby prevent causing structural changes to the crystal. The pulses are taken to propagate along the optic axis. In this geometry, the linear optical properties of the crystal are effectively isotropic. The induced optical Faraday effect is probed by a linearly polarized ultraviolet (UV) pulse that is significantly shorter than the pump pulse, but not necessarily shorter than its optical cycle. To obtain the polarization response, the electron dynamics is simulated in three spatial dimensions. As in the previous chapters, the wave functions are expressed and in the basis of stationary Bloch states, and the external field is given in the velocity gauge. Within the dipole approximation, the equation of motion for the wave functions are:

$$\mathrm{i}\hbar\frac{d}{dt}|u_{n\mathbf{k}}\rangle = \hat{H}^0_{\mathbf{k}} + \frac{e^2}{2m}A^2(t) + \frac{e}{m}\mathbf{A}(t)\cdot\hat{\mathbf{p}}_{\mathbf{k}}|u_{n\mathbf{k}}\rangle. \tag{5.22}$$

The electric field $\mathbf{F}(t)$ enters the equation via $\mathbf{A}(t) = -\int_{-\infty}^{t}\mathbf{F}(t')\,dt'$, $e > 0$ is the elementary charge, and m is electron mass. The unperturbed Hamiltonian $H^0_{\mathbf{k}}$ contains 36 valence bands and 160 conduction band that were obtained according to density functional theory using Wien2k [110] for Al_2O_3. The momentum matrix elements, $\hat{\mathbf{p}}_{\mathbf{k}}$, were likewise obtained from Wien2k. The modified Becke-Johnson exchange-correlation potential is used, and leads to a band gap of $E_g = 8.8$ eV, in agreement with experimental observations [89]. The electrons initially reside in the ground state, meaning that the valence bands are fully occupied, while the conduction bands are empty. The polarization response, $\mathbf{P}(t)$ is calculated by solving Eq. (5.22), evaluating the electric current density, $\mathbf{J}(t)$, and integrating it with respect to time: $\mathbf{P}(t) = \int_{-\infty}^{t}\mathbf{J}(t')\,dt'$. Each Cartesian component, $\ell \in \{x, y, z\}$ of the current density is evaluated as

$$J_\ell(t) = -\frac{2e}{m}\left(\frac{e\mathcal{N}_\ell}{V_{\mathrm{cell}}}A_\ell(t) + \sum_n^{N_V}\int_{\mathrm{BZ}}\frac{d^3k}{(2\pi)^3}\,\langle u_{n\mathbf{k}}(t)|\hat{p}_{\ell,\mathbf{k}}|u_{n\mathbf{k}}(t)\rangle\right), \tag{5.23}$$

where V_{cell} is the unit-cell volume, and $\mathcal{N}_\ell$ is the first order-approximation for the adiabatic corrections introduced in Section 3.4. The pre-factor of 2 comes from the fact that each band is doubly occupied due to the spin degeneracy of electrons. The lattice constants for Al_2O_3 are obtained from [136]. The density-functional-theory and dynamical calculations were performed on an unshifted Monkhorst-Pack grid with $5 \times 5 \times 5$ $\mathbf{k}$-points.

The electric fields of the pulses are defined in terms of the vector potential

$$\mathbf{A}^{\mathrm{P}}(t) = F_{\mathrm{P}}\omega_{\mathrm{P}}^{-1} \exp\left(\frac{-2\ln(2)t^2}{(T_{\mathrm{FWHM}}^{\mathrm{P}})^2}\right) \mathrm{Re}\left[\mathrm{i}e^{-\mathrm{i}\omega_{\mathrm{P}}t}\mathbf{u}_{\mathrm{P}}\right], \tag{5.24}$$

$$\mathbf{F}^{\mathrm{P}}(t) = -d\mathbf{A}^{\mathrm{P}}/dt = \mathrm{Re}\left[f^{\mathrm{P}}(t)e^{-\mathrm{i}\omega_{\mathrm{P}}t}\mathbf{u}_{\mathrm{P}}\right]. \tag{5.25}$$

Here, $\mathrm{P} \in \{\mathrm{IR}, \mathrm{UV}\}$, F_{P} is the amplitude of the electric field, $T_{\mathrm{FWHM}}^{\mathrm{P}}$ is the full width at half maximum of the pulse intensity, and the central pulse frequency is related to its central wavelength via $\omega_{\mathrm{P}} = 2\pi c/\lambda_{\mathrm{P}}$.
For the circularly polarized IR pump pulse, $\lambda_{\mathrm{IR}} = 750\mathrm{nm}$, $\mathbf{u}_{\mathrm{IR}} = (1, \mathrm{i}, 0)$, and $T_{\mathrm{IR}} = 5$ fs. For the linearly polarized UV probe pulse, $\lambda_{\mathrm{UV}} = 250\mathrm{nm}$, $\mathbf{u}_{\mathrm{UV}} = (1, 0, 0)$, $T_{\mathrm{UV}} = 2.5$ fs, and the peak field strength is kept fixed at $F_{\mathrm{UV}} = 1\,\mathrm{mV/Å}$. To model pump-probe measurements, a delay τ is introduced, and the fields are thus given by $\mathbf{F}^{\mathrm{IR}}(t)$ and $\mathbf{F}^{\mathrm{UV}}(t-\tau)$. Fresnel's formula is used to obtain an approximate relation between the field amplitude in vacuum and the field amplitude inside the medium:

$$F_{\mathrm{P}}^{\mathrm{vac}} = \frac{1}{2}[1 + n(\omega_{\mathrm{P}})]F_{\mathrm{P}}. \tag{5.26}$$

Fresnel's formula is derived for plane waves and therefore only provide an approximate description for the transmission of short pulses.

A fourth-order Runge–Kutta scheme is used to solve Eq. (5.22) for all 36 valence bands and 160 conduction bands in the interaction picture. Thus, $36 \times 5 \times 5 \times 5 = 4500$ independent differential equations are solved, and each of them was solved in a basis of $36 + 160 = 196$ stationary states. On a desktop computer (Intel Core 2 Duo E8400 3.00 GHz), solving the time-dependent Schrödinger equation for a single $\mathbf{k}$ point and a particular initial valence state takes 12 seconds.

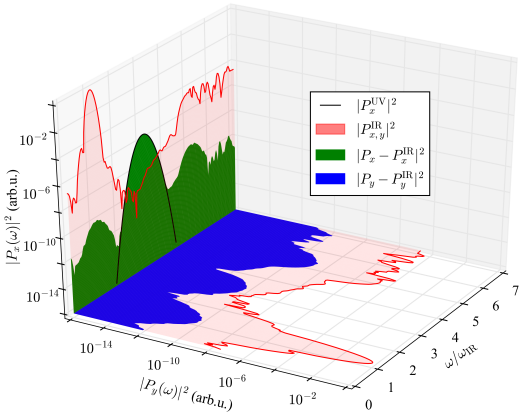

Figure 5.1: The spectral analysis of the polarization response for $F_{\mathrm{IR}} = 1$ V/Å and the zero pump-probe delay. The x and y components of the IR-only response $\mathbf{P}^{\mathrm{IR}}$ (pale red), the UV-only response $\mathbf{P}^{\mathrm{UV}}$ (black curve), and the polarization induced by both pulses after subtracting the IR-only response: $\mathbf{P} - \mathbf{P}^{\mathrm{IR}}$ (the green and blue areas). All the curves are plotted on the same scale.

5.4 Intensity dependence of the optical Faraday effect

First it is shown how the optical Faraday effect depends on the strength of the IR field. The two pulses are taken to arrive simultaneously, i.e. $\tau = 0$. Based on the considerations up until now, the third order non-linear response is expected to dominate the response for weak fields. Instead of calculating the response perturbatively, the response $\mathbf{P}^{\mathrm{IR}}(t)$ is first calculated to a single IR pulse, and afterwards the response $\mathbf{P}(t)$to both the IR pulse and the UV pulse is calculated. Afterwards, the response for the single IR pulse alone is subtracted. As the UV pulse is very weak, the UV pulse can be considered a perturbation, from which the response to this particular perturbation can be calculated. The power spectra of the polarizations $\mathbf{P}^{\mathrm{IR}}(t)$, $\mathbf{P}^{\mathrm{UV}}(t)$ and $\mathbf{P}(t) - \mathbf{P}^{\mathrm{IR}}(t)$ are shown in Figure 5.1. The field strength is taken to be in the strong, nonlinear regime $F_{\mathrm{IR}} = 1$ V/Å where the third-order susceptibilities no longer provide an accurate description of the optical Faraday effect. The power spectra of the polarization is shown for both Cartesian components.
The response to a single IR pulse is shown in red, and covers a wide range of frequencies, including above-band gap frequencies which is at $\omega/\omega_{\mathrm{IR}} \gtrsim 5.3$. As expected, the third-order harmonic response is absent due to being forbidden by symmetry. On the other hand, the response to a single UV pulse $\mathbf{P}^{\mathrm{UV}}$ is shown in black, and is a gaussian function which is simply proportional to the spectrum of the UV pulse. This confirms that the field is sufficiently weak that only the first order response is relevant. The green and blue filled areas show $|P_x(\omega) - P_x^{\mathrm{IR}}(\omega)|^2$ and $|P_y(\omega) - P_y^{\mathrm{IR}}(\omega)|^2$ respectively, which are the response of the system consisting of medium and IR pulse to the probe UV pulse.

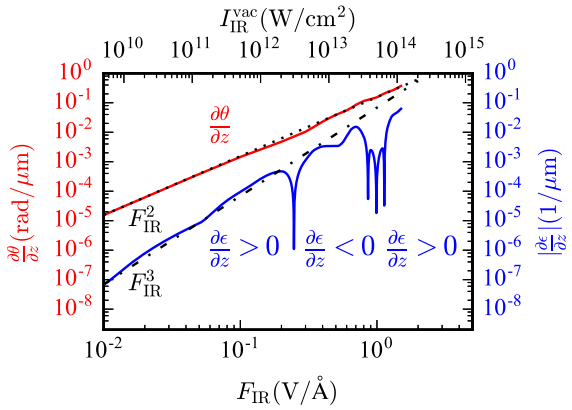

Figure 5.2: The induced polarization rotation and circular dichroism at the central UV frequency for $\tau = 0$. The upper horizontal axis is labeled with peak intensities of the incident IR pulse in vacuum. The lower horizontal axis shows the peak IR field at the crystal surface.

The rate of rotation $\partial\theta/\partial z$ and the rate of change of ellipticity $\partial\epsilon/\partial z$ are shown as functions of the IR field strength in Figure 5.2. The only quantity needed from the polarization responses are $P_y(\omega) - P_y^{\rm IR}(\omega)$ according to Eq. (5.17). The red curve in shows that deviations from the $\partial\theta/\partial z \propto F_{\rm IR}^2$ scaling law are small even at high IR intensities close to the damage threshold of sapphire. For a peak IR intensity of 10^{13} W/cm^2, the induced optical Faraday rotation at the central UV frequency is 0.03 radians (1.7°) per micrometer. Reaching this rotation strength in the conventional Faraday effect would require a magnetic field as strong as 700 Tesla, which exceeds the strongest nondestructive magnetic fields currently available in laboratories. This assumes a Verdet constant of 4 rad/(mT) [137].

In addition to polarization rotation, the UV pulse also experiences IR-induced circular dichroism, which is shown by the blue curve in Figure 5.2. In the weak-field limit, the induced ellipticity per unit propagation length scales as $\partial\epsilon/\partial z \propto F_{\rm IR}^3$ because at least three IR photons must be absorbed in addition to a UV photon to overcome the band gap. At $F_{\rm IR} = 0.25$ V/Å, the induced zero-delay ellipticity changes its sign, which appears as a narrow downward spike on the logarithmic scale. The sign of $\partial\epsilon/\partial z$ is shown in the plot, and it changes its sign four times for the interval of field strength considered here. The ellipticity is therefore seen to be much more sensitive to the actual field strength. The fact that the ellipticity changes sign can make measurements of the circular dichroism difficult, unless the field strength can be controlled over the length of interaction.

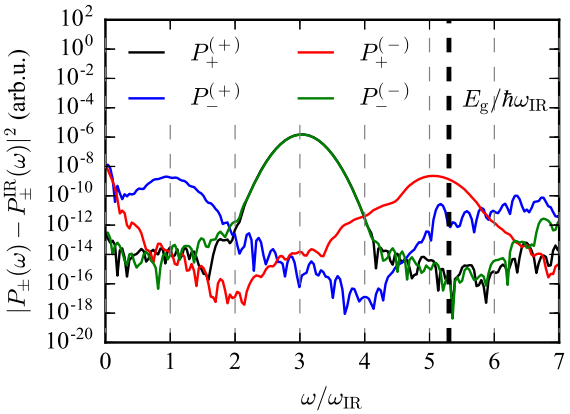

Figure 5.3: The spectral analysis of the polarization response for $F_{\mathrm{IR}} = 1$ V/Å. The decomposition of $\mathbf{P} - \mathbf{P}^{\mathrm{IR}}$ into the left- and right-rotating components induced by the left- and right-rotating components of the UV pulse. The vertical black dashed line shows the position of the band edge.

The difference in polarization $\mathbf{P} - \mathbf{P}^{\mathrm{IR}}$ that is show in Figure 5.1 can be decomposed into the components $P_{\pm}^{(\pm)}$ that were introduced in Section 5.1. The spectra of these components are shown in Figure 5.3. As expected, the responses $P_{+}^{(+)}$ and $P_{-}^{(-)}$ are maximal at the UV frequency, while $P_{+}^{(-)}$ has a local maximum at $\omega_{\mathrm{UV}} + 2\omega_{\mathrm{IR}}$ and $P_{-}^{(+)}$ has a local maximum at $\omega_{\mathrm{UV}} - 2\omega_{\mathrm{IR}}$. This is consistent with expected spin of photons that will be radiated by this polarization. Near the band edge, the conservation of the photon spin is violated because some angular momentum is transferred to charge carriers.

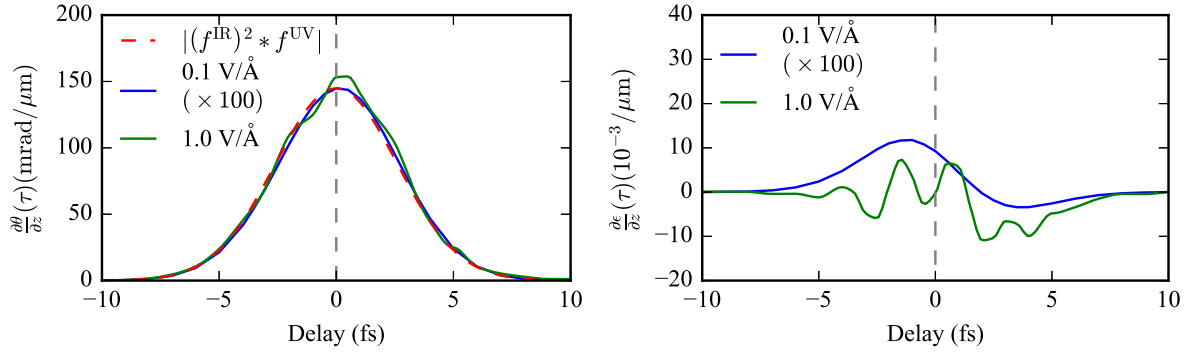

Figure 5.4: The dependence of induced (a) polarization rotation and (b) ellipticity of the probe pulse on the pump-probe delay. For a positive delay, the probe pulse arrives after the pump pulse. In both panels, data for $F_{\mathrm{IR}} = 0.1$ V/Å (blue curves) was multiplied by a factor of 100 to make it comparable to that for $F_{\mathrm{IR}} = 1$ V/Å (green curves). In panel (a), the dashed red curve shows the convolution of the UV envelope and the square of the IR envelope.

5.5 Delay dependence of the optical Faraday effect

Lastly, a delay scan is considered. This is motivated by the non-instantaneous characteristics of the optical Faraday effect, which is a result of the medium being dispersive and nonlinear. The delay-dependence introduces a trivial modulation of intensity. The intensity scans of the previous section therefore serve to determine the trivial intensity-related effects when a delay is introduced.

The results of the delay scan is shown in Figure 5.4 (a), where the polarization rotation is evaluated at the central UV frequency is shown for various delays. At $F_{\mathrm{IR}} = 0.1$ V/Å the conventional perturbative nonlinear optics works well, so the response is expected to depend on the instantaneous intensity, i.e. $\partial\theta/\partial z \propto |\mathbf{F}_{\mathrm{IR}}(t)|^2$. It is confirmed that $\partial\theta/\partial z$ follows the shape of the convolution $\left|\left(f^{\mathrm{IR}}\right)^2 * f^{\mathrm{UV}}\right|$ (red dashed curve) as a function of the delay (blue curve). The convolution $\left|\left(f^{\mathrm{IR}}\right)^2 * f^{\mathrm{UV}}\right|$ shown in the figure has been scaled to have the same peak value and unit to allow for better visual comparison. When the field is increased to $F_{\mathrm{IR}} = 1$ V/Å, a small but significant reshaping of $\partial\theta/\partial z$ is observed. This indicates an onset of nonadiabatic processes that disappear by the end of the pulse. For 1 V/Å the residual excitation density is 2.9×10^{-5} electrons per unit cell. For large delays, the pulses do no overlap, and no rotation of the polarization vector occurs. The induced chirality can therefore be considered transient. It also verifies that the number of excited conduction band electrons is small enough to have a negligible effect on the polarization.

Just as the rate of ellipticity $\partial\epsilon/\partial z$ showed a stronger dependency on the electric field strength than the rate of rotation, the ellipticity also exhibits a stronger dependency on the delay between the two pulses. The rate of ellipticity is shown in Figure 5.4 (b). For weak IR fields, i.e. $F_{\mathrm{IR}} = 0.1$ V/Å, the induced ellipticity is mainly due to the time-dependent polarization rotation as the intensity of the 5-fs IR pulse changes significantly over the duration the 2.5-fs UV pulse. This contribution to the induced ellipticity represents a transfer of angular momentum from the pump pulse to the probe pulse in the absence of circular dichroism, and it is particularly large at delays where $d|f^{\mathrm{IR}}(\tau)|^2/d\tau$ is large. At the same time, even this relatively weak IR field induces some noticeable ellipticity at $\tau = 0$, where $d|f^{\mathrm{IR}}(\tau)|^2/d\tau = 0$, and the main mechanism is therefore the induced circular dichroism.

At $F_{\mathrm{IR}} = 1$ V/Å (green curve), the induced ellipticity exhibits an oscillatory dependence on the pump-probe delay. The period of these oscillations is close to the optical period of the IR field (2.5 fs). Therefore, the oscillations cannot be due to the interference with the $\omega_{\mathrm{UV}} \pm 2\omega_{\mathrm{IR}}$ channels, which would result in a period of $\sim 2\pi/(2\omega_{\mathrm{IR}}) \approx 1.3$ fs. These oscillations represent a strong-field effect, and their phase depends on F_{IR}.

In order to observe these effects experimentally it may be beneficial to use a non-collinear geometry to spatially separate the propagated probe pulse from UV light. As the rates $\partial\theta/\partial z$ and $\partial\epsilon/\partial z$ are calculated using the first order propagation equation the pulses should ideally only propagate through micrometer-thin samples. Because of the high field strength, such widths are expected to be sufficient to measure a noticeable rotation and ellipticity.

5.6 Conclusions

The optical Faraday effect was examined in Al_2O_3 for an infrared pump pulse and an ultraviolet probe pulse. The effect was described in terms of effective susceptibilities, which were determined from real-time calculations of the optical response. In order to examine the associated effects of circular dichroism and transient chirality, the polarization response was decomposed into its helical components. It was observed that the optical Faraday effect can lead to rotations of the plane of polarization up to a few degrees per micrometer for experimentally accessible pulses. In comparison, obtaining the same effect with the ordinary Faraday effect is not easily accessible, as it requires magnetic field strengths of a few hundred teslas.

Even though the optical Faraday effect is a consequence of the nonlinear polarization response being non-instantaneous, the response time appears to be small enough that the optical Faraday effect in the investigated solid is inertialess. This can be observed from the scan over the probe pulse delay. As a result, a very fine control over the temporal profile of the plane of polarization can be achieved with the optical Faraday effect.

For basic research, the ultrafast optical Faraday effect is attractive as a spectroscopic tool capable of studying chiral dynamics with an attosecond temporal resolution. Potential applications of this effect include ultrafast all-optical circular-polarization modulators, optical isolators, and optical circulators without a need for magnetic field.

Chapter 6

Conclusion and outlook

The objectives of this thesis has been to investigate the dynamics of electrons in solids excited by strong electric fields. To this end, simulations of electron dynamics were performed in the independent particle approximations and the time-resolved optical responses were analyzed. The conclusions regarding the methodology used in this thesis can be summarized as follows:

- The electric current obtained from the geometric phases of mixed quantum systems was demonstrated to agree with the electric current determined from the velocity operator. An approximation to the covariant derivative for mixed systems was also determined. It was used to solve the dynamical equations for an open system interacting with the environment in the length gauge.

- The package `ulmic` was designed and implemented. It relies on *ab initio* data, which can be obtained from various existing density functional theory codes. The calculations rely on neglecting the time-dependence of the exchange-correlation potential – an approximation that has later been demonstrated to be justified in the this regime.

- The concept of adiabatic corrections to reduce number of bands required for velocity gauge calculations was introduced. It was tested for wave functions in both one-dimensional periodic potentials and for three-dimensional *ab initio* models for Al_2O_3.

The theoretical work was motivated by recent advances in attosecond spectroscopy, and new regimes for light-matter interaction in solids were investigated. This covers both resonant and non-resonant systems for experimentally accessible pulse parameters, from which it can be concluded that:

- Calculations indicated that unusual microscopic dynamics are expected to occur in direct band gap semiconductors, and that intraband motion is a key quantity to understand these effects. Due to macroscopic responses being averaged over all electrons in the solid, specialized techniques are, however, required to confirm these predictions.

These findings add resonant processes to the toolkit of petahertz solid-state technology where potential applications may range from CEP detection [91] to sub-laser-cycle spectroscopy [58] and ultrafast signal processing [64].

- For wide-band gap insulators, it was found that the optical Faraday effect can be used to rotate the plane of polarization of a probe field much more effectively than through the conventional Faraday effect with experimentally accessible magnetic fields.
  In the investigated regime, it was also found that the response is dominated by the instantaneous response, even for intense infrared pulses reaching field strengths of 1.0 V/Å inside the medium.

The method developed for evaluating the coordinate operator for a mixed system of wave functions in a periodic lattice is very general, and may be applied to other systems, such as optical lattices. In order to take advantage of developments to ab initio calculations beyond density functional theory, it may prove beneficial to extend the work to determine gauge invariant approximations that are compatible with non-local potentials such that screening effects can be incorporated.

Appendix A

Data preservation

Data archive `afs:ipp-garching/mpg/mpq/lap/groupdata/publications`

1. Strong-field resonant

Copy of C++ code.
Copy of Wien2k data.
Copy of analysed results.

2. Ultrafast optical Faraday effect

Copy of Python code.
Copy of Wien2k data.
Copy of analysed results

3. Gauge-independent model

Copy of Python code.
Copy of data for analytical potential.
Copy of analysed results

Bibliography

[1] Ofir E Alon, Vitali Averbukh, and Nimrod Moiseyev. Selection rules for the high harmonic generation spectra. *Physical review letters*, 80(17):3743, 1998.

[2] Claudia Ambrosch-Draxl and Jorge O Sofo. Linear optical properties of solids within the full-potential linearized augmented planewave method. *Computer Physics Communications*, 175(1):1–14, 2006.

[3] V. M. Arutiunian, T. A. Papazian, A. V. Karmenian, S. P. Ishkhanian, and L. Kholts. Resonance rotation of the plane of polarization in potassium vapor. *Z. Eksp. Teor. Fiz.*, 68:44–50, January 1975.

[4] R. Atanasov, A. Haché, J. L. P. Hughes, H. M. van Driel, and J. E. Sipe. Coherent control of photocurrent generation in bulk semiconductors. *Phys. Rev. Lett.*, 76:1703–1706, Mar 1996.

[5] P.W. Atkins and M.H. Miller. Quantum field theory of optical birefringence phenomena. *Mol. Phys.*, 15(5):503–514, 1968.

[6] Claudio Attaccalite and M Grüning. Nonlinear optics from an ab initio approach by means of the dynamical berry phase: Application to second-and third-harmonic generation in semiconductors. *Physical Review B*, 88(23):235113, 2013.

[7] Claudio Attaccalite, M Grüning, and A Marini. Real-time approach to the optical properties of solids and nanostructures: Time-dependent bethe-salpeter equation. *Physical Review B*, 84(24):245110, 2011.

[8] Claudio Aversa and JE Sipe. Nonlinear optical susceptibilities of semiconductors: Results with a length-gauge analysis. *Physical Review B*, 52(20):14636, 1995.

[9] Ph Balcou, Anne L'Huillier, and D Escande. High-order harmonic generation processes in classical and quantum anharmonic oscillators. *Physical Review A*, 53(5):3456, 1996.

[10] P. C. Becker, H. L. Fragnito, C. H. Brito Cruz, R. L. Fork, J. E. Cunningham, J. E. Henry, and C. V. Shank. Femtosecond photon echoes from band-to-band transitions in gaas. *Phys. Rev. Lett.*, 61:1647–1649, Oct 1988.

[11] Kristian Berland and Clas Persson. Enabling accurate first-principle calculations of electronic properties with a corrected k· p scheme. *Computational Materials Science*, 134:17–24, 2017.

[12] George F Bertsch, J-I Iwata, Angel Rubio, and Kazuhiro Yabana. Real-space, real-time method for the dielectric function. *Physical Review B*, 62(12):7998, 2000.

[13] P Blaha, K Schwarz, G Madsen, D Kvasnicka, and J Luits. Wien2k userguide. *Vienna University of Technology, Vienna*, 2001.

[14] Peter Blaha, Karlheinz Schwarz, GKH Madsen, Dieter Kvasnicka, and Joachim Luitz. wien2k. *An augmented plane wave+ local orbitals program for calculating crystal properties*, 2001.

[15] JS Blakemore. Semiconducting and other major properties of gallium arsenide. *J. Appl. Phys.*, 53(10):R123–R181, 1982.

[16] Felix Bloch. Über die quantenmechanik der elektronen in kristallgittern. *Zeitschrift für Physik A Hadrons and Nuclei*, 52(7):555–600, 1929.

[17] Peter E Blöchl. Projector augmented-wave method. *Physical review B*, 50(24):17953, 1994.

[18] EI Blount. Formalisms of band theory. *Solid state physics*, 13:305–373, 1962.

[19] Robert W Boyd. Nonlinear optics. *Elsevier*, 2003.

[20] Thomas Brabec and Ferenc Krausz. Intense few-cycle laser fields: Frontiers of nonlinear optics. *Rev. Mod. Phys.*, 72:545–591, Apr 2000.

[21] Yu. A. Bychkov and A. M. Dykhne. Breakdown in semiconductors in an alternating electric field. *Sov. Phys. JETP*, 31(5):928–32, 1970.

[22] John MD Coey. Magnetism and magnetic materials. *Cambridge University Press*, 2010.

[23] Paul B Corkum. Plasma perspective on strong field multiphoton ionization. *Physical Review Letters*, 71(13):1994, 1993.

[24] D. Côté, J. M. Fraser, M. DeCamp, P. H. Bucksbaum, and H. M. van Driel. Thz emission from coherently controlled photocurrents in gaas. *Appl. Phys. Lett.*, 75(25):3959–3961, 1999.

[25] John Crank and Phyllis Nicolson. A practical method for numerical evaluation of solutions of partial differential equations of the heat-conduction type. In *Mathematical Proceedings of the Cambridge Philosophical Society*, volume 43, pages 50–67. Cambridge University Press, 1947.

[26] A. Damascelli, Z. Hussain, and Z. X. Shen. Angle-resolved photoemission studies of the cuprate superconductors. *Rev. Mod. Phys.*, 75:473–541, 2003.

[27] A. M. Danishevskii, S. F. Kochegarov, and V. K. Subashiev. Light-induced gyrotropy and anisotropy in a cubic crystal. *Sov. J. Exp. Theor. Phys. Lett.*, 33:611, 1981.

[28] Jack Deslippe, Georgy Samsonidze, David A Strubbe, Manish Jain, Marvin L Cohen, and Steven G Louie. Berkeleygw: A massively parallel computer package for the calculation of the quasiparticle and optical properties of materials and nanostructures. *Computer Physics Communications*, 183(6):1269–1289, 2012.

[29] Rainer Dick. Analytic sources of inequivalence of the velocity gauge and length gauge. *Physical Review A*, 94(6):062118, 2016.

[30] H Dixit, R Saniz, Stefaan Cottenier, D Lamoen, and B Partoens. Electronic structure of transparent oxides with the tran–blaha modified becke–johnson potential. *Journal of Physics: Condensed Matter*, 24(20):205503, 2012.

[31] HM Dong, K Han, and W Xu. Dynamic optical properties in graphene: Length versus velocity gauge. *Journal of Applied Physics*, 115(6):063503, 2014.

[32] J e Enkovaara, Carsten Rostgaard, J Jørgen Mortensen, Jingzhe Chen, M Dułak, Lara Ferrighi, Jeppe Gavnholt, Christian Glinsvad, V Haikola, HA Hansen, et al. Electronic structure calculations with gpaw: a real-space implementation of the projector augmented-wave method. *Journal of Physics: Condensed Matter*, 22(25):253202, 2010.

[33] Carlos Fiolhais, Fernando Nogueira, and Miguel AL Marques. *A primer in density functional theory*, volume 620. Springer Science & Business Media, 2003.

[34] Mike Folk, Gerd Heber, Quincey Koziol, Elena Pourmal, and Dana Robinson. An overview of the hdf5 technology suite and its applications. In *Proceedings of the EDBT/ICDT 2011 Workshop on Array Databases*, pages 36–47. ACM, 2011.

[35] T M Fortier, P A Roos, D J Jones, S T Cundiff, R D R Bhat, and J E Sipe. Carrier-envelope phase-controlled quantum interference of injected photocurrents in semiconductors. *Phys. Rev. Lett.*, 92(14):147403, 2004.

[36] Alexander Galstyan, Ochbadrakh Chuluunbaatar, Aliou Hamido, Yu V Popov, Francisca Mota-Furtado, PF O'Mahony, Noël Janssens, Fabrice Catoire, and Bernard Piraux. Reformulation of the strong-field approximation for light-matter interactions. *Physical Review A*, 93(2):023422, 2016.

[37] Lihong Gao, F Lemarchand, and M Lequime. Refractive index determination of sio2 layer in the uv/vis/nir range: spectrophotometric reverse engineering on single and bi-layer designs. *Journal of the European Optical Society-Rapid publications*, 8, 2013.

[38] Crispin Gardiner, Peter Zoller, and Peter Zoller. *Quantum noise: a handbook of Markovian and non-Markovian quantum stochastic methods with applications to quantum optics*, volume 56. Springer Science & Business Media, 2004.

[39] Christopher C Gerry and Edward R Vrscay. Dynamics of pulsed su (1, 1) coherent states. *Physical Review A*, 39(11):5717, 1989.

[40] Shambhu Ghimire, Anthony D. DiChiara, Emily Sistrunk, Pierre Agostini, Louis F. DiMauro, and David A. Reis. Observation of high-order harmonic generation in a bulk crystal. *Nature Physics*, 7(2):138–141, dec 2010.

[41] Shambhu Ghimire, Anthony D. DiChiara, Emily Sistrunk, Pierre Agostini, Louis F. DiMauro, and David A. Reis. Observation of high-order harmonic generation in a bulk crystal. *Nature Phys.*, 7:138–141, Feb 2011.

[42] Shambhu Ghimire, Anthony D DiChiara, Emily Sistrunk, Georges Ndabashimiye, Urszula B Szafruga, Anis Mohammad, Pierre Agostini, Louis F DiMauro, and David A Reis. Generation and propagation of high-order harmonics in crystals. *Physical Review A*, 85(4):043836, 2012.

[43] Paolo Giannozzi, Stefano Baroni, Nicola Bonini, Matteo Calandra, Roberto Car, Carlo Cavazzoni, Davide Ceresoli, Guido L Chiarotti, Matteo Cococcioni, Ismaila Dabo, et al. Quantum espresso: a modular and open-source software project for quantum simulations of materials. *Journal of physics: Condensed matter*, 21(39):395502, 2009.

[44] D Golde, T Meier, and SW Koch. High harmonics generated in semiconductor nanostructures by the coupled dynamics of optical inter-and intraband excitations. *Physical Review B*, 77(7):075330, 2008.

[45] Xavier Gonze, J-M Beuken, R Caracas, F Detraux, M Fuchs, G-M Rignanese, Luc Sindic, Matthieu Verstraete, G Zerah, F Jollet, et al. First-principles computation of material properties: the abinit software project. *Computational Materials Science*, 25(3):478–492, 2002.

[46] Myrta Grüning, Andrea Marini, and Angel Rubio. Density functionals from many-body perturbation theory: The band gap for semiconductors and insulators. *The Journal of chemical physics*, 124(15):154108, 2006.

[47] J. Güdde, M. Rohleder, T. Meier, S. W. Koch, and U. Höfer. Time-resolved investigation of coherently controlled electric currents at a metal surface. *Science*, 318(5854):1287–1291, 2007.

[48] Chihiro Hamaguchi, Masahito Yamaguchi, Hidekazu Nagasawa, Masato Morifuji, Aldo Di Carlo, Peter Vogl, Gerhard Böhm, Günter Tränkle, Günter Weimann, Yuji Nishikawa, et al. Wannier-stark localization in superlattices. *Japanese journal of applied physics*, 34(8S):4519, 1995.

[49] Kenneth K Hansen, Tobias Deffge, and Dieter Bauer. High-order harmonic generation in solid slabs beyond the single-active-electron approximation. *Physical Review A*, 96(5):053418, 2017.

[50] Lars Hedin. New method for calculating the one-particle green's function with application to the electron-gas problem. *Physical Review*, 139(3A):A796, 1965.

[51] Takuya Higuchi, Christian Heide, Konrad Ullmann, Heiko B Weber, and Peter Hommelhoff. Light-field-driven currents in graphene. *Nature*, 550(7675):224–228, 2017.

[52] Pierre Hohenberg and Walter Kohn. Inhomogeneous electron gas. *Physical review*, 136(3B):B864, 1964.

[53] M Hohenleutner, F Langer, O Schubert, M Knorr, U Huttner, S W Koch, M Kira, and R Huber. Real-time observation of interfering crystal electrons in high-harmonic generation. *Nature*, 523(7562):572–5, July 2015.

[54] Li Huang, J Paul Callan, Eli N Glezer, and Eric Mazur. Gaas under intense ultrafast excitation: response of the dielectric function. *Physical Review Letters*, 80(1):185, 1998.

[55] Li Huang, J. Paul Callan, Eli N. Glezer, and Eric Mazur. Gaas under intense ultrafast excitation: Response of the dielectric function. *Phys. Rev. Lett.*, 80:185–188, Jan 1998.

[56] S Hughes. Subfemtosecond soft-x-ray generation from a two-level atom: Extreme carrier-wave rabi flopping. *Physical Review A*, 62(5):055401, 2000.

[57] Mark S Hybertsen and Steven G Louie. Electron correlation in semiconductors and insulators: Band gaps and quasiparticle energies. *Physical Review B*, 34(8):5390, 1986.

[58] Misha Ivanov and Olga Smirnova. Opportunities for sub-laser-cycle spectroscopy in condensed phase. *Chem. Phys.*, 414:3–9, 2013.

[59] L. V. Keldysh. Ionization in the field of a strong electromagnetic wave. *Sov. Phys. JETP*, 20:1307–1314, 1965.

[60] LV Keldysh et al. Ionization in the field of a strong electromagnetic wave. *Sov. Phys. JETP*, 20(5):1307–1314, 1965.

[61] Jacob B Khurgin. Optically induced currents in dielectrics and semiconductors as a nonlinear optical effect. *JOSA B*, 33(7):C1–C9, 2016.

[62] RD King-Smith and David Vanderbilt. Theory of polarization of crystalline solids. *Physical Review B*, 47(3):1651, 1993.

[63] Walter Kohn and Lu Jeu Sham. Self-consistent equations including exchange and correlation effects. *Physical review*, 140(4A):A1133, 1965.

[64] Ferenc Krausz and Mark I Stockman. Attosecond metrology: from electron capture to future signal processing. *Nature Photon.*, 8(3):205–213, 2014.

[65] J. B. Krieger and G. J. Iafrate. Time evolution of Bloch electrons in a homogeneous electric field. *Phys. Rev. B*, 33(8):5494–5500, 1986.

[66] S. Yu. Kruchinin, M. Korbman, and V. S. Yakovlev. Theory of strong-field injection and control of photocurrent in dielectrics and wide band gap semiconductors. *Phys. Rev. B*, 87:115201, Mar 2013.

[67] W. Kuehn, P. Gaal, K. Reimann, M. Woerner, T. Elsaesser, and R. Hey. Terahertz-induced interband tunneling of electrons in gaas. *Phys. Rev. B*, 82:075204, Aug 2010.

[68] Willis E Lamb Jr, Rainer R Schlicher, and Marlan O Scully. Matter-field interaction in atomic physics and quantum optics. *Physical Review A*, 36(6):2763, 1987.

[69] L. D. Landau. On the vibration of the electronic plasma. *Journal of Physics*, 10:25–34, 1946.

[70] W. S. Lee, I. M. Vishik, D. H. Lu, and Z. X. Shen. A brief update of angle-resolved photoemission spectroscopy on a correlated electron system. *J. Phys.: Condensed Matter*, 21:164217, 2009.

[71] Kurt Lejaeghere, Gustav Bihlmayer, Torbjörn Björkman, Peter Blaha, Stefan Blügel, Volker Blum, Damien Caliste, Ivano E Castelli, Stewart J Clark, Andrea Dal Corso, et al. Reproducibility in density functional theory calculations of solids. *Science*, 351(6280):aad3000, 2016.

[72] Xia Leng, Fan Jin, Min Wei, and Yuchen Ma. Gw method and bethe–salpeter equation for calculating electronic excitations. *Wiley Interdisciplinary Reviews: Computational Molecular Science*, 6(5):532–550, 2016.

[73] P. F. Liao and G. C. Bjorklund. Polarization rotation effects in atomic sodium vapor. *Phys. Rev. A*, 15:2009–2018, May 1977.

[74] Goran Lindblad. On the generators of quantum dynamical semigroups. *Communications in Mathematical Physics*, 48(2):119–130, 1976.

[75] Hanzhe Liu, Yilei Li, Yong Sing You, Shambhu Ghimire, Tony F Heinz, and David A Reis. High-harmonic generation from an atomically thin semiconductor. *Nature Physics*, 13(3):262, 2017.

[76] M Lucchini, SA Sato, A Ludwig, J Herrmann, M Volkov, L Kasmi, Y Shinohara, K Yabana, Lukas Gallmann, and U Keller. Attosecond dynamical franz-keldysh effect in polycrystalline diamond. *Science*, 353(6302):916–919, 2016.

[77] Joaquin M Luttinger and Walter Kohn. Motion of electrons and holes in perturbed periodic fields. *Physical Review*, 97(4):869, 1955.

[78] T. T. Luu, M. Garg, S. Yu. Kruchinin, A. Moulet, M. Th. Hassan, and E. Goulielmakis. Extreme ultraviolet high-harmonic spectroscopy of solids. *Nature*, 521(7553):498–502, May 2015.

[79] Andrea Marini, Conor Hogan, Myrta Grüning, and Daniele Varsano. Yambo: an ab initio tool for excited state calculations. *Computer Physics Communications*, 180(8):1392–1403, 2009.

[80] Nicola Marzari, Arash A Mostofi, Jonathan R Yates, Ivo Souza, and David Vanderbilt. Maximally localized wannier functions: Theory and applications. *Reviews of Modern Physics*, 84(4):1419, 2012.

[81] S. Mathias, L. Miaja-Avila, M. M. Murnane, H. Kapteyn, M. Aeschlimann, and M. Bauer. Angle-resolved photoemission spectroscopy with a femtosecond high harmonic light source using a two-dimensional imaging electron analyzer. *Rev. Sci. Instrum.*, 78(8):083105, 2007.

[82] Klaus Mølmer, Yvan Castin, and Jean Dalibard. Monte carlo wave-function method in quantum optics. *JOSA B*, 10(3):524–538, 1993.

[83] Arash A Mostofi, Jonathan R Yates, Young-Su Lee, Ivo Souza, David Vanderbilt, and Nicola Marzari. wannier90: A tool for obtaining maximally-localised wannier functions. *Computer physics communications*, 178(9):685–699, 2008.

[84] O D Mücke, T Tritschler, M Wegener, U Morgner, and F X Kärtner. Signatures of carrier-wave Rabi flopping in GaAs. *Phys. Rev. Lett.*, 87(5):057401, 2001.

[85] OD Mücke, Th Tritschler, M Wegener, U Morgner, and FX Kärtner. Signatures of carrier-wave rabi flopping in gaas. *Physical review letters*, 87(5):057401, 2001.

[86] Oliver D. Mücke, Thorsten Tritschler, Martin Wegener, Uwe Morgner, Franz X. Kärtner, Galina Khitrova, and Hyatt M. Gibbs. Carrier-wave Rabi flopping: role of the carrier-envelope phase. *Opt. Lett.*, 29(18):2160–2162, Sep 2004.

[87] Nomad. The NOMAD Laboratory A European Centre of Excellence . `https://www.nomad-coe.eu/`. [Online; accessed 1-July-2018].

[88] RW Nunes and Xavier Gonze. Berry-phase treatment of the homogeneous electric field perturbation in insulators. *Physical Review B*, 63(15):155107, 2001.

[89] J Olivier and R Poirier. Electronic structure of al 2 o 3 from electron energy loss spectroscopy. *Surf. Sci.*, 105(1):347–356, 1981.

[90] Giovanni Onida, Lucia Reining, and Angel Rubio. Electronic excitations: density-functional versus many-body green's-function approaches. *Reviews of Modern Physics*, 74(2):601, 2002.

[91] Tim Paasch-Colberg, Agustin Schiffrin, Nicholas Karpowicz, Stanislav Kruchinin, Özge Sağlam, Sabine Keiber, Olga Razskazovskaya, Sascha Mühlbrandt, Ali Alnaser, Matthias Kübel, Vadym Apalkov, Daniel Gerster, Joachim Reichert, Tibor Wittmann, Johannes V. Barth, Mark I. Stockman, Ralph Ernstorfer, Vladislav S. Yakovlev, Reinhard Kienberger, and Ferenc Krausz. Solid-state light-phase detector. *Nature Photon.*, 8(3):214–218, 2014.

[92] Gianluca Panati. Triviality of bloch and bloch–dirac bundles. In *Annales Henri Poincaré*, volume 8, pages 995–1011. Springer, 2007.

[93] E Yu Perlin. Non-linear rotation of light polarization in intrinsic cubic crystals. *Fizika Tverdogo Tela (Sov. Phys. Solid State)*, 22(1):66–69, 1980.

[94] E. Yu. Perlin and A. M. Danishevskii. Optical Faraday effect due to spin-density fluctuations of electrons in n-type semiconductors. *Journal of Experimental and Theoretical Physics*, 79(2):276–285, 1994.

[95] Clas Persson and Claudia Ambrosch-Draxl. A full-band fplapw+ k.p-method for solving the kohn-sham equation. *Computer physics communications*, 177(3):280–287, 2007.

[96] S. V. Popov, Yu. P. Svirko, and N. I. Zheludev. Coherent and incoherent specular inverse faraday effect: $\chi(3)$ measurements in opaque materials. *Opt. Lett.*, 19(1):13–15, Jan 1994.

[97] Muhammad Qasim, Michael S Wismer, Manoram Agarwal, and Vladislav S Yakovlev. Ensemble properties of charge carriers injected by an ultrashort laser pulse. *Physical Review B*, 98(21):214304, 2018.

[98] Raffaele Resta. Why are insulators insulating and metals conducting? *Journal of Physics: Condensed Matter*, 14(20):R625, 2002.

[99] P Romaniello and PL de Boeij. Time-dependent current-density-functional theory for the metallic response of solids. *Physical Review B*, 71(15):155108, 2005.

[100] Erich Runge and Eberhard KU Gross. Density-functional theory for time-dependent systems. *Physical Review Letters*, 52(12):997, 1984.

[101] Edwin E Salpeter and Hans Albrecht Bethe. A relativistic equation for bound-state problems. *Physical Review*, 84(6):1232, 1951.

[102] Shunsuke A Sato and Kazuhiro Yabana. First-principles calculations for initial electronic excitation in dielectrics induced by intense femtosecond laser pulses. In *Laser-Induced Damage in Optical Materials 2016*, volume 10014, page 100141A. International Society for Optics and Photonics, 2016.

[103] Agustin Schiffrin, Tim Paasch-Colberg, Nicholas Karpowicz, Vadym Apalkov, Daniel Gerster, Sascha Muehlbrandt, Michael Korbman, Joachim Reichert, Martin Schultze, Simon Holzner, Johannes V. Barth, Reinhard Kienberger, Ralph Ernstorfer, Vladislav S. Yakovlev, Mark I. Stockman, and Ferenc Krausz. Optical-field-induced current in dielectrics. *Nature*, 493(7430):70–74, JAN 3 2013.

[104] Fabian Schlaepfer, Matteo Lucchini, Shunsuke A Sato, Mikhail Volkov, Lamia Kasmi, Nadja Hartmann, Angel Rubio, Lukas Gallmann, and Ursula Keller. Attosecond optical-field-enhanced carrier injection into the gaas conduction band. *Nature Physics*, page 1, 2018.

[105] O. Schubert, M. Hohenleutner, F. Langer, B. Urbanek, C. Lange, U. Huttner, D. Golde, T. Meier, M. Kira, S. W. Koch, and R. Huber. Sub-cycle control of terahertz high-harmonic generation by dynamical Bloch oscillations. *Nature Photon.*, 8(2):119—123, 2014.

[106] Olaf Schubert, Matthias Hohenleutner, Fabian Langer, Benedikt Urbanek, C Lange, U Huttner, D Golde, T Meier, M Kira, Stephan W Koch, et al. Sub-cycle control of terahertz high-harmonic generation by dynamical bloch oscillations. *Nature Photonics*, 8(2):119–123, 2014.

[107] M. Schultze, E. M. Bothschafter, A. Sommer, S. Holzner, W. Schweinberger, M. Fiess, M. Hofstetter, R. Kienberger, V. Apalkov, V. S. Yakovlev, M. I. Stockman, and F. Krausz. Controlling dielectrics with the electric field of light. *Nature*, 493(7430):75–8, 2013.

[108] M. Schultze, K. Ramasesha, C. D. Pemmaraju, S. A. Sato, D. Whitmore, A. Gandman, J. S. Prell, L. J. Borja, D. Prendergast, K. Yabana, D. M. Neumark, and S. R. Leone. Attosecond band-gap dynamics in silicon. *Science*, 346(6215):1348–1352, December 2014.

[109] Martin Schultze, Elisabeth M. Bothschafter, Annkatrin Sommer, Simon Holzner, Wolfgang Schweinberger, Markus Fiess, Michael Hofstetter, Reinhard Kienberger, Vadym Apalkov, Vladislav S. Yakovlev, Mark I. Stockman, and Ferenc Krausz. Controlling dielectrics with the electric field of light. *Nature*, 493(7430):75–78, JAN 3 2013.

[110] Karlheinz Schwarz, Peter Blaha, and GKH Madsen. Electronic structure calculations of solids using the wien2k package for material sciences. *Comput. Phys. Commun.*, 147(1):71–76, 2002.

[111] Shawn Sederberg, Dmitry Zimin, Sabine Keiber, Florian Siegrist, Michael S. Wismer, Vladislav S. Yakovlev, Isabella Floss, Christoph Lemell, Joachim Burgdorfer, Martin Schultze, Ferenc Krausz, and Nicholas Karpowicz. Attosecond metrology in solids. *submitted*.

[112] David J Singh. Electronic structure calculations with the tran-blaha modified becke-johnson density functional. *Physical Review B*, 82(20):205102, 2010.

[113] Erik Sjöqvist. Geometric phases in quantum information. *International Journal of Quantum Chemistry*, 115(19):1311–1326, 2015.

[114] Erik Sjöqvist, Arun K Pati, Artur Ekert, Jeeva S Anandan, Marie Ericsson, Daniel KL Oi, and Vlatko Vedral. Geometric phases for mixed states in interferometry. *Physical Review Letters*, 85(14):2845, 2000.

[115] A. Sommer, E. M. Bothschafter, S. A. Sato, C. Jakubeit, T. Latka, O. Razskazovskaya, H. Fattahi, M. Jobst, W. Schweinberger, V. Shirvanyan, V. S. Yakovlev, R. Kienberger, K. Yabana, N. Karpowicz, M. Schultze, and F. Krausz. Attosecond nonlinear polarization and light–matter energy transfer in solids. *Nature*, 534(7605):86–90, may 2016.

[116] Ivo Souza, Jorge Íniguez, and David Vanderbilt. Dynamics of berry-phase polarization in time-dependent electric fields. *Physical Review B*, 69(8):085106, 2004.

[117] Marko Spasenović, Markus Betz, Louis Costa, and Henry M. van Driel. All-optical coherent control of electrical currents in centrosymmetric semiconductors. *Phys. Rev. B*, 77:085201, Feb 2008.

[118] Gilbert Strang, Gilbert Strang, Gilbert Strang, and Gilbert Strang. *Introduction to linear algebra*, volume 3. Wellesley-Cambridge Press Wellesley, MA, 1993.

[119] Bala Sundaram and Peter W Milonni. High-order harmonic generation: simplified model and relevance of single-atom theories to experiment. *Physical Review A*, 41(11):6571, 1990.

[120] Y.P. Svirko and N.I. Zheludev. *Polarization of Light in Nonlinear Optics*. Wiley, 1998.

[121] Nicolas Tancogne-Dejean, Oliver D Mücke, Franz X Kärtner, and Angel Rubio. Impact of the electronic band structure in high-harmonic generation spectra of solids. *Physical review letters*, 118(8):087403, 2017.

[122] T. Thirunamachandran. Laser-induced circular dichroism. *Chem. Phys. Lett.*, 49(3):536 – 538, 1977.

[123] Fabien Tran and Peter Blaha. Accurate band gaps of semiconductors and insulators with a semilocal exchange-correlation potential. *Phys. Rev. Lett.*, 102:226401, Jun 2009.

[124] Fabien Tran, Peter Blaha, and Karlheinz Schwarz. Band gap calculations with becke–johnson exchange potential. *Journal of Physics: Condensed Matter*, 19(19):196208, 2007.

[125] Armin Uhlmann. A gauge field governing parallel transport along mixed states. *Letters in Mathematical Physics*, 21(3):229–236, 1991.

[126] G. Vampa, T. J. Hammond, N. Thiré, B. E. Schmidt, F. Légaré, C. R. McDonald, T. Brabec, and P. B. Corkum. Linking high harmonics from gases and solids. *Nature*, 522(7557):462–464, June 2015.

[127] G. Vampa, T. J. Hammond, N. Thiré, B. E. Schmidt, F. Légaré, C. R. McDonald, T. Brabec, D. D. Klug, and P. B. Corkum. All-optical reconstruction of crystal band structure. *Phys. Rev. Lett.*, 115:193603, Nov 2015.

[128] G Vampa, CR McDonald, G Orlando, DD Klug, PB Corkum, and T Brabec. Theoretical analysis of high-harmonic generation in solids. *Physical review letters*, 113(7):073901, 2014.

[129] G B Ventura, D J Passos, J M B dos Santos, J M Viana Parente Lopes, and N M R Peres. Gauge covariances and nonlinear optical responses. *Phys. Rev. B*, 96(3):35431, jul 2017.

[130] G Vignale and Walter Kohn. Current-density functional theory of linear response to time-dependent electromagnetic fields. In *Electronic Density Functional Theory*, pages 199–216. Springer, 1998.

[131] Giovanni Vignale. Mapping from current densities to vector potentials in time-dependent current density functional theory. *Physical Review B*, 70(20):201102, 2004.

[132] Kuljit S Virk and JE Sipe. Semiconductor optics in length gauge: A general numerical approach. *Physical Review B*, 76(3):035213, 2007.

[133] Q. T. Vu, H. Haug, O. D. Mücke, T. Tritschler, M. Wegener, G. Khitrova, and H. M. Gibbs. Light-induced gaps in semiconductor band-to-band transitions. *Phys. Rev. Lett.*, 92:217403, May 2004.

[134] Sanwu Wang. Generalization of the thomas-reiche-kuhn and the bethe sum rules. *Physical Review A*, 60(1):262, 1999.

[135] Xinjie Wang, Jonathan R Yates, Ivo Souza, and David Vanderbilt. Ab initio calculation of the anomalous hall conductivity by wannier interpolation. *Physical Review B*, 74(19):195118, 2006.

[136] Xun-Li Wang, Camden R. Hubbard, Kathleen B. Alexander, Paul F. Becher, Jaime A. Fernandez-Baca, and Steve Spooner. Neutron diffraction measurements of the residual stresses in al2o3-zro2 (ceo2) ceramic composites. *Journal of the American Ceramic Society*, 77(6):1569–1575, 1994.

[137] Marvin J Weber. Handbook of optical materials. *CRC press*, 2002.

[138] Michael S. Wismer and et al. Detection of berry curvature in two-dimensional solid media. *In preparation.*

[139] Michael S. Wismer, Stanislav Yu. Kruchinin, Marcelo Ciappina, Mark I. Stockman, Ferenc Krausz, and Vladislav S. Yakovlev. Ultrafast coherent control of charge carriers in semiconductors. *CLEO/Europe-EQEC 2015*, Jun 2015.

[140] Michael S. Wismer, Stanislav Yu. Kruchinin, Marcelo Ciappina, Mark I. Stockman, and Vladislav S. Yakovlev. Strong-field resonant dynamics in semiconductors. *Phys. Rev. Lett.*, 116:197401, May 2016.

[141] Michael S Wismer, Stanislav Yu Kruchinin, Marcelo Ciappina, Mark I Stockman, and Vladislav S Yakovlev. Strong-field resonant dynamics in semiconductors. *Physical review letters*, 116(19):197401, 2016.

[142] Michael S. Wismer, Stanislav Yu. Kruchinin, Marcelo F. Ciappina, Mark I. Stockman, and Vladislav S. Yakovlev. Strong-field resonant light-induced currents in semiconductors. *8th EPS-QEOD Europhoton Conference*, Aug 2016.

[143] Michael S. Wismer, Mark I. Stockman, and Vladislav S. Yakovlev. Ultrafast optical faraday effect in crystalline al2o3. *6th International Conference on Attosecond Physics*, Jul 2017.

[144] Michael S. Wismer, Mark I. Stockman, and Vladislav S. Yakovlev. Ultrafast optical faraday effect in transparent solids. *Phys. Rev. B*, 96:224301, Dec 2017.

[145] Michael S. Wismer and Vladislav S Yakovlev. Gauge-independent decoherence models for solids in external fields. *Physical Review B*, 97(14):144302, 2018.

[146] D.M. Wolkow. Über eine klasse von lösungen der diracschen gleichung. *Zeitschrift für Physik*, 94(3-4):250–260, 1935.

[147] Mengxi Wu, Dana A Browne, Kenneth J Schafer, and Mette B Gaarde. Multilevel perspective on high-order harmonic generation in solids. *Physical Review A*, 94(6):063403, 2016.

[148] Mengxi Wu, Shambhu Ghimire, David A. Reis, Kenneth J. Schafer, and Mette B. Gaarde. High-harmonic generation from Bloch electrons in solids. *Phys. Rev. A*, 91:043839, Apr 2015.

[149] Vladislav S. Yakovlev and Michael S. Wismer. Adiabatic corrections for velocity-gauge simulations of electron dynamics in periodic potentials. *Computer Physics Communications*, 217:82–88, Aug 2017.

[150] Vladislav S Yakovlev and Michael S Wismer. Adiabatic corrections for velocity-gauge simulations of electron dynamics in periodic potentials. *arXiv preprint arXiv:1702.07410*, 2017.

[151] C. Zener. A theory of the electrical breakdown of solid dielectrics. *Proc. Royal Soc. London. Ser. A*, 145:523–529, 1934.